A μ-biomimetic uncooled infrared sensor based on the infrared receptors of *Melanophila acuminata*

Dissertation
zur
Erlangung des Doktorgrades (Dr. rer. nat.)
der
Mathematisch-Naturwissenschaftlichen Fakultät
der
Rheinischen Friedrich-Wilhelms-Universität Bonn

vorgelegt von
Georg Siebke
aus
Überlingen

Bonn, 01.2015

Dieser Forschungsbericht wurde als Dissertation von der Mathematisch-Naturwissenschaftlichen Fakultät der Universität Bonn angenommen und ist auf dem Hochschulschriftenserver der ULB Bonn http://hss.ulb.uni-bonn.de/diss_online elektronisch publiziert.

1. Gutachter: Prof. Dr. H. Schmieden
2. Gutachter: Prof. Dr. U. B. Kaupp

Tag der Promotion: 03.11.2015
Erscheinungsjahr: 2015

Meiner Frau und
unserem ungeborenen Sohn

Summary

The pyrophilous beetle *Melanophila acuminata* depends on freshly burnt wood for reproduction. It is able to reach forest fires from large distances of up to 130 km. The beetle possesses an organ sensitive to IR radiation that employs a *photomechanic* detection principle. A liquid filled pressure chamber with a diameter of about 15 µm is heated by absorption of the radiation. The liquid expands and leads to the deflection of a mechanosensitive dendrite. In addition, the IR receptors of the beetle *Melanophila acuminata* possess a sophisticated compensation mechanism for large temperature differences.

In this work, a biomimetic IR sensor based on the IR receptors of *Melanophila acuminata* is developed by means of micro systems technology. The sensor consists of two liquid-filled chambers that are connected by a micro-fluidic system. Absorption of IR radiation by one of the chambers leads to heating and expansion of a liquid. The increasing pressure deflects a membrane. The membrane is part of a plate capacitor with a diameter of 500 µm and an electrode distance of 500 nm. The micro-fluidic system and the other chamber represent a fluidic low-pass filter, preventing slow, but large pressure changes. The strong frequency dependence of the filter demands a precise characterization of its properties. Furthermore, it requires a modulation of the incident IR radiation.

To predict optimal dimensions and material properties for the sensor design, a theoretical model is developed. The model is able to predict the modulation frequency dependent response based on a variety of parameters. It describes the transport of liquid between the two chambers, the deflections of the two membranes, the heat transfer inside the sensor, and, finally, the heat exchange of the sensor with its environment and a distant heat source. The model especially allows to calculate the filter properties of the compensation mechanism. An experimental test of the fluidic filter mechanism is able to verify the model predictions.

To analyse the influence of several parameters on the sensitivity of the sensor, a simplified sensor is presented. This sensor is larger than the full-featured sensor and does not feature the compensation mechanism; yet it employs the same detection mechanism. Sensors with different membrane diameters and thicknesses are produced and characterized at different temperatures. The measurements are used to verify the behaviour of the membrane deflection. Furthermore, an electronics setup and a graphical user interface for the computer-assisted readout is developed. This setup is successfully tested using the simplified sensor but is also most suitable for the full-featured sensor.

Finally, a solution for the fabrication of the capacitor is presented. Due to the large aspect ratio between electrode diameter and distance of 1000, a standard sacrificial layer process cannot be employed. Instead, different other processes are evaluated and further developed. The obtained capacitors show the predicted behaviour and pave the way for the fabrication of the complete sensor including the compensation mechanism.

Contents

1 Introduction **1**

2 Basics **3**

2.1 The beetle *Melanophila acuminata* 3
2.1.1 Detection mechanism 3
2.1.2 Sensitivity 5
2.1.3 Other biological IR sensors 6
2.2 Infrared sensor technology 6
2.2.1 Radiometry 6
2.2.2 Figures of merit 7
2.2.3 Thermal detectors 8
2.2.4 Photon detectors 10
2.2.5 Comparison of photon and thermal detectors 10
2.3 Micro systems technology (MEMS) 10
2.3.1 Substrates 11
2.3.2 Deposition 12
2.3.3 Photolithography 13
2.3.4 Etching 15
2.3.5 Wafer bonding 17

3 Transfer from biology to a sensor concept **19**

3.1 Model description 20
3.1.1 Fluidic model 21
3.1.2 Thermal model 24
3.1.3 Environment 26
3.1.4 Expansion 28
3.2 Model predictions 28
3.2.1 Sensor response 28
3.2.2 Fluidic low-pass filter 31
3.3 Simulation of the membranes and the heat transfer 32
3.3.1 Simulation of the membrane deflection 32
3.3.2 Simulation of the heat transfer 33
3.4 The fluidic low-pass filter 35
3.4.1 Chip design 35
3.4.2 Experimental setup 37
3.4.3 Pretest 38
3.4.4 Calculation of the spring constants 39
3.5 Estimation of the beetle's sensitivity 42

4 From the sensor concept to a technological sensor **45**
4.1 Design of the micro technological sensor 45
4.2 Parameter optimization 46
4.2.1 Requirements regarding the sensor 47
4.2.2 Implications of the model 48
4.3 Process flow 49
4.4 Bubble-free filling and assembly 57
4.4.1 Bubble-free Filling 57
4.4.2 Manufacturing of the PDMS layer 59
4.4.3 Assembly of the sensor 59

5 Readout of the μ-biomimetic sensor **61**
5.1 Measurement electronics 61
5.2 Data acquisition (DAQ) 63
5.3 Test setup 66

6 Proof of the detection principle on a larger scale **69**
6.1 Design of a simplified sensor 69
6.2 Parasitic capacitances 73
6.2.1 Substrate grounding 75
6.2.2 Thickening the insulating layers 75
6.2.3 Reducing the electrode diameter 76
6.3 Analysis of experimental data 76
6.4 Results 78
6.4.1 Room temperature 78
6.4.2 Verification of the expected deflection 80

7 On the way to the μ-biomimetic sensor **85**
7.1 Manufacturing of the μ-capacitors 85
7.1.1 Sacrificial a-Si layer process 87
7.1.2 Support point process 89
7.1.3 Optimized support point process 91
7.2 The first sensors based on the μ-capacitor 91

8 Conclusion and outlook **95**

A Flowcharts **99**

B Masks **115**

C Electronics **117**

List of Figures **123**

List of Tables **125**

List of Symbols **129**

List of Abbreviations **131**

Bibliography **131**

1 Introduction

Each year, forest fires cause the devastation of large territories. Such fires destroy the habitats of animals, threaten villages and cities, and entail huge cost. However, not every species suffers from forest fires. On the contrary, different *pyrophilous* beetles of the genus *Melanophila* even require the occurrence of forest fires. These beetles reproduce on freshly burnt trees because their larvae need the charred wood to develop. As the beetles depend on such fires, they must be able to reach distant forest fires starting from their habitat. Historical reports show that beetle of the genus *Melanophila* are able to find forest fires within distances of up to 130 km.

To achieve such a huge range, the beetles might be able to detect the infrared (IR) radiation that is emitted by a forest fire. The beetles possess an organ sensitive to IR radiation that employs a *photomechanic* detection principle. A liquid filled pressure chamber with a diameter of about 15 µm is heated by absorption of the radiation. The liquid expands and leads to the deflection of a mechanosensitive dendrite. In addition, the IR receptors of the beetle *Melanophila acuminata* possess a sophisticated compensation mechanism for large temperature differences. As the temperature differences between day and night can be much larger than those imposed by a distant forest fire, they might deteriorate the actual measurement. To prevent this, the wall of the pressure chamber contains small channels with a diameter of a few nanometres. These allow for a slow transfer of liquid between the chambers. Hence, slow pressure changes are compensated. To be still able to detect constant heat sources, the beetle modulates the radiation with its wing flaps. In this way, the constant signal is converted into a fast changing signal that is not affected by the compensation mechanism. A technical sensor based on the IR receptors with such a range, as presented in this work, will outperform current commercially available uncooled sensors. Analogously to the beetle, the sensor can e.g. be employed for the detection of forest fires. Used in an early warning system, it will help to prevent the expansion of forest fires.

While the beetle *Melanophila acuminata* undoubtedly possesses an organ that is able to detect IR radiation, the actual sensitivity has been discussed controversially for decades. Although there are strong hints that the beetle can use its IR receptors to detect distant forest fires, other findings only imply a short range of about 100 m. On the one hand, to detect fires in a distance of more than 100 km, an exceptional sensitivity unmatched by current uncooled IR sensors is required. On the other hand, the detection of fire from a distance of 100 m is not sufficient to find a forest fire. Instead, it allows the beetle to navigate inside the burning forest to prevent landing on hot surfaces. Nevertheless, the compensation mechanism is even more important in this application as the receptor is exposed to much larger temperatures changes. The same is true for technical sensors. Sensors that need to cover a large range usually provide a worse resolution compared to sensors that are optimized for a small range. This dilemma is solved by the compensation mechanism. It automatically shifts the detection range to the current conditions. Therefore, sensors with an otherwise small range but high sensitivity can be used in a large range. This means that such a com-

pensation mechanism as presented in this work can also be used for other types of sensors that use a fluid, e.g. pressure sensors. So, whether the beetle detects forest fires from distances of 100 m or 100 km, it provides a promising model for a biomimetic IR sensor. In fact, the discussion about the sensitivity further demands a technical sensor, which helps to answer the open questions.

The aim of this work is to build a foundation for the production of a biomimetic IR sensor based on the IR receptors of *Melanophila acuminata*. To be as close as possible to the biological model and to achieve the highest sensitivity using a small size, it has to be fabricated by means of micro systems technology. As for the IR receptors of *Melanophila acuminata*, the central component is a liquid filled chamber. Instead of the dendrite, a membrane is deformed by the increasing volume. The membrane is part of a plate capacitor with a diameter of 500 µm and an electrode distance of 500 nm. The fabrication of such a capacitor is the largest challenge in the development for the sensor. When transferring this aspect ratio into an everyday scene, the cables of a power pylon with a distance of 1 km should not sag more than 1 m, not even accounting for additional deflections. At the same time, the small electrode distance imposes a potential drawback of the sensor. Large temperature changes that occur if the ambient temperature increases could deflect the membrane until it touches the other electrode. Yet the biological model provides the solution to this problem. By implementing a fluidic compensation mechanism, the membrane is relieved from large pressures while a modulated signal is detected without loss of sensitivity. In this way, the sensor adapts itself to varying temperatures. The compensation mechanism is implemented by means of a second chamber that is connected to the pressure chamber by a long and narrow channel. To be able to take up excess liquid, the compensation chamber is also closed by a membrane.

This work is structured as follows. In Chapter 2, the biological model and its sensitivity are described in detail. Furthermore, a general description of IR sensors including the classification and figures of merit is presented. Finally, an overview of micro systems technology and the processes used in this work is given. After the analysis of the biological model, a general sensor concept is derived in Chapter 3. The sensor concept is accompanied by a mathematical model that describes the frequency dependent sensor response based on the geometry and the materials. To prove the functioning of the compensation mechanism and the prediction of the model, a dedicated experimental test is performed. With the mathematical model at hand, the optimal geometry of the sensor fabricated by means of micro systems technology is deduced in Chapter 4. Following the description of the sensor design, the micro-technological process flow is presented as well as additional steps required e.g. for the bubble-free filling of the sensor. The electronics and software which measure the capacitance of the sensor and analyse the raw data are presented in Chapter 5, and an appropriate test setup to characterize different sensors is developed. The test setup is put to use in Chapter 6 to analyse a simplified version of the biomimetic sensor. This sensor focuses on the proof-of-principle of the photomechanic detection leaving out the compensation mechanism. After the thorough tests of the simplified sensor, first prototypes of the capacitor with the aspect ratio of 1000 are obtained in Chapter 7. The first working capacitors are used to build sensors similar to the large simplified sensor. These air-filled sensors prove the feasibility of the capacitors and, together with the other components presented throughout this work, of the complete sensor (Chapter 8). The completion, characterization, and optimization of the full-featured sensor is left to future works. In this work, all the components required for the sensor are provided.

2 Basics

2.1 The beetle *Melanophila acuminata*

The pyrophilous jewel beetle *Melanophila acuminata* possesses infrared (IR)-sensing organs used to detect fires (Figure 1(a)). It uses the organ to find suitable places for reproduction as the larvae can only develop in freshly burnt wood found in areas with recent forest fires [1, 2]. However, it is still unclear if the beetle uses the organ to find forest fires or if it is used to navigate in freshly burnt forests. The IR-sensing organ is located next to the mesothoracic legs (Figure 1(a)) and consists of about 70 to 100 IR-sensing receptors (*sensilla*) [1] evolved from hair mechanoreceptors (Figure 1(b)) [3–5]. The exact detection mechanism is not fully understood yet. More than that, the sensitivity is discussed controversially [6–10].

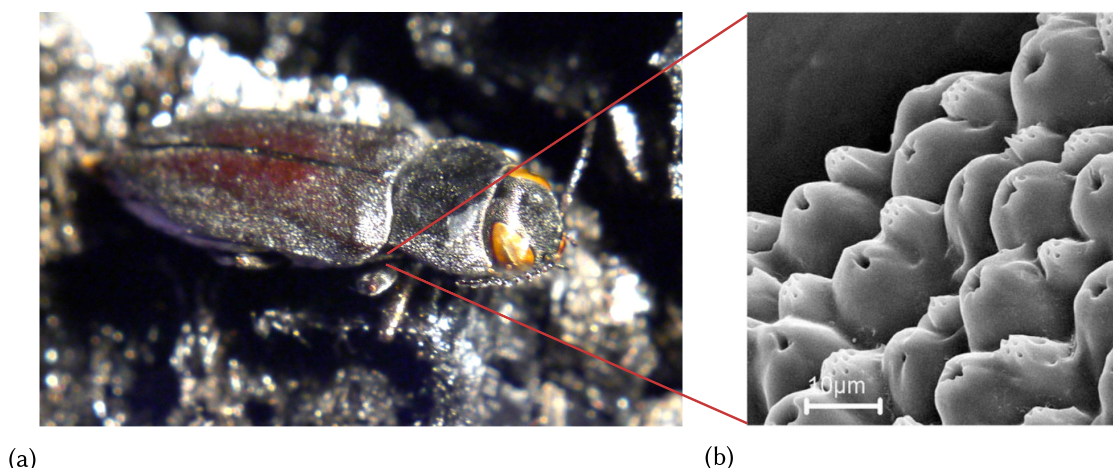

(a) (b)

Figure 1: The biological IR-sensor. (a) The pyrophilous jewel beetle *Melanophila acuminata* (from Siebke et al. [11]). (b) Scanning electron microscope image of the IR-sensing sensillae of *Melanophila acuminata* (from Klocke et al. [12], available under the terms of the Creative Commons Attribution Licence, Version 2.0).

2.1.1 Detection mechanism

Most probably, the receptors are based on the following mechanism [5, 13]: The central component of the sensillum is a liquid filled pressure chamber made of a hard chitin structure (Figure 2). The inside of the sphere contains a sponge-like structure with many interconnected lacunae [4]. Upon absorption of radiation, the liquid inside the sphere is heated and expands. The chitin structure is stiff and withstands the increasing pressure. Instead, the increasing volume leads to the deformation of the tip of the dendrite that is located at the bottom of the pressure chamber. Following the deformation of the dendritic

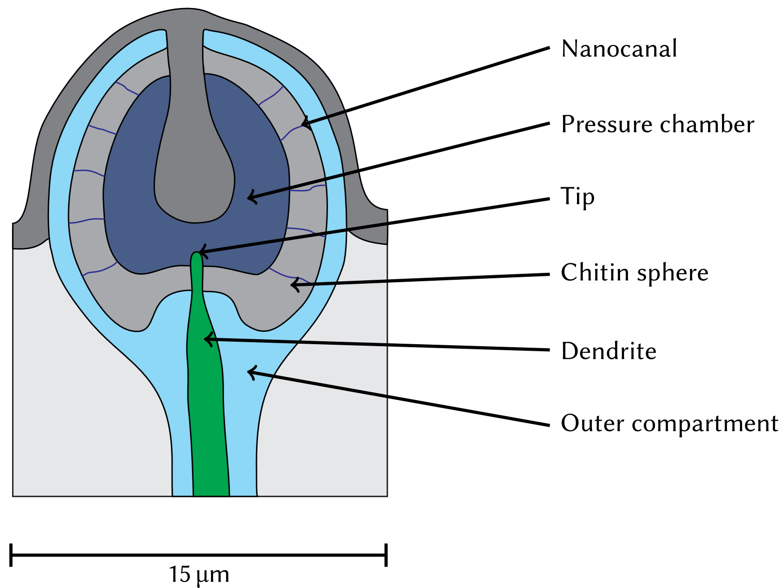

Figure 2: Simplified cross section of one IR sensillum of the beetle (from Siebke et al. [11]).

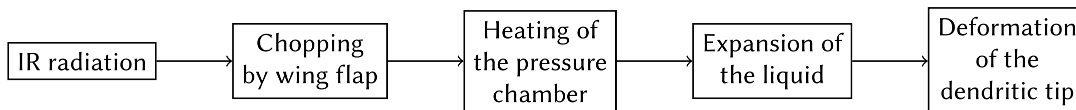

Figure 3: Detection chain of the IR sensillae of *Melanophila*.

tip, its mechanoreceptive neuron generates a response; the dendrite represents the biological transducer. Due to the indirect measurement of IR radiation, the detection mechanism is referred to as *photomechanic*.

One highlighting feature of the IR receptors of *Melanophila acuminata* is a compensation mechanism coping with large changes in ambient temperature. During the course of a day, the ambient temperature changes slowly by several kelvins. As the sensilla are in contact to the outside, they are also subject to these large temperature changes. At the same time, the minimal detectable temperature changes due to a distant heat source is below a millikelvin (see Section 3.5). The compensation mechanism prevents the build-up of large pressures, which would interfere with the detection of these very small signals or could even damage the sensillum. The compensation mechanism consists of nanocanals connecting the pressure chamber to the outer compartment, a large liquid volume. These canals allow for a slow transport of liquid. In this way, slow temperature increases are compensated. Sufficiently fast changes are not affected as the liquid transport is too slow. Hence, the compensation mechanism represents a fluidic low-pass filter.

Usually, a heat source, e.g. a forest fire, emits a constant heat flux. Due to the compensation mechanism, the IR receptor is blind to constant signals. To enable the detection of constant signal, the incident radiation is periodically *chopped* by the wing flap of the beetle with a frequency of about 100 Hz [14]. In this way, the constant signal is converted in a modulated signal that is not affected by the compensation mechanism. Chopping of the incident radiation is also used for technical IR sensors to reduce noise; pyroelectric sensors even require chopping as they are only sensitive to irradiance changes (see Sections 2.2.1 and 2.2.2). The complete detection chain in depicted is Figure 3.

2.1.2 Sensitivity

Although the detection mechanism of the IR receptors of *Melanophila acuminata* is in the focus of many studies, the actual sensitivity to IR radiation is still unclear. On the one hand, model calculations suggest that the beetle is able to detect IR radiation as weak as $4 \times 10^{-5}\,\mathrm{W\,m^{-2}}$ or even lower [15]. This is much less than current commercial pyroelectric sensors with a sensitivity threshold of about $2 \times 10^{-3}\,\mathrm{W\,m^{-2}}$ [16]. On the other hand, electrophysiological experiments yield thresholds of up to $150\,\mathrm{W\,m^{-2}}$, differing by six to seven orders of magnitude from the values of the model calculations [8, 17].

Several attempts were made to measure the sensitivity of the IR organ of *Melanophila* beetles during the last decades. There are four important methods investigated in this work, partially yielding drastically different results. First, behavioural experiments were conducted. Upon illumination of the receptors by IR radiation, the beetle responded with a twitching of its antennae. Afterwards, the organs were disabled using paint and the response vanished. Thereby it is ensured that the organ is responsible for the detection of IR radiation. During the experiment, different individuals were tested using radiation of different intensities and wavelengths. The threshold intensity was defined as the intensity evoking a response for at least 50 % of all trials. The lowest sensitivity threshold of $0.6\,\mathrm{W\,m^{-2}}$ was measured for wavelengths of $3.0\,\mu\mathrm{m}$ to $3.5\,\mu\mathrm{m}$ [2].

Second, action potentials of the dendrite located in the sensillum were recorded. A change in spike frequency of the associated neuron was used to define the sensitivity threshold. The resulting detection thresholds range between $50\,\mathrm{W\,m^{-2}}$ and $173\,\mathrm{W\,m^{-2}}$. The maximum sensitivity was measured for two wavelength regions, $3\,\mu\mathrm{m}$ to $5\,\mu\mathrm{m}$ and $8\,\mu\mathrm{m}$ to $12\,\mu\mathrm{m}$ [8, 14, 17–19]. The spectral sensitivity of the receptors is perfectly adapted to the atmosphere, as it is mostly transparent in the specified range. The large difference between the sensitivity obtained in the electrophysiological measurements and the behavioural experiments can be caused by different mechanisms. First, the definitions of the threshold are inherently different. The electrophysiological experiments use a change of the spike frequency while the behavioural experiments rely on the antennae twitching of the beetle. Furthermore, the electrodes used in electrophysiological experiments change the thermal mass of the receptors and diminish the response [14]. Lastly, the beetle may use the large number of receptors (about 100) to increase the sensitivity manifesting in behavioural experiments.

Third, the sensitivity was estimated indirectly based on historic reports about the distance that beetles travel to reach a forest fire. Different literature sources state that *Melanophila* beetles detect forest fires from large distances up to 130 km [1, 2, 15, 20, 21]. Within this assumption, the beetle must be able to detect an irradiance equal to or lower than the irradiance at such a distance from the fire. The highest sensitivity was calculated using the data from an oil tank fire [15]. In 1924, an oil reservoir in Coalinga, California caught fire and burnt for several days. Some days after the onset of the fire, a large number of *Melanophila* beetles was observed at the place of the fire. However, the beetles must originate from a forest with a recent forest fire as a suitable breeding place. The authors of [15] conclude that the next suitable forest is at distance of 130 km from the oil reservoir. Using model calculations of the burning oil tanks to estimate the irradiance at the origin of the beetles, a detection threshold of down to $1.3 \times 10^{-4}\,\mathrm{W\,m^{-2}}$ was obtained.

Fourth, a theoretical biological limit was derived based on the geometry of the sensillum and basic biological detection limits of mechanoreceptors. Within this, a detection threshold $3 \times 10^{-9}\,\mathrm{W\,m^{-2}}$ to $4 \times 10^{-7}\,\mathrm{W\,m^{-2}}$ was predicted [15]. For a diameter of the

sensillum $d = 5\,\mu\text{m}$ and a response time $\Delta t = 4\,\text{ms}$ [15], the number of photons with wavelength $\lambda = 3\,\mu\text{m}$ (see above) that should be sufficient for detection is

$$n_\gamma = \frac{E_\text{e} \cdot (d/2)^2 \pi \cdot \Delta t}{hc/\lambda} = 0.014, \quad (1)$$

where E_e is the irradiance (see next section), h is Planck's constant, and c is the speed of light. As this number is below one, at least this very low biological limit can be precluded.

Instead of calculating the sensitivity from information about the distance from which the beetle can sense forest fires, it was also tried to estimate this distance based on measured sensitivities. Due to the different sensitivities and, in part questionable, calculation methods, the resulting distances range from 50 m to 130 km [2, 8, 14, 22, 23]. The knowledge of this distance however is important for understanding the behaviour of the beetle. On the one hand, a distance of 130 km enables the beetle to find forest fires. On the other hand, a distance of 50 m is not sufficient to accomplish this. It rather enables the beetle to navigate inside a burning forest to avoid landing on glowing hot wood.

2.1.3 Other biological IR sensors

There are more animals which possess highly sensitive IR-sensing organs [24]. For example, the Australian flat bug *Aradus* uses a receptor similar to that of *Melanophila* [25]. Yet it does not feature a pressure compensation mechanism [26]. The Australian "fire-beetle" *Merimna atrata* has an IR-sensing organ with a much lower sensitivity of about $400\,\text{W}\,\text{m}^{-2}$ which is also based on a photomechanic detection principle [19, 27]. This sensor is similar to the Australian "Little Ash Beetle" *Acanthocnemus nigricans* with a sensitivity of about $250\,\text{W}\,\text{m}^{-2}$ [28, 29]. However, the latter employs a fundamentally different detection mechanism. Furthermore, some snakes use IR sensing for hunting [30]. The highest sensitivity found for snakes is $0.2\,\text{W}\,\text{m}^{-2}$, discovered in *Agkistrodon rhodostoma* [31]. The beetle *Melanophila* thus may possess the most sensitive IR organs suitable to detect IR radiation sources from large distances.

2.2 Infrared sensor technology

The detection mechanism of *Melanophila acuminata* is referred to as *photomechanic*. The incident radiation is not detected directly. Rather, it triggers a mechanical deformation that is subsequently detected. In contrast to this, common commercially available IR sensors, such as thermal sensors or quantum detectors, employ different mechanisms. IR detectors can be divided into two classes, depending on their detection principle. *Thermal detectors* take advantage of physical properties that change with temperature. *Photon detectors* rely on the conversion of incident photons into conducting electrons within the material. In the following, the fundamental radiometric terms and the quantities used to characterize IR detectors are explained. Afterwards, the different types of IR detectors are presented.[1]

2.2.1 Radiometry

Radiometry describes the radiation flux through an optical system. Table 1 shows all relevant terms used in this work. *Radiant energy* Q_e and *radiant flux* Φ_e are generic terms

[1] For more details about radiometry and IR sensors, see e.g. [32, 33].

Symbol	Radiometric quantity	Unit
Q_e	Radiant energy	J
Φ_e	Radiant flux	W
I_e	Radiant intensity	$W\,sr^{-1}$
M_e	Radiant exitance	$W\,m^{-2}$
L_e	Radiance	$W\,m^{-2}\,sr^{-1}$
E_e	Irradiance	$W\,m^{-2}$

Table 1: Radiometric terms used to describe IR radiation.

describing an amount of transported energy or power.[2] The *radiant intensity* I_e is the radiant flux per solid angle Ω radiated from a point source:

$$I_e = \frac{\partial \Phi_e}{\partial \Omega}. \tag{2}$$

The *exitance* M is the flux per area A_e leaving the emitter surface, e.g. a heat source:

$$M_e = \frac{\partial \Phi}{\partial A_e}. \tag{3}$$

The *radiance* L describes the flux per area A_e and per solid angle Ω_r:

$$L_e = \frac{\partial^2 \Phi_e}{\partial A_e \cos\theta_e \partial \Omega_r} \tag{4}$$

$$\Rightarrow \partial^2 \Phi = L \partial A_e \cos\theta_e \partial \Omega_r, \tag{5}$$

where θ is the angle between the emitter surface and the solid angle element $\partial\Omega_r$. Equation (5) is also called the fundamental equation of radiation transfer. The *irradiance* is the incident flux per area on the receiver surface, e.g. a sensor:

$$E_e = \frac{\partial \Phi_e}{\partial A_r}. \tag{6}$$

2.2.2 Figures of merit

An IR sensor absorbs radiation and converts it into a quantity that can be measured by an electronic circuit. Most often this quantity is a voltage U or a current I. As described in Chapter 3, the output signal of the µ-biomimetic sensor is a capacitance C. In the following, C will be used to represent either of these possibilities. The change of the output signal C with respect to the incident flux Φ_e is the *responsivity*

$$\mathcal{R}_C = \frac{\Delta C}{\Delta \Phi_e}. \tag{7}$$

If the measurable quantity is a voltage or a current, the symbols $\mathcal{R}_U$ or $\mathcal{R}_I$ are used instead. Often the incident radiation is modulated, e.g. using a rotating chopper wheel. Then,

[2] The subscript "e" implies that these quantities are related to the radiation field and based on energy instead of photon count.

only the respective Fourier component of the output signal is measured. This technique provides discrimination against some electrical noise and, most important, a drift of the sensor signal. IR sensors are sensitive to changes in ambient temperature, which distort the sensor response. By modulating the signal that should be measured, such distortions are eliminated. The responsivity to radiation modulated at frequency f is defined as

$$\mathscr{R}_C(f) = \frac{C_0(f)}{\Phi_0(f)}, \tag{8}$$

where C_0 and Φ_0 are the amplitude of the capacitance and the incident flux, respectively. Furthermore, the responsivity depends on the wavelength λ of the incident radiation. The *spectral responsivity* is the response to monochromatic radiation of wavelength λ at modulation frequency f. The dependence on the wavelength is fundamentally different for thermal and photon detectors (see below).

2.2.3 Thermal detectors

Thermal detectors do not measure the incident flux directly. They rather measure the change in temperature due to the incident flux. As the change in temperature only depends on the absorbed radiant energy, it is independent of the wavelength (Figure 4(a)). Instead, the detection band is limited by the spectral properties of the absorber or the protective window. Thermal IR sensors are easy to use as they do not require any cooling. However, the response is rather slow due to the time the sensor needs to heat up. Many different mechanism are used to measure the temperature changes of the sensor.

Thermocouples and thermopiles

Thermocouples or *thermoelectric detectors* consist of two junctions of two different conductors. Due to the Seebeck-effect, a temperature dependent voltage is produced at the junctions. The *hot* junction is exposed to IR radiation whereas the *cold* junction is shielded. At the hot junction, the two conductors are electrically connected, whereas the cold junction is left open. Due to the different temperatures at the two junctions, the voltage differs. Therefore, the two voltages at the junctions do no cancel but a temperature dependent voltage difference can be measured at the cold junction. The voltage difference is described by the Seebeck coefficient

$$\Theta = \frac{\mathrm{d}U}{\mathrm{d}T}, \quad \mathit{Signal} \propto \Delta T. \tag{9}$$

The signal of a thermocouple is proportional to the temperature difference. By connecting many thermocouples in series, a *thermopile* is obtained, which features a higher sensitivity than a single thermocouple. Compared to other thermal detectors, thermocouples and thermopiles are rather slow and insensitive. However, they are very reliable and comparably cheap.

Pyroelectric detectors

Pyroelectric detectors are made of pyroelectric crystals. These crystals exhibit a permanent electrical polarization that is dependent on the temperature. Two electrodes are connected to opposing sides perpendicular to the polarization axis. At constant temperature, the polarization is neutralized by mobile charges on the surfaces. Therefore, no

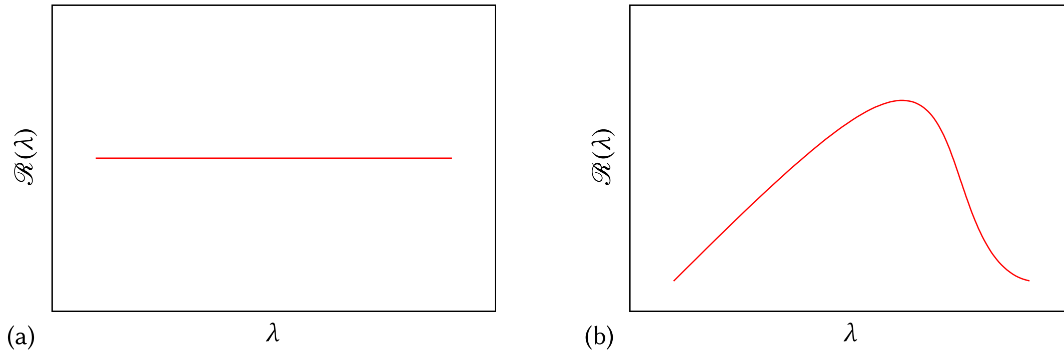

Figure 4: Shape of the spectral responsivity of thermal (a) and photon (b) detectors. (a) The responsivity of thermal detectors is independent of the wavelength. (b) The responsivity of photon detectors increases linearly with the wavelength until it drops off at a cut-off wavelength.

voltage can be measured. When the temperature changes due to a variation of the irradiance, a voltage between the surfaces arises. To be able to measure a constant irradiance, the incident radiation has to be chopped (see Section 2.2.2). The change in polarization is described by the pyroelectric coefficient

$$p = \frac{\mathrm{d}P}{\mathrm{d}T}, \quad \mathit{Signal} \propto \frac{\mathrm{d}T}{\mathrm{d}t}, \tag{10}$$

where P is the electrical polarization. The signal is proportional to the rate of change of the temperature. A common material used e.g. to build motion detectors is lead zirconate titanate (PZT). Materials like barium strontium titanate (BST) are most commonly used to fabricate imaging detectors but require a more general definition of the pyroelectric coefficient. Pyroelectric sensors are more sensitive than thermoelectric sensors. They however require chopping and they are sensitive to vibrations [32].

Bolometers

Bolometers are based on materials that change their electrical resistance R upon a temperature change. The change in resistance is described by the TCR (temperature coefficient of resistance)

$$\alpha = \frac{1}{R}\frac{\mathrm{d}R}{\mathrm{d}T}, \quad \mathit{Signal} \propto T. \tag{11}$$

The resulting signal is proportional to the temperature. As bolometers can measure constant temperatures, they do not require chopping as do pyroelectric sensors. Usually, bolometers are made of a thin membrane consisting of a suitable material like vanadium oxide (VO_x) or amorphous silicon (a-Si). The membrane is thermally insulated from the substrate to achieve a maximum change in temperature and thus in resistance and signal. Arrays of *micobolometers* can be fabricated by means of micro systems technology.

Other thermal detectors

Apart from the three types of thermal detectors presented above, there exist several more. These are either still at an early development stage or are only seldom used. Many novel developments make use of micro systems technology to build miniaturized sensors

with mechanical components. These include microcantilevers, bimaterial detectors, and torsional resonators [34–36]. The *Golay cell* consists of a gas filled chamber with a flexible membrane. Upon absorption of radiation, the gas is heated and the membrane is distorted. On the membrane, a mirror is located, which is deflected and changes the irradiance and thus the photocurrent of a photocell or a photodiode [37–39]. Miniaturized Golay cells are developed using micro systems technology with capacitive readout [40], tunneling displacement transducers [41], or interferometric readout [42]. Furthermore, recent studies propose the use of nanostructures inspired by the *Morpho* butterfly for the use in IR detectors [43].

2.2.4 Photon detectors

All *photon detectors* are based on the internal photoelectric effect. Upon absorption of photons in a semiconductor, electron-hole pairs are created. In *photovoltaic* detectors, the electron-hole pairs are separated at a p-n junction of a diode and produce a photocurrent. In contrast to this, the electron-hole pairs lead to an increase of conductance in *photoconductive* detectors. Most photon detectors are based on either of these two effects. Besides, other effects, e.g. the photoelectromagnetic (PEM) effect, are exploited for IR sensors. In addition to the different physical effects, many different materials are used for photon detectors. These include silicon and germanium detectors, photoemissive detectors (metal-semiconductor junctions), III-V and IV-VI semiconductor detectors, mercury cadmium telluride (HgCdTe) detectors, and more complex structures like quantum well IR photodetectors (QWIP), quantum dot photodetectors (QDIP), and superlattice detectors. One of the most important materials used for IR detectors is mercury cadmium telluride (HgCdTe), which can be used both for photovoltaic and photoconductive detectors.

Each photon absorbed in a photon detector contributes equally to the sensor signal. Therefore, the responsivity increases with increasing wavelength, as more photons per energy are absorbed. However, a minimum energy is required for any absorption at all. In *intrinsic* photon detectors, the photon energy must be at least as large as the band-gap energy. In *extrinsic* photon detectors, the absorption of photons involves impurity levels in the band-gap and thus requires less energy. Due to the minimum energy, the responsivity decreases abruptly above cut-off wavelength (Figure 4(b)).

2.2.5 Comparison of photon and thermal detectors

The most obvious difference between photon and thermal IR detectors is the difference in the spectrum (Figure 4). The responsivity and detectivity of thermal detectors are independent of the wavelength, whereas photon detectors are most sensitive in a specific wavelength region. To limit the response of thermal detectors to certain wavelengths, an appropriate absorber or window material has to be used. In general, photon detectors offer the largest theoretical detectivity. However, to achieve a larger detectivity than thermal detectors, they need cryogenic cooling down to 30 K to 50 K [44]. At the same time, the detectivity of thermal detectors is usually independent of the temperature.

2.3 Micro systems technology (MEMS)

Micro systems are devices that may incorporate electrical, optical, fluidic, and mechanical components. Therefore, such devices are often called MEMS or MOEMS devices (Micro-(Opto-)Electrical-Mechanical Systems). The dimensions of such devices range from submicrometres to millimetres. Micro systems are built by means of micro systems technology,

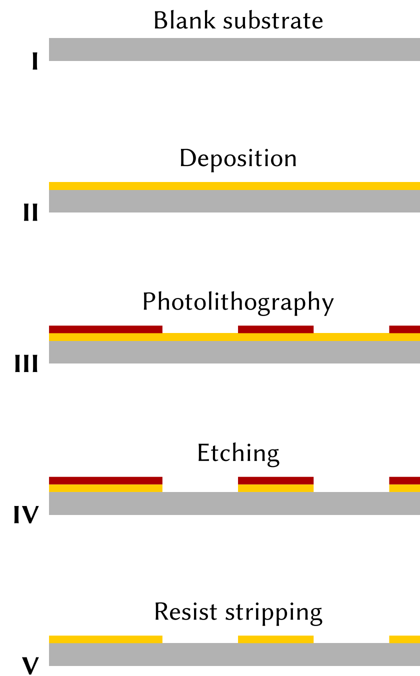

Figure 5: Basic procedure to create three-dimensional structures within micro systems technology. The image shows a cut through the planar substrate.

which builds up on techniques that have been developed for micro electronics. Today, micro systems technology is not limited anymore to these techniques, but still the majority of devices is fabricated using flat silicon substrates. Often, creating a micro system is a combination of the following steps.

Starting with the blank substrate (Figure 5 I), a layer of material, e.g. gold, is *deposited* (Figure 5 II) on the substrate, covering the complete surface. Second, a layer of *photoresist* is deposited on the material and is patterned by means of *photolithography* (Figure 5 III). In the next step, the region that is not covered by the photoresist is *etched* (Figure 5 IV). In the end, the complete photoresist is removed (*stripped*) (Figure 5 V). Mostly by repeating steps II-V, complex three dimensional structures can be created. Sometimes, the order of these steps is changed for processes like *electrodeposition* or *lift-off* processes. In addition, complete wafers can be *bonded* to each other.

In the following, the most important techniques used to build the µ-biomimetic IR sensor are presented. More complex sequences will be introduced and analyzed later. The descriptions are not meant to be extensive and refer to the processes and machines used in this work.[3]

2.3.1 Substrates

The bulk material for most processes is single-crystalline silicon. The silicon single crystal is grown by pulling a small mono-crystalline seed crystal out of melted silicon (Czochralski technique). The single crystal rod is cut into *wafers*. Afterwards the wafers are planarized and polished. The concentration of impurities in the single crystal is below $10^{14}\,\mathrm{cm}^{-3}$. Some processes depend on the exact concentration of impurities. To achieve a homogeneous distribution of impurities, a small amount of a dopant (usually phosphor) is added.

[3]Details of micro systems technology can be found e.g. in [45, 46].

The amount of the dopant is larger than the number of intrinsic impurities. This is why the concentration (and the conductivity) is enlarged and less subject to fluctuations. None of the processes used here depends on the crystalline orientation of the single crystal. Therefore only the most common orientation of the wafer surface (100) is used. For all processes, 4" (100 mm) wafers with a thickness of 300 µm or 500 µm are used. In addition to silicon, glass wafers are used for *wafer bonding* (see below).

2.3.2 Deposition

The deposition of new layers of various materials used as electrode, insulation, membrane, etc. is a crucial prerequisite to create micro systems. Such methods can be classified as either chemical or physical. Chemical processes use the creation of material on the substrate by a chemical reaction of gases and/or liquids with each other or with the substrate. In physical deposition processes, the material is directly moved to the substrate surface.

2.3.2.1 Chemical deposition

Chemical deposition includes *chemical vapour deposition* (CVD), *electrodeposition*, and *thermal oxidation* of silicon.

Chemical vapour deposition

For chemical vapour deposition, the substrate is placed in a reactor to which a mixture of gaseous *precursors* is supplied. A chemical reaction takes place between the gas components, and a solid material is created which condenses on all surfaces of the reactor. The two most relevant CVD techniques are the low pressure CVD (LPCVD) and the plasma enhanced CVD (PECVD). They differ in the way by which the required dissociation energy for the gas is supplied. LPCVD processes need a high temperature ranging from 500 °C to 850 °C but produce layers of high uniformity. Furthermore, many wafers (at least 25) can be processed at the same time. In PECVD reactors, the required energy is supplied by means of a plasma discharge. Therefore, temperatures down to 250 °C are possible [45]. The downside is an inferior film quality and a small number of wafers that can be processed simultaneously.

One crucial process for the fabrication of the µ-biomimetic IR sensor is the deposition of silicon nitride (Si_3N_4) layers that function as a free-standing membrane. It is important that the membrane is as even as possible and does not bend without any external force applied. However, already due to the deposition process, the Si_3N_4 layer is exposed to intrinsic stress. Depending on the process parameters and most important on the gas mixture, the intrinsic stress can be varied in a large range. Here, Si_3N_4 layers are deposited using a LPCVD process. The employed precursors are dichlorosilane (SiH_2Cl_2 or DCS) and ammonia (NH_3). By varying the ratio of DCS and ammonia gas flows, the intrinsic stress is adjusted [47, 48]. The ratio of the gas flows directly influences the stoichiometric ratio of silicon and nitride [49]. Stoichiometric silicon nitride has the largest tensile stress of around 1000 MPa [50], whereas silicon rich Si_xN_y films have lower stress values and even compressive stress for large ratios of ammonia to DCS of about 10 [51].

Thermal oxidation

Due to the exposition of silicon to oxygen, a layer of silicon dioxide SiO_2 is formed. The *native* oxide, which grows just due to the exposition of Si to air at room temperature, has a

thickness of about 20 nm. To achieve thicker layers, the substrate is heated to temperatures between 800 °C and 1200 °C using a furnace. For dry oxidation, oxygen and nitrogen is fed into the furnace, for wet oxidation, water vapour is added. The presence of vapour increases the reaction rate and allows for thicker layers.

Electrodeposition

Electrodeposition, also known as *electroplating*, refers to the electrochemical process of depositing metal ions in solution on a substrate. This process is used to create thick (around 5 µm) gold layers. The wafers, which need to have a conductive surface, and a platinum plated titanium anode are immersed in an electrolyte based on sodium gold sulphite ($Na_3Au(SO_3)_2$). In the solution, the sulphite dissolves into Na^+ and $[Au(SO_3)_2]^{3-}$ ions. For the electroplating process, a voltage is applied between the wafer (the cathode) and the anode. In the field of the cathode, the $[Au(SO_3)_2]^{3-}$ ions are polarized and eventually break up. The gold cations (Au^+) are attracted onto the wafer surface and are deposited.

2.3.2.2 Physical deposition

In most cases, physical deposition refers to *physical vapour deposition* (PVD). A purified material is vapourized and condenses on the substrate, forming a thin film. Materials that can be used include different metals and silicon. Silicon deposited by means of PVD usually does not form a single crystal but rather a polycrystalline or amorphous layer. Two PVD methods are used in this work: *thermal evaporation* and *sputtering*.

In thermal evaporation, material is heated by passing a large electrical current through a tungsten filament in vacuum. The vacuum pressure has to be lower than the vapour pressure of the source material to allow for free evaporation. The evaporated material forms a beam and subsequently condenses on the substrate. A surface in the "shadow" of a structure is not reached by the beam. Therefore, sidewalls of elevated structures are not covered. In some cases, this is not a desirable behaviour, but it can be exploited in *lift-off* processes (see Section 4.3).

In contrast to thermal evaporation, in sputtering a *target* is vapourized by bombarding it with argon ions. The ions are accelerated towards the target and knock out material from the target into the chamber. As for evaporation, the material condenses on the wafer surface. As the target size is comparable to the wafer size, it cannot be considered point-sized as for thermal evaporation. Consequently, only undercut surfaces are not coated by the target material. In general, sputtering provides a better sidewall deposition than thermal evaporation.

2.3.3 Photolithography

Photolithography enables the creation of patterned polymer layers. These layers may act as protection for etch processes or as a mold for deposition. The lithography procedure can be divided into three phases: coating, exposure, and development. The following technique was used in this work: First, the substrate (Figure 6 I) is *spin-coated* with photoresist. Some millilitres of resist are dispensed on the substrate which is then rotated with 1000 min^{-1} to 3000 min^{-1} spin speed. Most of the resist is lost during spinning, whereas a homogeneous layer with a thickness between 1 µm and 10 µm remains (Figure 6 II). Second, parts of the resist are exposed to radiation of a specific wavelength. The exposed areas are selected by placing a *photomask* between the light source and the coated substrate. The mask consists

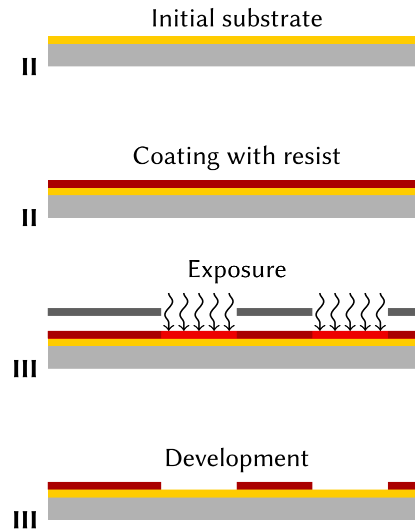

Figure 6: Basic photolithography procedure using a positive resist.

of glass and a patterned layer of chrome. Due to the exposure, the resist changes its chemical properties (Figure 6 III). Third, the resist is placed in a developer solution. Depending on the type of resist, either the exposed or the unexposed parts of the resist are etched away (Figure 6 III). If the exposed area is removed by the developer, the resist is called positive resist. If the unexposed area is removed, the resist is called negative resist.

After each of theses steps, the resist may be baked. After the spin coating, the resist still contains a large amount of solvent. During the *softbake*, the solvent concentration is reduced to about 5 %. This prevents contaminations of the photomask as well as the sticking of the coated wafer to the mask. Furthermore, the resist adhesion and the overall chemical stability is improved. After exposure, the *post exposure bake* is required for special resists like negative resists or to smoothen ripples due to standing light waves. Finally, after developing, the *hardbake* is performed to increase the physical, thermal, and chemical stability of the developed resist.

2.3.3.1 Chemistry of photoresists

The basis for all positive resists used in this work is a resin called Novolac. The etch rate of this resin by a developer is changed by adding a photoactive compound of the group of Diazonaphtoquinone-sulphonates (DNQ). The presence of DNQ strongly reduces the development rate of the resist. When the resist is exposed to blue or ultraviolet radiation, the DNQ transforms into a carboxylic acid and the development rate increases.

In some cases, the pattern of the mask has to be inverted. This can be achieved by using negative or, in this case, *image reversal* resists. Image reversal resists are treated similarly to positive resists except for additional steps. After the first exposure, image reversal resists are baked. The baking step renders the already exposed areas resistant to the developer due to crosslinking. After a *flood exposure* of the complete resist, the hitherto unexposed areas react like normal unexposed positive resist. In the development step, only the resist that was not exposed in the first place is removed.

2.3.3.2 Mask alignment

During a microtechnological process flow, usually more than one lithography step takes place. To fabricate devices with feature sizes down to few µm, the lithography masks have to be carefully aligned to each other. Usually the first mask contains a set of alignment marks that are used to align all other masks. Each mark belongs to one mask. Each subsequent mask only contains one mark, which is aligned to the respective mark of the first mask. As the new mark is also transferred to the substrate, the original mark may become blurred during the following etching step. Therefore, the first mask should contain a mark for each single other mask. The marks are placed on the left- and rightmost side of the wafer to allow for a precise alignment. Often wafers are processed on both sides. In this case, also the first mask that is used for the second side may contain additional alignment marks. The alignment of this mask is done using *back side alignment*, which is more complex and less precise.

2.3.3.3 Choice of resist

Three different resists are used in this work. The AZ1518 (AZ Electronic Materials, Luxembourg) is a thin resist (1 µm to 5 µm) used for most etching processes. It provides a lateral resolution below 1 µm and is easy to handle. When very deep structures ($\gtrsim$ 100 µm) need to be etched, the thickness of AZ1518 is not sufficient. Instead, AZ9260 with a thickness of about 10 µm is used. It is also used for electrodeposition to provide a mold for the deposited metal layer. Disadvantages of AZ9260 are the long development time (6 min) and a reduced resolution compared to AZ1518. Usually, masks are designed in such a way that a positive resist can be used. In some cases, the same pattern is used inverted and non-inverted. For the inverted pattern, the image-reversal resist AZ5214 is used.

2.3.4 Etching

To create three-dimensional structures, parts of the deposited layers have to be removed prior to further deposition processes. Techniques to remove material can be divided into *wet etching* and *dry etching*. For wet etching, the wafers are placed in a solution containing the required components for the desired chemical reaction. Dry etching refers to the usage of a gas or a plasma to achieve chemical or physical etching. In general, wet etching techniques provide a higher selectivity than dry etching techniques, i.e. the etch rate of the material that should be etched is much larger than the etch rate of the other materials. Furthermore, the different etching techniques can be classified as *isotropic* or *anisotropic*. Isotropic processes do not have a preferred etch direction, whereas for anisotropic processes, the etch rate depends on the etch direction.

2.3.4.1 Wet Etching

In this work, wet etching is mostly used for the removal of silicon dioxide (SiO_2). Buffered hydrofluoric acid (BHF) is a solution that isotropically etches SiO_2. It is a mixture of hydrofluoric acid (HF), water, and ammonia fluoride (NH_4F). The addition of ammonia fluoride maintains a constant etch rate.

2.3.4.2 Dry etching

In dry or plasma etching, the etchant is composed of one or more gases. A plasma discharge leads to the production of the etching particles out of the gas. Four different kinds of

particles are distinguished: inert ions (e.g. Ar^+), reactive ions (e.g. O^+), reactive neutrals (e.g. XeF_2), and reactive radicals (e.g. F·).

As inert ions do not react chemically, they provide a pure physical way of etching. For *ion beam etching* (IBE), argon ions are produced in a plasma, which is separated from the substrate. The ions are accelerated towards the substrate and knock out atoms or molecules from the surface. As this process only provides a small selectivity, IBE is also called *ion milling*. Due to the small selectivity, resists and other masking layers are etched at a rate similar to that of the masked material. Additionally, the milling process does not automatically stop when the top layer is removed but rather continues to etch the layers below. Therefore, IBE is only used if no other process is available. Here it is used to structure metal layers.

For *reactive ion etching* (RIE), a reactor with two parallel electrode plates is used. The electrode on which the substrate is placed is smaller than the counter electrode. Upon application of a high frequency voltage, a plasma discharge is started. Due to the larger mobility of electrons compared to ions, more electrons than ions reach the electrodes upon acceleration by the high frequency voltage. The electrodes gain a negative potential compared to the plasma. The voltage between the smaller electrode and the plasma is larger than the voltage between the larger electrode and the plasma [45]. Positively charged ions are therefore strongly accelerated towards the substrate. The subsequent chemical reaction of radicals on the surface is started by the physical bombardment [52] by the ions. Hence, this process is anisotropic. RIE is used to etch silicon oxide and silicon nitride layers. For SiO_2, a mixture of CF_4 and CHF_3 is used. In the plasma, CF_3· radicals are formed that are responsible for the etch process. To etch Si_3N_4, oxygen is added. However, the selectivity of Si_3N_4 over SiO_2 is only 2 to 3, whereas in both cases, the selectivity over silicon is high.

In contrast to standard RIE reactors, where the power is coupled capacitively, it is transferred inductively in *inductively coupled plasma* (ICP) reactors. The plasma is heated by the magnetic field of coils surrounding the reactor. Without the capacitive coupling, there is no large voltage between the substrate and the plasma [52]. In contrast to RIE, ions are therefore less accelerated towards the substrate and the etching process is mostly chemical and isotropic. ICP reactors are used to etch silicon with a mixture of sulfur hexafluoride (SF_6) and oxygen. In the plasma, F· radicals are produced, which penetrate the substrate surface to form gaseous SiF_2· radicals and stable SiF_4 [53].

To achieve highly anisotropic silicon etching, a further modification of the RIE process is used. An example for *deep reactive ion etching* (DRIE) is the *Bosch* process [54]. In this process, the plasma chemistry is continuously switched between isotropic silicon etching and the deposition of a passivation layer. During the etching, ions accelerated towards the substrate physically etch the passivation layer at the bottom of the trench, whereas the passivation on the sidewalls is left intact. However, the F· radicals are not able to etch the passivation layer. Only after the passivation is removed at the bottom, silicon etching starts. During the passivation step, an octafluorocyclobutane (C_4F_8) plasma leads to the deposition of a chemically inert “Teflon”-like material, protecting the sidewalls of the trench.

A purely chemical plasma process is commonly used to strip photoresist. *Barrel etching* is performed in a tube like reactor. Outside the tube, electrodes are located to ignite the plasma. To remove photoresist (*plasma ashing*), oxygen is used, which converts polymers as resist into carbon dioxide (CO_2) and water.

2.3.5 Wafer bonding

Wafer bonding refers to the process of the mechanical fixation of two wafers to each other without the usage of glue. Prior to the bonding, the wafers can be structured. After bonding, the structures are buried between the two surfaces. Depending on the material of the wafers, different processes have to be employed. In this work, two techniques were used. For *anodic bonding*, an electric field assists in the bonding of a silicon and a glass wafer. *Fusion bonding* refers to the direct bonding of two silicon wafers with a thin layer of thermal or native oxide. Although spontaneous bonding occurs when two silicon wafers are brought into contact, additional steps need to be made to ensure a homogeneous and permanent bond.

2.3.5.1 Anodic Bonding

Anodic bonding is usually used to bond Pyrex or a similar glass to silicon. Pyrex has almost the same coefficient of thermal expansion as silicon and contains a sufficient amount of sodium oxide (Na_2O). Prior to the bonding processes, both wafers have to be thoroughly cleaned. Usually, a mixture of hydrogen peroxide (H_2O_2) and sulphuric acid (H_2SO_4), also called *Piranha solution*, is used to clean organic residues off the substrates. Afterwards, the silicon and the glass wafer are placed on top of each other and heated to 450 °C. Due to the elevated temperature, the sodium ions in the glass become mobile. The silicon wafer is located on a plate that serves as anode, whereas a tip-like cathode touches the glass wafer. After the two wafers are pressed together, a voltage of 1200 V is applied between the two electrodes. Positively charged sodium ions (Na^+) drift towards the cathode, leaving a negatively charged depletion region adjacent to the silicon-glass interface. As a result, a high electric field strength between the glass and silicon pulls both wafers together. Due to the high temperature, covalent bounds are formed between the surface atoms of the wafers. A strong and permanent bond between the silicon and glass wafer is established.

2.3.5.2 Fusion Bonding

Fusion bonding is usually employed to bond two silicon wafers. In contrast to anodic bonding, no electric field helps pressing the surfaces together. Even the smallest impurity may prevent the spontaneous bonding of the silicon surfaces. Therefore, the wafers are accurately cleaned using a standardized cleaning procedure. First, the wafers are cleaned using Piranha solution (see above) for ten minutes. In addition, the wafers are cleaned using *RCA1* (Radio Corporation of America) and *RCA2* solutions for ten minutes at 70 °C. RCA1 consists of 1 part ammonium hydroxide (NH_4OH, 25 % aqueous solution), 5 parts deionized water, and one part H_2O_2. It removes further organic dirt. RCA2 consists of 1 part hydrochloric acid (HCl, 25 %), 6 parts water, and one part H_2O_2. It is used to remove metals ions. After the cleaning, the surface of the wafers has a high density of OH groups; it is hydroxylated. Due to the hydroxylation, the surface is hydrophilic and is covered by a thin layer of water molecules. When the two surfaces are brought into contact, the two wafers are bonded by means of hydrogen bonds. Afterwards, the bonded wafers are heated to 450 °C. The hydrogen atoms diffuse through the silicon and the wafers are bonded via covalent bonds between SiO_2 units. Whereas the previous steps are carried out in a wafer bonding machine, the final *annealing* is done in the thermal furnace. The bonded wafers are heated to 1075 °C in a nitrogen atmosphere. At this temperature, also the oxygen from the thermal oxide at the interface diffuses through the silicon. Now the two wafers are inseparably bonded together.

3 Transfer from biology to a sensor concept

The beetle *Melanophila* possesses a sensitive IR detecting organ. When taking the sensitivity measured in behavioural experiments as a basis, no other known biological IR sensor performs significantly better (see Section 2.1.2). Furthermore, the sensitivity calculations based on a historic oil tank fire yield a value of 4×10^{-5} W m^{-2} [15] that is much lower compared to current commercially available pyroelectric detectors with a sensitivity threshold of about 2×10^{-3} W m^{-2} [16].

Most importantly, the beetle receptor has a unique feature amongst other – biological and technical – IR sensors: the integrated compensation mechanism. Nevertheless, many technical sensors require compensation to accommodate changes in ambient temperature. Usually, such changes are filtered electronically. The integrated fluidic compensation mechanism is superior to the electronic filtering: It protects the dendrite in the sensillum or any other transducer in a technological sensor from large pressures. Without the compensation mechanism, a transducer optimized for the highest sensitivity might be distorted by large changes in ambient temperature or even be damaged. With its high sensitivity and the compensation mechanism, the IR receptors of *Melanophila* provide a model for a technical biomimetic uncooled IR sensor. Even if the sensitivity of the beetle was worse than that offered by current IR sensors, it can be further improved by an optimized design. Furthermore, a similar compensation mechanism could enhance other (IR) sensors.

The actual use of a biomimetic IR sensor inspired by *Melanophila* to detect IR radiation is not the only possible application. As explained in Section 2.1.2, the detection mechanism and the sensitivity of the beetle are part of a long lasting discussion. A technical model of the receptors – the biomimetic sensor – can help to further understand their functionality and to end this discussion. In this case, the technical sensor is used to validate model calculations that, in turn, can be applied to the beetle receptor.

In the first step of the development of the biomimetic sensor, the receptor is simplified as much as possible to generate the basic functioning principle of the sensor shown in Figure 7. The sensor consists of two chambers interconnected by a channel. Both chambers have a deflectable piston or a membrane. One chamber acts as the pressure chamber like in the beetle, the other chamber (the compensation chamber) represents the outer compartment. Instead of many short channels connecting the pressure chamber to the outer compartment, a single long compensation channel is used here. Absorption of IR radiation in the pressure chamber leads to the expansion of the liquid contained inside. Depending on the speed of the expansion, the liquid deflects the membrane or flows through the compensation channel. Fast changes of the irradiance lead to a larger deflection of the membrane of the pressure chamber, whereas slow changes are filtered by the compensation mechanism consisting of the channel and the compensation chamber. In general, the

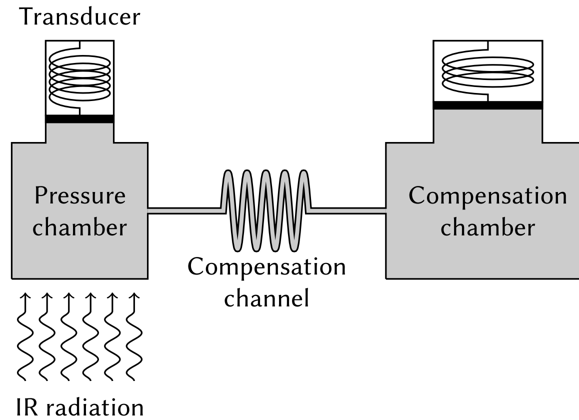

Figure 7: Concept of the biomimetic IR sensor. The pressure chamber (left) absorbs IR radiation and is heated. The resulting pressure increase deflects the membrane. Slow pressure changes are passed to the compensation chamber (right) via the compensation channel.

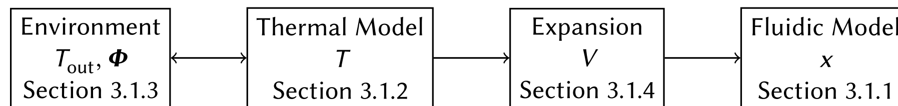

Figure 8: Overview of the theoretical model. Each box corresponds to a distinct part of the model and shows the characterising variable. The arrows indicate the influence of the parts on each other (adapted from Siebke et al. [55]).

membrane of the compensation chamber has to be much more flexible than the membrane of the pressure chamber. Otherwise, a liquid flow through the channel would be prevented. In the following section, a theoretical description of this sensor principle is developed.

3.1 Model description

Based on the sensor principle described in the previous section, a model is derived in this work, which predicts the response of the sensor to IR radiation.[1] To simplify the modelling of the sensor, it is divided into four logical parts (Figure 8). First, the sensor exchanges heat Φ_{in} with the environment. It warms up or cools down, depending on the incident heat flux Φ_{src} from an external source and the temperature difference $\Delta T_{out} = T_{out} - T$ between the sensor and the environment. Second, the absorbed heat is distributed inside the sensor between the two chambers and the remaining sensor volume, described by the thermal model. Third, a change in temperature T leads to a change in the liquid volume V via thermal expansion. Finally, the volume change leads to a deflection x of the membranes and to a liquid flow through the compensation channel, described by the fluidic model. The model will be derived in reverse order, starting with the fluidic model. It can be derived independently of the thermal and environmental part. Then the thermal model and the integration into the environment are derived. Finally, the thermal and the fluidic model are connected.

As described in the previous section, the compensation mechanism does filter slowly changing IR signals, whereas fast changes are not affected. To detect a constant heat flux, it has to be chopped with a suitable modulation frequency f. The chopping frequency of

[1] A description of this model was previously published in Siebke et al. [55].

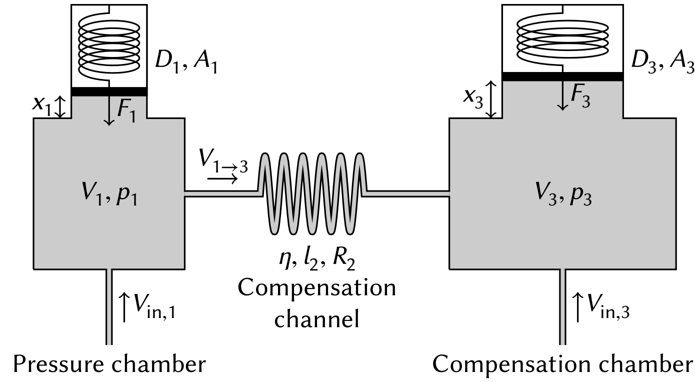

Figure 9: Overview of the fluidic model. If liquid flows into one chamber through an inlet at the bottom, the corresponding piston on top of the chamber is immediately deflected. This leads to a pressure increase due to the deformed spring and a subsequent flow through the compensation channel to the other chamber (from Siebke et al. [55]).

the sensor can be chosen arbitrarily. However, the optimal frequency is a trade-off between speed and sensitivity. Slow chopping leads to a long response time while faster chopping usually results in a decreased sensitivity. The aim of the model is to calculate the frequency spectrum of the sensor response. To simplify the equations, *frequency* is defined as the angular frequency $\omega = 2\pi f$ within the following derivations.

3.1.1 Fluidic model

Figure 9 shows an overview of the fluidic model. The pressure chamber is represented by index 1 and the compensation chamber is represented by index 3. The chambers are connected by a compensation channel, represented by index 2. To be able to accommodate thermal expansion of the liquid, an inlet is added to each chamber. A volume increase due to expansion is then achieved by a flow $V_{\text{in},i}$ through the corresponding inlet.

Generally the deflection x of a membrane is a function of the force F and the position r, $x_\text{r} = x_\text{r}(F, r)$, which is non-linear. For small deflections $x \lesssim d$, the deflection is almost linear. In addition, the shape of the deformed membrane is irrelevant for the behaviour of the model. Therefore, the membrane is approximated by a spring following Hooke's law, $x = F/D$, where D is the spring constant (Figure 10). Instead of the position dependent deflection x_r, the mean deflection

$$x \equiv x_\text{mean} = 2\pi \int_0^R \mathrm{d}r\, r x_\text{r} \left(R^2\pi\right)^{-1} \tag{12}$$

is used, where R is the radius of the membrane. Using the mean deflection ensures that a force F applied to the spring leads to the same volume change as the same force F applied to the membrane. To calculate the spring constant, the behaviour of the membranes is simulated (see Section 3.3.1). With this approximation, it is possible to derive the differential equations describing the fluidic model. The relation between the deflection x_i and the force F_i exerted by the spring on the piston is made by Hooke's law,

$$F_i = D_i x_i. \tag{13}$$

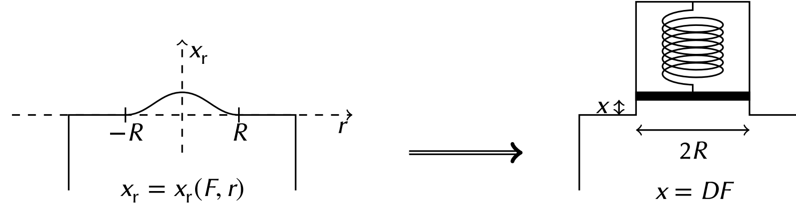

Figure 10: Equivalence of membrane and spring within the model description. In the model, instead of membranes with a complex deflection, springs pushing on a piston described by a single deflection are used.

Inertial forces can be neglected due to the small size of the targeted sensor.[2] Using the area A_i of the piston, the pressure p_i in the liquid is

$$p_i = \frac{F_i}{A_i} = \frac{x_i D_i}{A_i}. \tag{14}$$

The change $\mathrm{d}V_1$ in volume V_1, measured by the deflection of the piston, is given by the difference between the inflow $\mathrm{d}V_{\mathrm{in},1}$ and the outflow through the channel $\mathrm{d}V_{1\to3}$. Analogously, this holds for volume V_3:

$$\mathrm{d}V_1 = A_1\,\mathrm{d}x_1 = \mathrm{d}V_{\mathrm{in},1} - \mathrm{d}V_{1\to3}, \tag{15}$$
$$\mathrm{d}V_3 = A_3\,\mathrm{d}x_3 = \mathrm{d}V_{\mathrm{in},3} + \mathrm{d}V_{1\to3} \tag{16}$$
$$(15, 16) \Rightarrow A_1\,\mathrm{d}x_1 + A_3\,\mathrm{d}x_3 = \mathrm{d}V_{\mathrm{in},1} + \mathrm{d}V_{\mathrm{in},3}\,. \tag{17}$$

Due to the pressure difference between both chambers, liquid flows through the channel. If the cross section of the channel is circular (radius R_2), this process is described by the Hagen–Poiseuille law:

$$\frac{\mathrm{d}}{\mathrm{d}t}V_{1\to3} = \gamma(p_1 - p_3), \tag{18}$$
$$\gamma = \frac{\pi R_2^4}{8\eta l_2}, \tag{19}$$

where η is the dynamic viscosity of the liquid and l_2 the length of the compensation channel. Within micro systems technology, it is more feasible to build rectangular channels. Such channels are accommodated by replacing γ with the following expression [56]:

$$\gamma = \frac{d_2^3 d_2'}{4\eta l_2}\left\{\frac{1}{3} - \frac{d_2}{d_2'}\frac{64}{\pi^5}\sum_{n=1}^{\infty}\tanh\left[(2n-1)\frac{\pi d_2'}{2d_2}\right](2n-1)^{-5}\right\}, \tag{20}$$

d_2 and d_2' being the width and height of the channel, respectively. Using Equation (14), Equation (18) can be rewritten to

$$\frac{\mathrm{d}}{\mathrm{d}t}V_{1\to3} = \gamma\left(\frac{D_1}{A_1}x_1 - \frac{D_3}{A_3}x_3\right). \tag{21}$$

[2] For a water volume $V = 1\,\mathrm{mm}^3$, a frequency $f = 10\,\mathrm{Hz}$, and a spring constant $D = 10\,\mathrm{kN\,m^{-1}}$, the spring force is $D/(\rho V(2\pi f)^2) \simeq 10^6$ times larger than the inertial force.

Combining Equations (15), (16), and (21) yields

$$\gamma\left(\frac{D_1}{A_1}x_1 - \frac{D_3}{A_3}x_3\right) = \frac{\mathrm{d}}{\mathrm{d}t}V_{\mathrm{in},1} - A_1\frac{\mathrm{d}}{\mathrm{d}t}x_1 \tag{22}$$

$$\Rightarrow \gamma\left(\frac{D_1}{A_1}\frac{\mathrm{d}}{\mathrm{d}t}x_1 - \frac{D_3}{A_3}\frac{\mathrm{d}}{\mathrm{d}t}x_3\right) = \frac{\mathrm{d}^2}{\mathrm{d}t^2}V_{\mathrm{in},1} - A_1\frac{\mathrm{d}^2}{\mathrm{d}t^2}x_1. \tag{23}$$

x_3 can be substituted using (17):

$$\gamma\left(\frac{D_1}{A_1}\frac{\mathrm{d}}{\mathrm{d}t}x_1 - \frac{D_3}{A_3^2}\left(\frac{\mathrm{d}}{\mathrm{d}t}V_{\mathrm{in},1} + \frac{\mathrm{d}}{\mathrm{d}t}V_{\mathrm{in},3} - A_1\frac{\mathrm{d}}{\mathrm{d}t}x_1\right)\right) = \frac{\mathrm{d}^2}{\mathrm{d}t^2}V_{\mathrm{in},1} - A_1\frac{\mathrm{d}^2}{\mathrm{d}t^2}x_1 \tag{24}$$

$$\Rightarrow A_1\frac{\mathrm{d}^2}{\mathrm{d}t^2}x_1 + \gamma A_1\left(\frac{D_1}{A_1^2} + \frac{D_3}{A_3^2}\right)\frac{\mathrm{d}}{\mathrm{d}t}x_1 = \frac{\mathrm{d}^2}{\mathrm{d}t^2}V_{\mathrm{in},1} + \gamma\frac{D_3}{A_3^2}\left(\frac{\mathrm{d}}{\mathrm{d}t}V_{\mathrm{in},1} + \frac{\mathrm{d}}{\mathrm{d}t}V_{\mathrm{in},3}\right). \tag{25}$$

By applying the Fourier transform $\mathscr{F}$, the solution for x_1 in the frequency domain is obtained:

$$\hat{x}_1 \equiv \mathscr{F}(x_1)(\omega) = \frac{\mathrm{i}\omega\,\hat{V}_{\mathrm{in},1} + \gamma\frac{D_3}{A_3^2}\left(\hat{V}_{\mathrm{in},1} + \hat{V}_{\mathrm{in},3}\right)}{A_1\,\mathrm{i}\omega + \gamma A_1\left(\frac{D_1}{A_1^2} + \frac{D_3}{A_3^2}\right)}. \tag{26}$$

The circumflex (ˆ) denotes the Fourier transform. As the fluidic model is symmetric, the solution for x_3 is obtained by exchanging the indices 1 and 3.

For an arbitrary frequency ω_0, the volume inflow can be written as $V_{\mathrm{in},i} = V_{\mathrm{in},i,0}\exp(\mathrm{i}\omega_0 t)$. x_i has the same time dependence, $x_i = x_{i,0}\exp(\mathrm{i}\omega_0 t)$. Thus, the Fourier transform of the volume inflow and the deflection is

$$\hat{V}_{\mathrm{in},i} = \sqrt{2\pi}V_{\mathrm{in},i,0}\delta(\omega - \omega_0), \tag{27}$$

$$\hat{x}_i = \sqrt{2\pi}x_{i,0}\delta(\omega - \omega_0), \tag{28}$$

respectively. Inserting (27) and (28) into (26) and solving the time integral yields:

$$\frac{1}{\sqrt{2\pi}}\int \mathrm{d}t\,\hat{x}_1 = x_{1,0} = \frac{\mathrm{i}\omega_0 V_{\mathrm{in},1,0} + \gamma\frac{D_3}{A_3^2}\left(V_{\mathrm{in},1,0} + V_{\mathrm{in},3,0}\right)}{A_1\mathrm{i}\omega_0 + \gamma A_1\left(\frac{D_1}{A_1^2} + \frac{D_3}{A_3^2}\right)}. \tag{29}$$

This equation retains exactly the same form as (26). Therefore, the value of Fourier transform $\hat{x}_i$ and $\hat{V}_{\mathrm{in},i}$ in (26) is interpreted as the amplitude $x_{i,0}$ and $V_{\mathrm{in},i,0}$ for an harmonic oscillation with the frequency $\omega_0 = \omega$. This feature is exhibited due to the linear form of (25) and provides measurable quantities.

To determine the filter characteristics of the compensation mechanism, the behaviour for small and large frequencies needs to be analysed. For large frequencies, the deflection of the membrane of the pressure chamber simplifies to

$$\hat{x}_1(\omega \to \infty) = \frac{\hat{V}_{\mathrm{in},1}}{A_1}. \tag{30}$$

As $\hat{x}_1$ only depends upon $\hat{V}_{\mathrm{in},1}$, the chambers react independently at high frequencies. For low frequencies,

$$\hat{x}_1(\omega \to 0) = \frac{\frac{D_3}{A_3^2}\left(\hat{V}_{\mathrm{in},1} + \hat{V}_{\mathrm{in},3}\right)}{A_1\left(\frac{D_1}{A_1^2} + \frac{D_3}{A_3^2}\right)}. \tag{31}$$

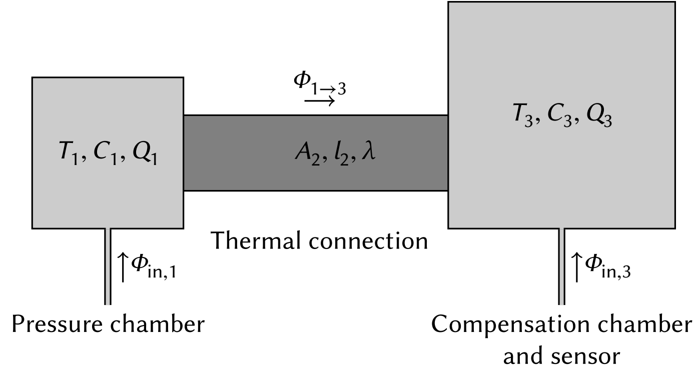

Figure 11: Overview of the thermal model. The left box represents the heat capacity of the liquid filled pressure chamber. The right box represents the heat capacity of compensation volume and the sensor material. The thermal connection describes the heat transfer between the chambers. The inlets represent the heat intake from the outside (from Siebke et al. [55]).

$\hat{x}_1$ depends on the sum of $\hat{V}_{\text{in},1}$ and $\hat{V}_{\text{in},3}$, so the chambers are coupled. Therefore, the compensation channel acts like a low-pass filter. The ratio

$$\delta \equiv \frac{\hat{x}_1(\omega \to 0)}{\hat{x}_1(\omega \to \infty)} = \frac{1}{1 + \frac{D_1}{A_1^2}\frac{A_3^2}{D_3}} \frac{\hat{V}_{\text{in},1} + \hat{V}_{\text{in},3}}{\hat{V}_{\text{in},1}} \equiv \delta' \frac{\hat{V}_{\text{in},1} + \hat{V}_{\text{in},3}}{\hat{V}_{\text{in},1}} \tag{32}$$

describes the distribution of the liquid between the two chambers at low frequencies. Only if $\delta < 1$, the compensation chamber actually relieves the capacitor membrane. For $\delta > 1$, the pressure in the pressure chamber would become even larger at low frequencies. δ' is completely defined by the properties of the fluidic model, whereas $\hat{V}_{\text{in},i}$ depends upon the thermal properties of the sensor and external influences. Two major conclusions for the sensor design can be drawn from (32). First, $V_{\text{in},3}$ has to be as small as possible compared to $V_{\text{in},1}$. Second, δ' can be reduced to improve the compensation. Therefore, the membrane of the pressure chamber should be small and stiff, whereas the membrane of the compensation chamber should be large and flexible. The optimal parameters will be discussed in more detail in Section 4.2.

3.1.2 Thermal model

Figure 11 depicts the thermal model. The left box represents the heat capacity of the pressure chamber, whereas the right box represents the heat capacity of the compensation chamber and the rest of the sensor. The chambers are thermally coupled by the sensor material. The two inlets $\boldsymbol{\Phi}_{\text{in},1}$ and $\boldsymbol{\Phi}_{\text{in},3}$ describe the heat influx from the outside.

For the change $\mathrm{d}T_i$ in temperature T_i, the external inflow $\boldsymbol{\Phi}_{\text{in},i}$ as well as the heat transfer $\boldsymbol{\Phi}_{1\to3}$ from the pressure chamber into the compensation chamber have to be considered:

$$\mathrm{d}T_1 = \frac{\boldsymbol{\Phi}_{\text{in},1} - \boldsymbol{\Phi}_{1\to3}}{C_1}\,\mathrm{d}t, \tag{33}$$

$$\mathrm{d}T_3 = \frac{\boldsymbol{\Phi}_{\text{in},3} + \boldsymbol{\Phi}_{1\to3}}{C_3}\,\mathrm{d}t, \tag{34}$$

$C_{1,3}$ being the heat capacity of the capacitor and compensation chamber, respectively. Using

$$\boldsymbol{\Phi}_i = \frac{\mathrm{d}}{\mathrm{d}t} Q_i \tag{35}$$

leads to

$$C_1 \frac{\mathrm{d}}{\mathrm{d}t} T_1 = \frac{\mathrm{d}}{\mathrm{d}t} Q_{\mathrm{in},1} - \frac{\mathrm{d}}{\mathrm{d}t} Q_{1\to 3}, \tag{36}$$

$$C_3 \frac{\mathrm{d}}{\mathrm{d}t} T_3 = \frac{\mathrm{d}}{\mathrm{d}t} Q_{\mathrm{in},3} + \frac{\mathrm{d}}{\mathrm{d}t} Q_{1\to 3} \tag{37}$$

$$\Rightarrow C_1 \frac{\mathrm{d}}{\mathrm{d}t} T_1 + C_3 \frac{\mathrm{d}}{\mathrm{d}t} T_3 = \frac{\mathrm{d}}{\mathrm{d}t} Q_{\mathrm{in},1} + \frac{\mathrm{d}}{\mathrm{d}t} Q_{\mathrm{in},3} \tag{38}$$

In contrast to the fluidic model, there is no distinct channel in which the heat transfer between the chambers takes place. Here, the chambers are thermally coupled by the sensor material in which the chambers are located. In general, heat transfer is described by Fourier's law for thermal conduction,

$$\boldsymbol{q} = -\lambda \nabla T, \tag{39}$$

where $\boldsymbol{q}$ is the heat flux per area and λ is the thermal conductivity. Each chamber is approximated by a single temperature T_i and the heat flow $\Phi_{1\to 3}$ between the chambers is assumed to be stationary. Therefore, the total heat flow is proportional to the temperature difference $\Delta T_{1\to 3}$ of the chambers:

$$\Phi_{1\to 3} = \lambda' \Delta T_{1\to 3}. \tag{40}$$

For a simple bar, $\lambda' = \lambda A/l$. For more complex cases, λ' is calculated by simulation (see Section 3.3.2). In addition to the heat flow, the heat capacity of the sensor has also to be accounted for. All heat emitted by the pressure chamber is absorbed by the sensor material as well as the compensation chamber. Hence, the heat capacity of the sensor is added to the heat capacity of the compensation chamber. Combining Equation (40) with (36) to eliminate $Q_{1\to 3}$ yields

$$\lambda' T_1 - \lambda' T_3 = \frac{\mathrm{d}}{\mathrm{d}t} Q_{\mathrm{in},1} - C_1 \frac{\mathrm{d}}{\mathrm{d}t} T_1 \tag{41}$$

$$\Rightarrow \lambda' \frac{\mathrm{d}}{\mathrm{d}t} T_1 - \lambda' \frac{\mathrm{d}}{\mathrm{d}t} T_3 = \frac{\mathrm{d}^2}{\mathrm{d}t^2} Q_{\mathrm{in},1} - C_1 \frac{\mathrm{d}^2}{\mathrm{d}t^2} T_1. \tag{42}$$

T_3 is eliminated by (38):

$$\lambda' \frac{\mathrm{d}}{\mathrm{d}t} T_1 - \lambda' \left(\frac{1}{C_3} \left(\frac{\mathrm{d}}{\mathrm{d}t} Q_{\mathrm{in},1} + \frac{\mathrm{d}}{\mathrm{d}t} Q_{\mathrm{in},3} \right) - \frac{C_1}{C_3} \frac{\mathrm{d}}{\mathrm{d}t} T_1 \right) = \frac{\mathrm{d}^2}{\mathrm{d}t^2} Q_{\mathrm{in},1} - C_1 \frac{\mathrm{d}^2}{\mathrm{d}t^2} T_1 \tag{43}$$

$$\Rightarrow C_1 \frac{\mathrm{d}^2}{\mathrm{d}t^2} T_1 + \lambda' \left(1 + \frac{C_1}{C_3} \right) \frac{\mathrm{d}}{\mathrm{d}t} T_1 = \frac{\mathrm{d}^2}{\mathrm{d}t^2} Q_{\mathrm{in},1} + \lambda' \frac{1}{C_3} \left(\frac{\mathrm{d}}{\mathrm{d}t} Q_{\mathrm{in},1} + \frac{\mathrm{d}}{\mathrm{d}t} Q_{\mathrm{in},3} \right). \tag{44}$$

Finally, the Fourier transform is used to calculate the frequency dependent response of the temperature to an external heat source:

$$\hat{T}_1 = \frac{\mathrm{i}\omega \hat{Q}_{\mathrm{in},1} + \lambda' \frac{1}{C_3} \left(\hat{Q}_{\mathrm{in},1} + \hat{Q}_{\mathrm{in},3} \right)}{C_1 \, \mathrm{i}\omega + \lambda' \left(1 + \frac{C_1}{C_3} \right)}. \tag{45}$$

The same holds for T_3 under exchange of the indices 1 and 3.

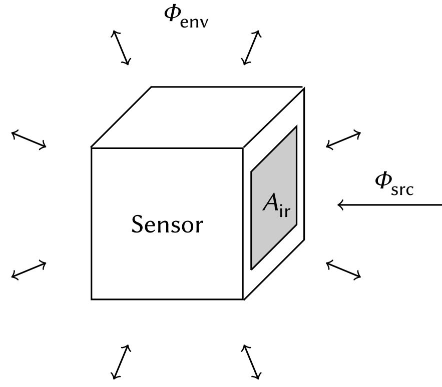

Figure 12: Overview of the environmental model. An external source (Φ_{src}) irradiates the surface of the pressure chamber (A_{ir}). Due to the temperature difference between the sensor and the environment, heat (Φ_{env}) is in general exchanged on the complete sensor surface.

3.1.3 Environment

To complete the model, the heat exchange of the sensor with the environment, i.e. $\hat{Q}_{in,i}$, is taken into account. The whole heat exchange is split in two parts. On the one hand, the sensor absorbs radiation $\boldsymbol{\Phi}_{src}$ that is emitted by a distant heat source, e.g. a forest fire (Figure 12). On the other hand, the sensor emits or absorbs heat $\boldsymbol{\Phi}_{env}$ due to the temperature difference to the environment. Within this, the total heat flux is

$$\boldsymbol{\Phi}_{in,i} = \boldsymbol{\Phi}_{src,i} + \boldsymbol{\Phi}_{env,i} = \frac{d}{dt} Q_{in,i}. \tag{46}$$

The radiant heat absorbed from the remote source is proportional to the fraction of the absorbing area $\boldsymbol{A}_{ir,i}$ perpendicular to the irradiance $\boldsymbol{E}_e$:

$$\boldsymbol{\Phi}_{src,i} = \varepsilon_i \boldsymbol{A}_{ir,i} \cdot \boldsymbol{E}_e, \tag{47}$$

ε_i being the emissivity of the surface of the chamber. The radiant heat exchanged due to different temperatures is given by the Stefan-Boltzmann law:

$$\boldsymbol{\Phi}_{env,i} = \varepsilon_i A_{ir,i} \sigma \left(T_{out}^4 - T_i^4 \right). \tag{48}$$

As described in Section 3.1.1, the heat intake of the compensation chamber should be as small as possible. To prevent absorption of heat outside the pressure chamber, the sensor should be appropriately shielded. This can be accomplished e.g. by use of a reflective layer with a transmissive window at the pressure chamber. It is assumed that the sensor only absorbs IR radiation at the window of the pressure chamber and completely reflects the radiation on the rest of the sensor area, i.e.

$$\varepsilon_3 \simeq 0 \quad \text{(for IR radiation)} \tag{49}$$

$$\Rightarrow \frac{d}{dt} Q_{in,3} \simeq 0. \tag{50}$$

The Stefan-Boltzmann equation is linearized by employing the first order Taylor approximation of T_1^4 and T_{out}^4 around a mean temperature T_0:

$$T^4 \simeq T_0^4 + 4T_0^3 (T - T_0) \tag{51}$$

$$\Rightarrow \frac{\mathrm{d}}{\mathrm{d}t} Q_{\mathrm{in},1} \simeq \Phi_{\mathrm{src}} + 4\varepsilon A_{\mathrm{ir}} \sigma T_0^3 (T_{\mathrm{out}} - T_1) \tag{52}$$

$$\equiv \Phi_{\mathrm{src}} + \sigma' (T_{\mathrm{out}} - T_1). \tag{53}$$

For a mean temperature of $T_0 = 300\,\mathrm{K}$ (room temperature) and a difference of $\Delta T = 10\,\mathrm{K}$ (approx. day-night cycle), the deviation of Equation (51) compared to Equation (48) is only 5 %. Finally the Fourier transform of the heat inflow can be obtained:

$$\mathrm{i}\omega\, \hat{Q}_{\mathrm{in},1} = \hat{\Phi}_{\mathrm{src}} + \sigma' (\hat{T}_{\mathrm{out}} - \hat{T}_1). \tag{54}$$

Inserting Equations (50) and (54) into Equation (45) for T_1 yields

$$\Rightarrow \hat{T}_1 = \frac{\mathrm{i}\omega \left(\hat{\Phi}_{\mathrm{src}} + \sigma'(\hat{T}_{\mathrm{out}} - \hat{T}_1)\right) + \lambda' \frac{1}{C_3} \left(\hat{\Phi}_{\mathrm{src}} + \sigma'(\hat{T}_{\mathrm{out}} - \hat{T}_1)\right)}{\underbrace{C_1 (\mathrm{i}\omega)^2 + \lambda' \left(1 + \frac{C_1}{C_3}\right) \mathrm{i}\omega}_{\mathcal{N}_1}} \tag{55}$$

$$\Rightarrow \hat{T}_1 \left(1 + \frac{\sigma' \,\mathrm{i}\omega + \lambda' \frac{1}{C_3} \sigma'}{\mathcal{N}_1}\right) = \frac{\mathrm{i}\omega \hat{\Phi}_{\mathrm{src}} + \sigma' \,\mathrm{i}\omega \hat{T}_{\mathrm{out}} + \lambda' \frac{1}{C_3} (\hat{\Phi}_{\mathrm{src}} + \sigma' \hat{T}_{\mathrm{out}})}{\mathcal{N}_1} \tag{56}$$

$$\Rightarrow \hat{T}_1 \left(\mathcal{N}_1 + \sigma' \,\mathrm{i}\omega + \lambda' \frac{1}{C_3} \sigma'\right) = \mathrm{i}\omega \hat{\Phi}_{\mathrm{src}} + \sigma' \,\mathrm{i}\omega \hat{T}_{\mathrm{out}} + \lambda' \frac{1}{C_3} (\hat{\Phi}_{\mathrm{src}} + \sigma' \hat{T}_{\mathrm{out}}) \tag{57}$$

$$\Rightarrow \hat{T}_1 = \frac{\mathrm{i}\omega \hat{\Phi}_{\mathrm{src}} + \sigma' \,\mathrm{i}\omega \hat{T}_{\mathrm{out}} + \lambda' \frac{1}{C_3} (\hat{\Phi}_{\mathrm{src}} + \sigma' \hat{T}_{\mathrm{out}})}{\underbrace{C_1 (\mathrm{i}\omega)^2 + \lambda' \left(1 + \frac{C_1}{C_3}\right) \mathrm{i}\omega + \sigma' \,\mathrm{i}\omega + \lambda' \frac{1}{C_3} \sigma'}_{\mathcal{N}_2}}. \tag{58}$$

Inserting Equations (50) and (54) into Equation (45) for T_3 yields

$$\hat{T}_3 = \frac{\lambda' \frac{1}{C_1} \left(\hat{\Phi}_{\mathrm{src}} + \sigma'(\hat{T}_{\mathrm{out}} - \hat{T}_1)\right)}{C_3 (\mathrm{i}\omega)^2 + \lambda' \left(1 + \frac{C_3}{C_1}\right) \mathrm{i}\omega}. \tag{59}$$

Using Equation (58), the following formula can be derived:

$$\hat{T}_1 - \hat{T}_{\mathrm{out}} - \frac{1}{\sigma'} \hat{\Phi}_{\mathrm{src}} = \frac{\mathrm{i}\omega \hat{\Phi}_{\mathrm{src}} + \sigma' \,\mathrm{i}\omega \hat{T}_{\mathrm{out}} + \lambda' \frac{1}{C_3} (\hat{\Phi}_{\mathrm{src}} + \sigma' \hat{T}_{\mathrm{out}})}{\mathcal{N}_2} - \frac{\mathcal{N}_2 \left(\hat{T}_{\mathrm{out}} + \frac{1}{\sigma}' \hat{\Phi}_{\mathrm{src}}\right)}{\mathcal{N}_2} \tag{60}$$

$$= -\frac{\mathcal{N}_1 \hat{T}_{\mathrm{out}} + \mathcal{N}_1 \frac{1}{\sigma'} \hat{\Phi}_{\mathrm{src}}}{\mathcal{N}_2}. \tag{61}$$

Inserting into Equation (59) leads to final equation for $\hat{T}_3$:

$$\Rightarrow \hat{T}_3 = \frac{\lambda' \frac{1}{C_1} \mathcal{N}_1 \left(\sigma' \hat{T}_{\mathrm{out}} + \hat{\Phi}_{\mathrm{src}}\right)}{\left(C_3 (\mathrm{i}\omega)^2 + \lambda' \left(1 + \frac{C_3}{C_1}\right) \mathrm{i}\omega\right) \mathcal{N}_2} \tag{62}$$

$$= \frac{\lambda' \frac{1}{C_1} \mathcal{N}_1 \left(\sigma' \hat{T}_{\mathrm{out}} + \hat{\Phi}_{\mathrm{src}}\right)}{\frac{C_3}{C_1} \mathcal{N}_1 \mathcal{N}_2} \tag{63}$$

$$= \frac{\lambda' \frac{1}{C_3} \left(\sigma' \hat{T}_{\mathrm{out}} + \hat{\Phi}_{\mathrm{src}}\right)}{C_1 (\mathrm{i}\omega)^2 + \lambda' \left(1 + \frac{C_1}{C_3}\right) \mathrm{i}\omega + \sigma' \,\mathrm{i}\omega + \lambda' \frac{1}{C_3} \sigma'}. \tag{64}$$

For low frequencies and in the absence of a source, the equations simplify to $\hat{T}_i = \hat{T}_{\text{out}}$. The temperatures of both chambers are the same as the ambient temperature. For high frequencies, the temperature in the pressure chamber is given by

$$\hat{T}_1 = \frac{\hat{\Phi}_{\text{src}} + \sigma' \hat{T}_{\text{out}}}{C_1 \, \mathrm{i}\omega}. \tag{65}$$

This behaviour is as expected, since a shorter exposure to a heat source implies less energy transferred.

3.1.4 Expansion

Finally the thermal model has to be linked to the fluidic model. The thermal model predicts the temperature of the chambers, whereas the fluidic model uses volume flow. The link is made by linear thermal expansion:

$$\mathrm{d}V_i = \alpha V_{i,0} \, \mathrm{d}T_i \tag{66}$$
$$\equiv \alpha_i' \, \mathrm{d}T_i \tag{67}$$
$$\Rightarrow \hat{V}_i = \alpha_i' \hat{T}_i, \tag{68}$$

where α and $V_{i,0}$ are the coefficient of volumetric expansion and the volume of the chambers, respectively. For the fluidic model, the volume change $\mathrm{d}V_i$ is equivalent to an inflow $\mathrm{d}V_{\text{in},i}$ into the according chamber. This link completes the theoretical model of the µ-biomimetic IR sensor.

3.2 Model predictions

With the theoretical model, it is possible to predict the frequency spectrum of the sensor. The next section covers the overall form of the frequency spectrum. Prior to that, some general remarks need to be made.

The temperature inside the chambers only depends on the sum of $\sigma' \hat{T}_{\text{out}}$ and $\hat{\Phi}_{\text{src}}$ (see Equation (58) and Equation (64)) and no other combination. Hence a change in the ambient temperature T_{out} is equivalent to a change in the heat flux Φ_{src}; it is sufficient to analyse the sensor's response to either of them. In the following analyses, a constant amplitude of $\hat{T}_{\text{out}} = 1\,\text{K}$ is used. Instead, using Equation (54), this could be achieved by setting $\hat{\Phi}_{\text{src}} = \sigma' \hat{T}_{\text{out}}$. So, the graphs in the next sections are read in the following way: Assume that the ambient temperature or the power of the external heat source oscillates with the frequency ω and an amplitude of $\hat{T}_{\text{out}}$ or $\hat{\Phi}_{\text{src}}$, respectively. Then the temperature or the deflection oscillates at the same frequency with the amplitude $\hat{T}$ or $\hat{x}$, respectively. Since the model is linear, the response scales with the excitation. In the following, the model parameters are arbitrarily chosen in a way to visualize the analysis.

3.2.1 Sensor response

The structure of the frequency spectrum of the sensor response is very complex. This is due to the influence of the fluidic low-pass filter (see Section 3.1.1), the thermal low-pass filter (see Section 3.1.2), and the heat exchange with the environment (see Section 3.1.3). For a better understanding, each of these parts is analysed individually. Figure 13 describes the influence of the different parts on the sensor response.

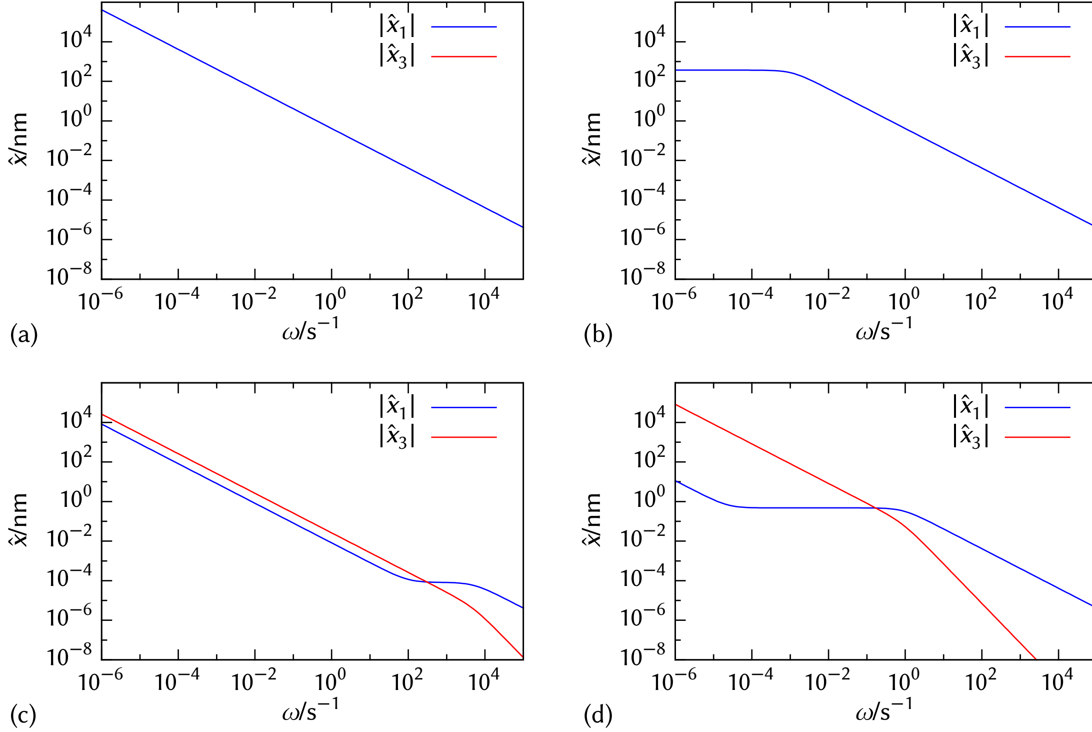

Figure 13: Frequency spectrum of the membrane deflections for different parts of the model. x_1 and x_3 are the deflection of the membrane of the pressure chamber and the compensation chamber, respectively. (a) Only absorption of radiation from an external source. The compensation mechanism, the heat transfer inside the sensor and the heat exchange with the environment are disabled ($x_3 = 0$). (b) Only heat exchange with the environment enabled ($x_3 = 0$). (c) Only heat transfer inside the sensor enabled. (d) Only compensation mechanism enabled.

In Figure 13(a), only the external source is present; the compensation mechanism, the heat transfer inside the sensor, and the heat exchange with the environment are switched off by setting $\gamma = \lambda' = \sigma' = 0$.[3] A smaller frequency ω corresponds to a longer time period, and thus more energy is emitted by the external source during one period. As neither heat nor liquid are transported from the pressure chamber to the compensation chamber, the deflection $\hat{x}_1$ increases linearly with the period. Therefore, the deflection $\hat{x}_1$ is proportional to $1/\omega$ and $\hat{x}_3 = 0$ (Figure 13(a)).

Figure 13(b) shows the influence of the heat exchange with the environment (see Section 3.1.3). At high frequencies, the temperature of the sensor only changes very little. Thus Figure 13(a) and Figure 13(b) are identical at high frequencies. If the frequency decreases, the sensor's temperature rises until it emits heat at the same rate as it absorbs. The sensor reaches a thermal equilibrium with the outside and is not able to heat up further.

When heat is transferred inside the sensor (Figure 13(c)), also the compensation chamber heats up (see Section 3.1.2). For low frequencies, the heat absorbed inside the pressure chamber is distributed across the sensor, resulting in a thermal equilibrium. Therefore, the temperature in both chambers is the same and the deflection differs by a constant factor (parallel lines in Figure 13(c)). At high frequencies, the absorbed heat cannot be transferred fast enough. As a result, the temperature in the pressure chamber increases faster than in

[3]Note that $\gamma = \lambda' = \sigma' = 0$ is not realizable for the sensor. It is only used here to simplify the understanding of the frequency spectrum.

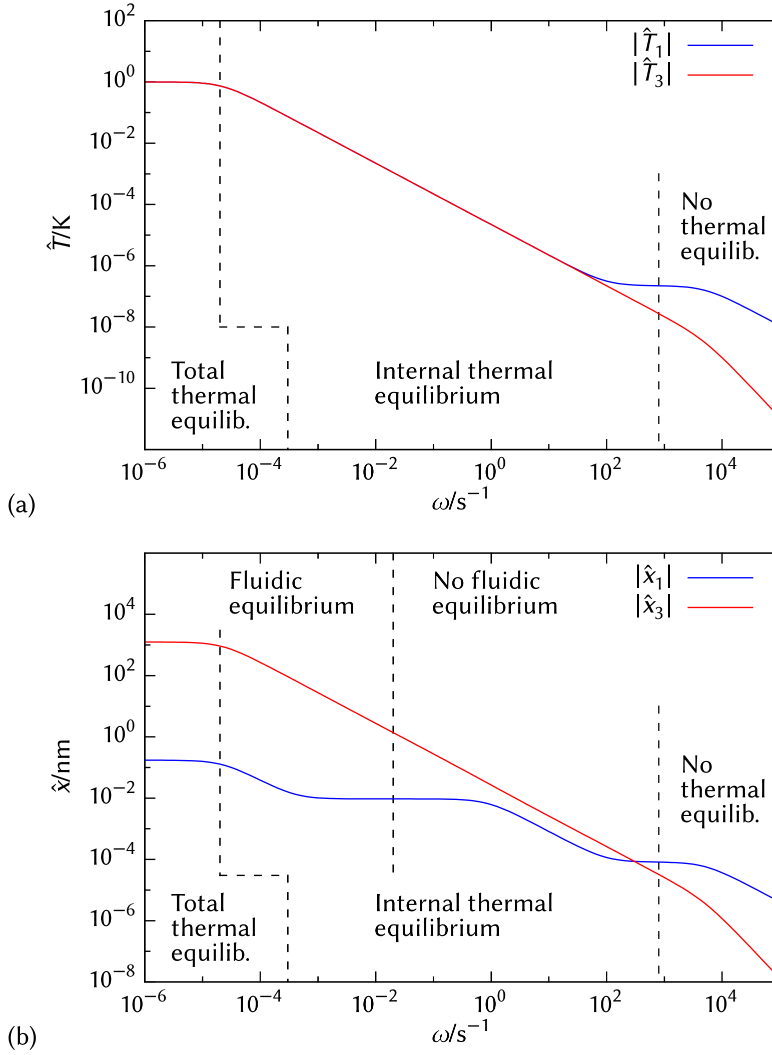

Figure 14: Complete frequency spectrum of the sensor response. The calculations are made using $\hat{T}_{\mathrm{out}} = 1\,\mathrm{K}$. (a) Amplitude $|\hat{x}_i|$ of the deflection. (b) Amplitude $|\hat{T}_i|$ of the temperature. Index 1 and 3 refer to the pressure and compensation chamber, respectively.

the compensation chamber. This leads to a larger difference of $\hat{x}_1$ and $\hat{x}_3$. Therefore, the thermal connection of the two chambers is described by a thermal low-pass filter.

The effect of the compensation mechanism (Figure 13(d), see Section 3.1.1) is similar to that of the thermal low-pass filter. At very low frequencies ($\lesssim 10^{-4}\,\mathrm{s}^{-1}$), the volume increases so slowly that the pressure inside the pressure chamber induces a liquid flow into the compensation chamber. A "fluidic equilibrium" is established – the pressure in both chambers is the same – similar to the thermal equilibrium mentioned above. At higher frequencies, the transport is reduced ($10^{-4}\,\mathrm{s}^{-1} \lesssim \omega \lesssim 1\,\mathrm{s}^{-1}$) and finally virtually blocked ($\gtrsim 1\,\mathrm{s}^{-1}$).

Figure 14 visualizes the combination of the fluidic low-pass filter, the thermal low-pass filter, and the heat exchange with the environment. As the compensation mechanism does not influence the temperatures in this simplified view, the temperature spectrum (Figure 14(b)) has a different structure than the deflection spectrum (Figure 14(a)). The temperature spectrum shows three distinct regions. At low frequencies, the incident radiation intensity changes so slowly that the sensor is in thermal equilibrium with its environment.

The sensor reaches a maximum temperature depending on the ambient temperature and the incident heat flux, independently of the frequency. At medium frequencies, the sensor cannot heat up and cool down as fast as the ambient temperature changes. Higher frequencies lead to lower absorption of heat. Thus the temperature amplitude decreases. At high frequencies, the heat input changes so fast that the sensor itself cannot establish a thermal equilibrium. There is not enough time for the heat exchange between the chambers. This is why the temperature amplitude of the compensation chamber is always lower than the temperature amplitude of the pressure chamber.

In contrast to the temperature spectrum, the deflection spectrum is influenced by the compensation mechanism. At low frequencies, the volume increase is distributed between both chambers, maintaining the same pressure. The fractions of liquid that are present in the chambers depend solely on the properties of the membranes. At high frequencies, the compensation mechanism, which acts as a low-pass filter, blocks the transport of liquid. A fast volume change is not transported into the compensation chamber (see also below).

At the higher cut-off frequency of both low-pass filters, both filters block. As long as one of the filters is "conducting", liquid or heat are transported into the compensation chamber. As heat transfer also results in a volume increase, the filters are connected as in a parallel circuit. The properties of the thermal filter are defined by the overall dimension of the sensor and the material. In contrast, the cut-off frequency of the fluidic filter can be easily adapted. Hence it is important and sufficient to further characterize only the fluidic low-pass filter.

3.2.2 Fluidic low-pass filter

The properties of the fluidic low-pass filter can be easily changed during the manufacturing process. For this reason, a precise description of the cut-off frequency and the damping are of particular interest. The damping of the fluidic low-pass filter can be described by comparing the model with and without the low-pass filter. The deflection without the low-pass filter can be obtained by setting $\gamma = 0$. The normalized deflection $\tilde{x}_1$ is defined as the ratio of the deflection with $\gamma \neq 0$ and the deflection with $\gamma = 0$:

$$\tilde{x}_1 \equiv \frac{|\hat{x}_1|}{\left|\hat{x}_1\right|_{\gamma=0}\right|} \Rightarrow \tilde{x}_1^2 = \frac{\omega^2 + \gamma^2 \frac{D_3^2}{A_3^4}\left(\frac{|\hat{V}_{\text{in},1}+\hat{V}_{\text{in},3}|}{|\hat{V}_{\text{in},1}|}\right)^2}{\omega^2 + \gamma^2\left(\frac{D_1}{A_1^2}+\frac{D_3}{A_3^2}\right)^2}. \tag{69}$$

The cut-off-frequency is now defined as the inflection point of $\tilde{x}_1^2$ (see also Figure 13(d)):

$$\frac{\mathrm{d}^2}{\mathrm{d}\omega^2}\tilde{x}_1^2\Big|_{\omega=\omega_c} = 0. \tag{70}$$

As the cut-off frequency of the fluidic filter is smaller than the cut-off frequency of the thermal filter (Figure 14(a)), a thermal equilibrium is assumed for the following calculations, i.e. $\hat{T}_1 = \hat{T}_3$. Hence,

$$\frac{|\hat{V}_{\text{in},1} + \hat{V}_{\text{in},3}|}{|\hat{V}_{\text{in},1}|} = \frac{\alpha_1' + \alpha_3'}{\alpha_1'} \equiv \alpha'' = \text{const.} \tag{71}$$

Carrying out Equation (70) finally leads to the cut-off frequency ω_c:

$$\frac{\mathrm{d}^2}{\mathrm{d}\omega^2}\tilde{x}_1^2\Big|_{\omega=\omega_c} = \frac{\mathrm{d}^2}{\mathrm{d}\omega^2} \left. \frac{\omega^2 + \gamma^2 \frac{D_3^2}{A_3^4} \alpha''^2}{\omega^2 + \gamma^2 \left(\frac{D_1}{A_1^2} + \frac{D_3}{A_3^2}\right)^2} \right|_{\omega=\omega_c} \tag{72}$$

$$\Rightarrow \omega_c^2 = \frac{1}{3}\gamma^2 \left(\frac{D_1}{A_1^2} + \frac{D_3}{A_3^2}\right)^2 . \tag{73}$$

The damping at the cut-off is

$$\tilde{x}_{c,1}^2 \equiv \tilde{x}_1^2(\omega^2 = \omega_c^2) = \frac{1}{4} + \frac{3}{4} \frac{\left(1 + \frac{\hat{V}_{\mathrm{in},3}}{\hat{V}_{\mathrm{in},1}}\right)^2}{\left(1 + \frac{D_1}{D_3}\frac{A_3^2}{A_1^2}\right)^2} . \tag{74}$$

If $\tilde{x}_{c,1} < 1$, the low-pass filter leads to a reduction of the amplitude at low frequencies (see also Section 3.1.1). If $\tilde{x}_{c,1} > 1$, the deflection increases due to the low-pass filter. For the biomimetic IR sensor, $\tilde{x}_{c,1} < 1$ is desired. Similar to the beetle, the fluidic low-pass filter should allow for a slow exchange of liquid between the chambers and prevent the build-up of a large pressure, while fast volume changes lead to a deflection of the membrane. This can be achieved by choosing suitable sensor parameters.

3.3 Simulation of the membranes and the heat transfer

In the previous section, a model describing the response of the biomimetic sensor was derived. However, the model does neither predict the precise membrane deflection depending on the pressure nor the heat transfer depending on the temperature difference. The membranes are approximated by springs with spring constant D and the heat transfer is approximated by a linear coefficient λ'. Both are calculated by simulation using COMSOL Multiphysics (Version 4.4, COMSOL Multiphysics, Germany).

3.3.1 Simulation of the membrane deflection

Throughout this work, membranes made of PDMS (polydimethylsiloxane) and Si_3N_4 (silicon nitride). Silicon nitride is used to provide stiff membranes, whereas PDMS is used for flexible membranes and when silicon nitride is not feasible. The deflection of a membrane with radius R and thickness t depends on the Young's modulus E, the Poisson ratio ν, and the residual stress σ of the membrane. For Si_3N_4, the Young's modulus depends very little on the fabrication process, whereas the residual stress can be adjusted from large tensile stress of about 1000 MPa even down to compressive stress. The mechanical properties of PDMS largely depend on the exact composition, the curing temperature, and the thickness. Table 2 sums up the properties of the two materials.

The general setup of the simulation is shown in Figure 15(a). It exploits the rotational symmetry around the centre of the membrane. The border of the membrane is kept fixed while the membrane is deformed by a varying pressure applied at the bottom. To calculate the spring constant D, the total force $F = pR^2\pi$ and the mean deflection

$$x = 2\pi \int_0^R \mathrm{d}r\, r x_r \left(R^2\pi\right)^{-1}$$

	E	ν	ρ/kg m^{-3}	σ/MPa
Si_3N_4	290 GPa[a]	0.24[b]	3100[c]	870[d]
PDMS	1.9 MPa to 5.4 MPa[e]	0.50[f]	1030[f]	0

Table 2: Properties of the Si_3N_4 and PDMS (Sylgard 184) layers used to simulate the membrane. E is the Young's modulus, ν is the Poisson ratio, ρ is the density, σ is the residual stress. Positive values of σ mean tensile stress, negative values mean compressive stress. As the stress of the PDMS layers is unknown, no stress is simulated. [a][57], [b][58], [c][59], [d]measured, [e]see Table 5, [f][60].

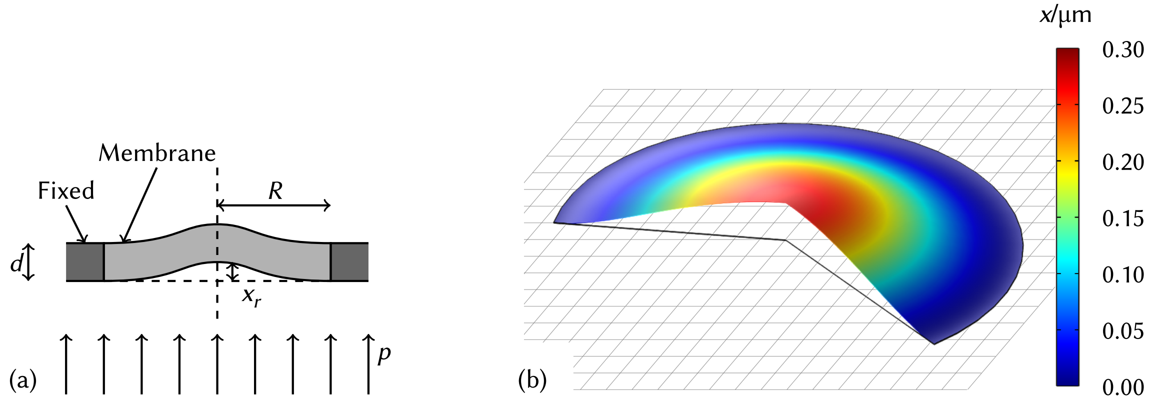

Figure 15: COMSOL Multiphysics simulation for the membrane deflection. The simulation determines the deformation depending upon the applied pressure. (a) The membrane is represented as a layer of material fixed at the edges. The simulation exploits the rotational symmetry of the setup. (b) Cut through a deformed Si_3N_4 membrane for a fixed pressure. In the centre (red) the deformation is the largest, at the edge (blue), there is no deformation (from Siebke et al. [55]).

are extracted from the simulated scenario. Figure 16 shows the results for a Si_3N_4 membrane with different stress values. Apart from the red curve ($\sigma = 0$), the deflection depends linearly on the force in the shown region. As will be described later, deflections larger than 1 µm with possibly non-linear behaviour do not occur for the Si_3N_4 membrane . Therefore the membrane of the sensor can be replaced by a spring in the model with virtually any error. The spring constant is calculated using the values for a deflection of 1 µm:

$$D = \frac{F(x = 1\,\mu\text{m})}{1\,\mu\text{m}}. \tag{75}$$

Table 3 shows the resulting spring constants for the membranes in Figure 15(a). Note that for $\sigma = 0$, the spring constant does not describe the deviations from the linear behaviour.

The same simulation and calculation procedure is applied to the PDMS membranes. The applicable values will be presented in Sections 3.4.4, 6.4, and 7.2.

3.3.2 Simulation of the heat transfer

An analytical calculation of the heat transfer in objects is only possible for simple geometries as bars. In such cases, it can be described as

$$\Phi = \lambda \frac{A}{l} \Delta T, \tag{76}$$

where A is the cross-section and l the length of the bar. For more complex geometries like the sensor, the heat transfer must be calculated numerically. As for the membrane,

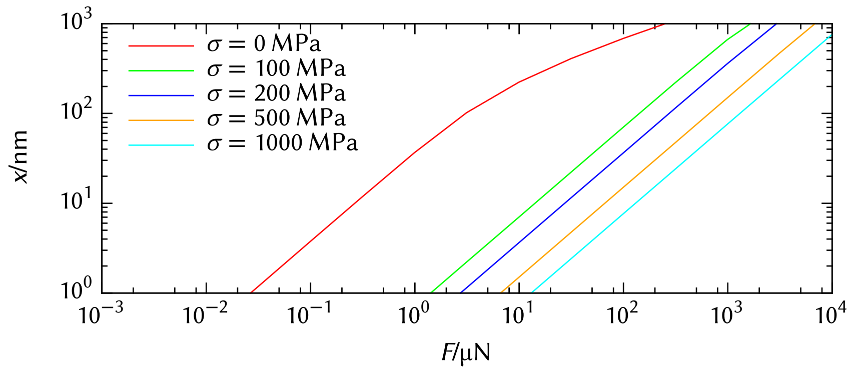

Figure 16: Simulation of the deflection of a Si_3N_4 membrane. Radius $R = 250\,\mu m$ and thickness $t = 500\,nm$ were fixed while different values for the stress σ were simulated.

σ/MPa	D/N m^{-1}
100	1600
200	2927
500	6740
1000	13 262

Table 3: Resulting spring constants for Si_3N_4 membranes with different stress values. Radius $R = 250\,\mu m$ and thickness $t = 500\,nm$.

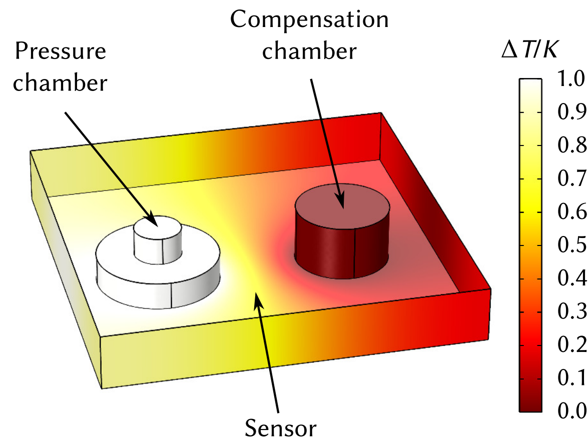

Figure 17: View of the sensor model for the simulation of heat transfer. The left chamber belongs to the capacitor, the right chamber is the compensation chamber. The colour code shows the temperature difference ΔT relative to the compensation chamber. The simulation calculates the heat flux transferred from the capacitor to the compensation cavity (from Siebke et al. [55]).

the setup is simulated using COMSOL Multiphysics. Figure 17 shows the simulated setup for the biomimetic sensor. It contains the bulk material of the sensor that consists of two chambers. The temperatures of both chambers are fixed to a constant difference. Using the simulation program, the stationary solution for the heat flux is obtained. It is assumed that upon a change of temperature of a chamber, a constant heat flow is instantaneously established. The combined coefficient of thermal conduction is calculated as

$$\lambda' = \frac{\Phi}{\Delta T}. \tag{77}$$

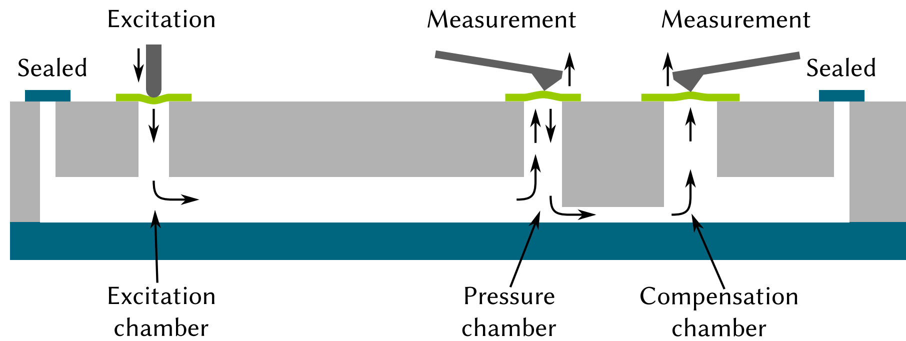

Figure 18: Concept of the chip to validate the fluidic low-pass filter. Side view of the fluidic system. Upon excitation by a piezo actuator, liquid is displaced in the pressure chamber and slowly flows also into the compensation chamber. The deflection of the membrane is measured using AFM. Not to scale; the channel between the pressure and compensation chamber has the same height as the other channels but is narrower.

3.4 The fluidic low-pass filter

The fluidic low-pass filter (the compensation mechanism) is a key feature of the biomimetic IR sensor. In Section 3.1, the modulation frequency dependent response of the sensor including the compensation mechanism was derived. Is was shown that the compensation mechanism can be described as a fluidic low-pass filter. To validate the model calculations and simulated values of the spring constants as shown in Section 3.3.1, a dedicated test of this fluidic filter is performed in this section.[4]

To test the fluidic low-pass filter, silicon chips were designed and fabricated. These chips mimic the fluidic system of the biomimetic sensor (see also Figure 9). The expansion of the liquid is emulated by periodically pumping liquid into the pressure chamber and the subsequent deflection of the membranes of the pressure and compensation chamber is measured.

3.4.1 Chip design

Figure 18 shows the general layout of the fluidic system used for the experimental verification of the fluidic low-pass filter. It contains a pressure chamber and a compensation chamber interconnected by a small channel similar to the compensation channel in the sensor and in the beetle. Instead of periodically heating and cooling the pressure chamber by IR radiation, the liquid volume is changed using a third chamber. The so-called excitation chamber is connected to the pressure chamber by a broad channel. Upon deflection of the membrane of the excitation chamber by an external force, the liquid inside is immediately displaced to the pressure chamber. The openings at both ends are used to fill the system with water bubble-free (see Section 4.4). During the experiment, they are sealed with glass.

The design of Figure 18 is realized using silicon chips with different sizes of the pressure and compensation chamber (see Figure 19). The size of the chips is set to 75 mm × 25 mm, the size of standard microscope slides. Each chip contains three independent fluidic systems, differing by the diameter of the pressure and compensation chamber.[5] The fabrication of the chips is done as follows:[6] First the channels (blue structures in Figure 19) are

[4]Parts of this section were previously published in Siebke et al. [61].
[5]A detailed description of the masks can be found in Appendix B.
[6]More details of the process can be found in Appendix A.

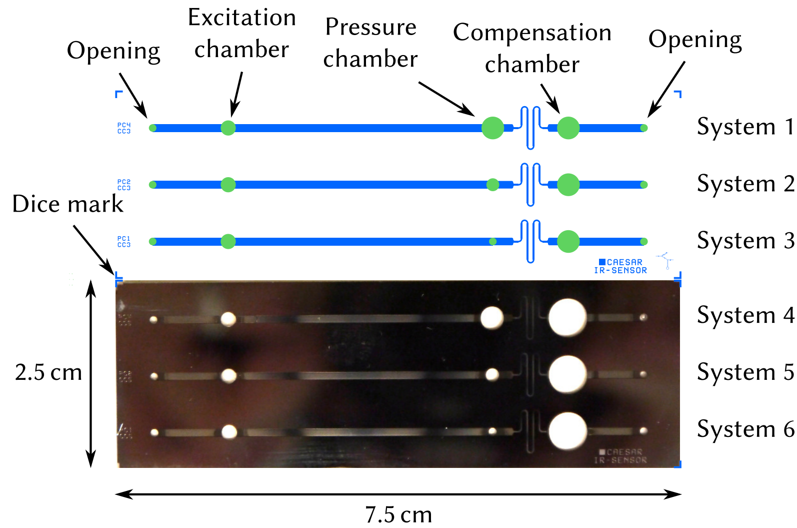

Figure 19: Design of the chip to validate the fluidic low-pass filter. View of the lithography masks for the microtechnological process and photography of one complete Si-chip. Blue: Channels and dice marks. Green: Openings and chambers. Each chip contains three independent systems with different geometries; two different chips are produced.

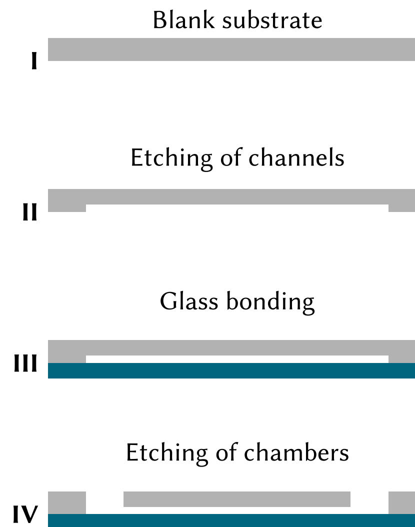

Figure 20: Simplified process flow of the chip to validate the fluidic low-pass filter. Not to scale.

etched into a silicon wafer from the bottom side (Figure 20 I). The depth of the channel is set by varying the etching time during processing. Then a glass wafer is bonded anodically to the Si wafer to close the channels (Figure 20 II). Finally the chambers are etched from the top side through the whole Si wafer (Figure 20 III). After the chips are cut along the dice marks, the PDMS membranes are attached to close all three chambers. All membranes are made of PDMS (Sylgard 184, Dow Corning, USA) in different thicknesses. Membranes with a thickness of 50 µm and 200 µm were fabricated using spin coating, membranes with a thickness of 500 µm were cast. All membranes were cured at 80 °C. Immediately be-

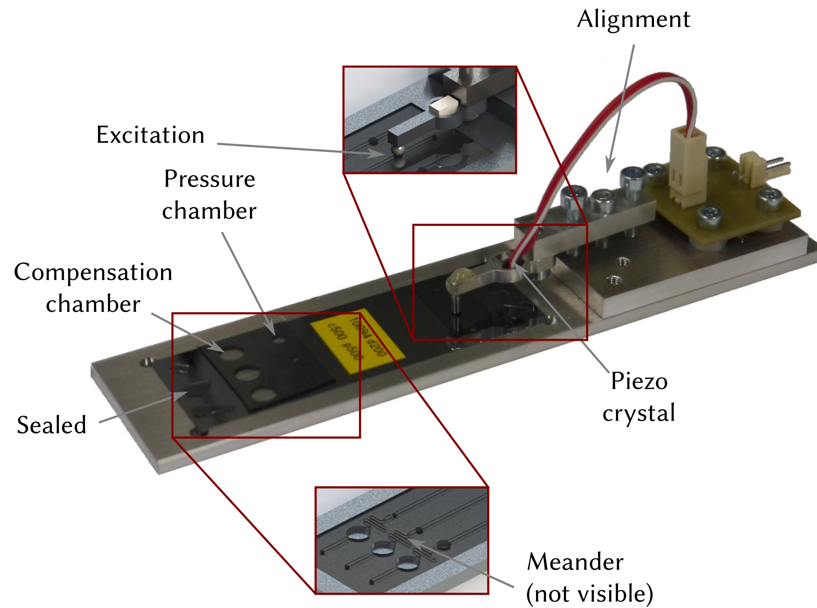

Figure 21: Test setup for the fluidic low-pass filter. Photography and CAD drawing (insets) of the completely assembled setup. The chip is placed in the fixture and the excitation membrane is deflected by a piezo actuator. Three screws are used to align the piezo actuator. On the photography, the PDMS membranes are visible. The meander structure is not visible on the photography because it is on the bottom side.

fore a membrane is attached to the silicon chip, both the membrane and the silicon surface are treated by a plasma. The plasma is generated by the discharge of a Tesla-type coil vacuum leak detector (Model BD-10ASV, Electro-Technic Products, USA). The plasma changes the surface chemistry and leads to a permanent bond of PDMS and silicon after the attachment [62, 63]. The PDMS membrane is applied to the Si-chip by hand using a tweezer. The PDMS immediately sticks to the silicon surface. As adjusting is impossible after the application, the membrane has to be slightly stretched to avoid a wavy surface. Table 4 shows the membrane radii and thicknesses and the depth of the channels for all tested systems.

3.4.2 Experimental setup

During the experiment the chip is placed in a holder (Figure 21). On the holder, a piezo actuator (A10E, elliptec, Germany) is mounted. The actuator moves a metal sphere up and down to deflect the membrane of the excitation chamber that is placed exactly below the sphere. The piezo crystal is driven by a sinusoidal voltage generated by a frequency generator and amplified by an external circuit. Frequencies between 0.01 Hz and 1 kHz with a peak-to-peak voltage of 20 V, corresponding to a deflection of about 4.6 μm, can be achieved [64]. The membrane deflection is measured using an atomic force microscope (MFP-3D, Asylum Research, USA) allowing for measurements in the sub-nanometre range. For each system, many different frequencies are applied (see below) and the membrane deflections of the pressure chamber and the compensation chamber are measured. A sine function is fitted to the data for each frequency to obtain the amplitude of the oscillation. For each fit, several hundred to thousand single measurements are evaluated. Combined with the resolution of the AFM, the error of the fitted amplitude is negligibly small. Other effects like vibrations of the experimental setup impose a much larger un-

						experimental		simulated	
n	b_2/µm	d_1/mm	d_3/mm	t_1/µm	t_3/µm	D_1/N m^{-1}	D_3/N m^{-1}	D_1/N m^{-1}	D_3/N m^{-1}
p1	50	1.7	3.0	500	50				
p2	50	1.0	5.0	500	500				
p3	50	1.7	3.0	500	500				
p4	50	3.0	1.0	500	500	not evaluated			
p5	50	3.0	5.0	500	500				
p6	200	1.0	5.0	500	500				
p7	200	3.0	5.0	500	500				
1	200	1.7	5.0	50	500	147	9200	57	2305
2	200	3.0	3.0	500	200	7284	674	4107	645
3	250	1.7	5.0	50	500	173	3132	57	2305
4	250	3.0	3.0	500	200	5019	578	4107	645
5	250	3.0	5.0	200	500	683	3987	645	2305

Table 4: Geometry, experimental and simulated spring constants. n is the sensor number, a “p” denotes a sensor from the pretest. b_2 is the depth of the channel. d_i, t_i, and D_i are the diameter, the thickness, and the spring constant, respectively, of the membrane of the pressure chamber ($i = 1$) and the compensation chamber ($i = 3$) (adapted from Siebke et al. [61]).

certainty on the measured amplitude. The quantification of such systematic effects would require further experiments and analyses that were not carried out here. Because the deflection of both chambers cannot be measured simultaneously, the spectrum is first recorded for the pressure chamber and then for the compensation chamber.

Using the setup described above, two test series were performed. The pretest was made to ensure the functioning of all components of the experiment. Furthermore, the results of the pretest were used to tune the parameters for the actual experimental validation of the fluidic low-pass filter.

3.4.3 Pretest

Using the formula for the cut-off frequency of the low-pass filter, Equation (73), suitable parameters for the pretest were chosen. The right choice of the membrane thickness and diameter and the channel depth ensures that the cut-off is in a frequency range which can measured using the experimental setup described above. However, this range could only be determined during the pretest. As it turned out, two factors limit the suitable range of measurements. At low frequencies, the measured signal is drifting strongly due to the long time needed for a single measurement. Below about 0.2 Hz, the drift is larger than the range of the AFM. No complete oscillation can be measured and the amplitude cannot be obtained. At frequencies above 200 Hz, the amplitude suddenly changes independently of the system's parameters. Most probably, the experimental setup itself starts to vibrate due to the excitation of the piezo actuator. Due to these limitations, only frequencies between 0.2 Hz and 200 Hz were used for further experiments.

Although this frequency range was unknown during the design of the pretest, the resulting frequencies spectra allow for a qualitative verification of the compensation mechanism. Figure 22 shows the measured data for pressure and compensation chamber for two frequencies (25 Hz and 0.25 Hz). When going from high to low frequencies, the amplitude of the pressure chamber is reduced, whereas the amplitude of the compensation chamber is increased. Figure 22(e) shows the amplitudes for both chambers for the complete frequency range. Below a certain position, the amplitude of the pressure chamber drops and

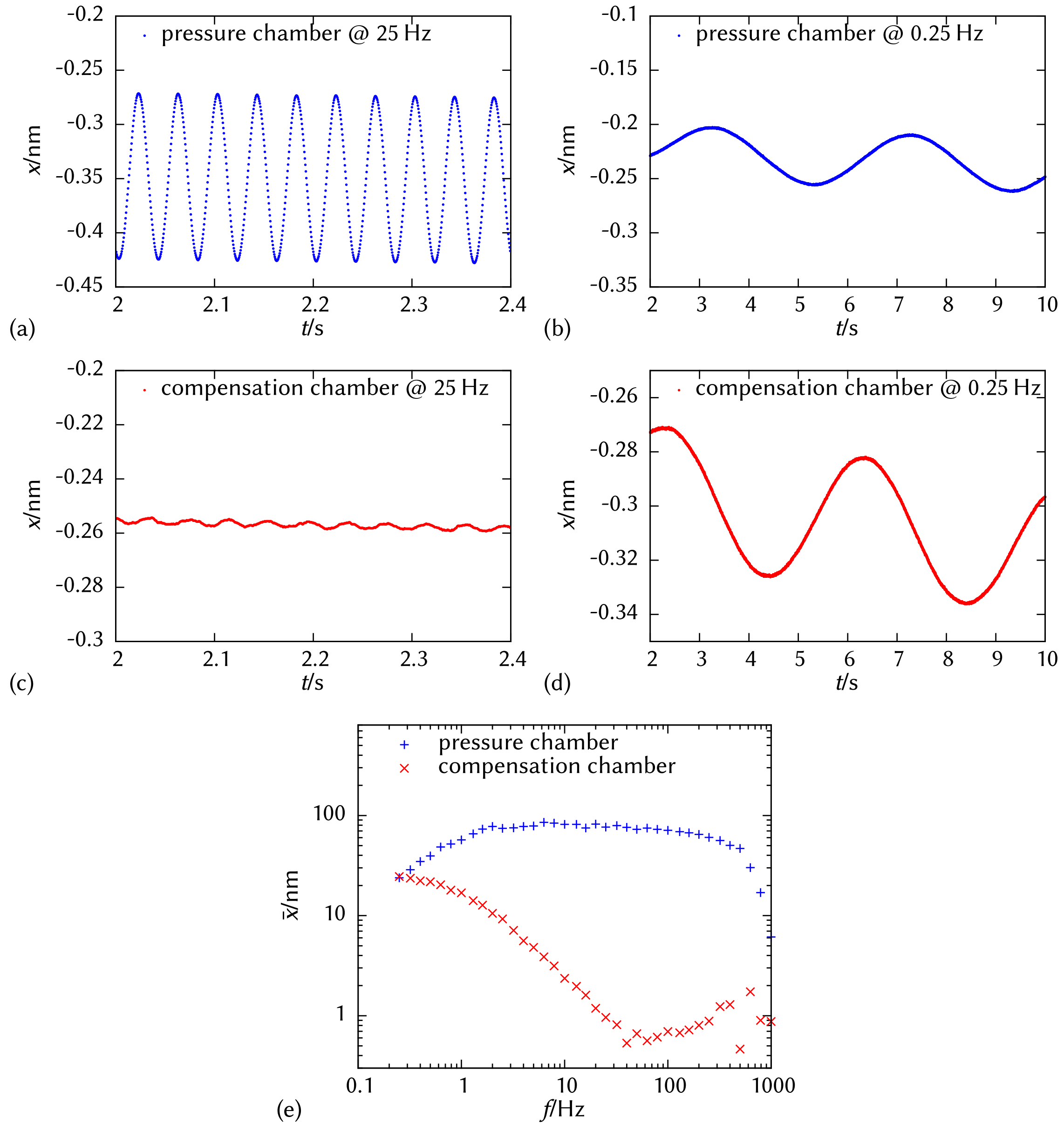

Figure 22: Pretest of the fluidic low-pass filter (Sensor p5). (a) – (d) Membrane deflection of the pressure and compensation for two different frequencies. (a) Pressure chamber at high frequency. (b) Pressure chamber at low frequency. (c) Compensation chamber at high frequency. (d) Pressure chamber at low frequency. (e) Amplitudes for one exemplary system of the pretest.

the amplitude of the compensation chamber rises towards smaller frequencies. So, this test proves that the compensation mechanism works as intended. However, at even smaller frequencies, it is expected that the amplitude of the pressure chamber stops dropping. Due to the limited frequency range, this point is not visible. Without this piece of information, the system is under-determined and it is impossible to fit the model equations to the experimental data of the pretest.

3.4.4 Calculation of the spring constants

Using the frequency range obtained during the pretest, suitable membrane and channel dimensions for the second experiment were obtained. Now the complete frequency region

of the compensation channel should be visible by the experimental setup. Table 4 shows the chosen parameters. The theoretical model presented in Section 3.1 predicts the deflection amplitude $\hat{x}_i$ of the membranes depending on the inflow $V_{\text{in},i}$ in both chambers (see Equation (26)):

$$\hat{x}_1 = \frac{\mathrm{i}\omega \hat{V}_{\text{in},1} + \gamma \frac{D_3}{A_3^2}\left(\hat{V}_{\text{in},1} + \hat{V}_{\text{in},3}\right)}{A_1 \mathrm{i}\omega + \gamma A_1 \left(\frac{D_1}{A_1^2} + \frac{D_3}{A_3^2}\right)}.$$

The value for $\hat{x}_3$ is obtained by exchanging the indices 1 and 3. In this case, only the pressure chamber has a direct inflow $\hat{V}_{\text{in},1} \neq 0$ through the excitation chamber, whereas the volume of the compensation chamber is only changed through the compensation channel. Therefore, $\hat{V}_{\text{in},3} = 0$. Furthermore, $\hat{x}_i$ is the mean deflection of the membranes, averaged across the membrane surface. However, the AFM does not measure the mean deflection of the membranes but rather the deflection at one point of the membrane, which is not necessarily at the centre. This can be compensated by introducing an additional scaling factor a_i to the equation above. Both $\hat{V}_{\text{in},1}$ and the scaling factor are combined to

$$V_i \equiv |\hat{V}_{\text{in},1}| a_i. \tag{78}$$

Finally, the measured amplitude $\bar{x}_i$ is the absolute value of $\hat{x}_i$:

$$\bar{x}_1 = |\hat{x}_1| = V_1 \left(\frac{[2\pi f]^2 + \left[\gamma \frac{D_3}{A_3^2}\right]^2}{[A_1 2\pi f]^2 + \left[\gamma A_1 \left(\frac{D_1}{A_1^2} + \frac{D_3}{A_3^2}\right)\right]^2} \right)^{1/2}, \tag{79}$$

$$\bar{x}_3 = |\hat{x}_3| = V_3 \left(\frac{\left[\gamma \frac{D_1}{A_1^2}\right]^2}{[A_3 2\pi f]^2 + \left[\gamma A_3 \left(\frac{D_1}{A_1^2} + \frac{D_3}{A_3^2}\right)\right]^2} \right)^{1/2}. \tag{80}$$

γ is the ratio of the volume flow through the compensation channel to the pressure difference. γ and A_i are defined by the known radii of the chambers as well as the cross section and length of the channel. However, the spring constants depend on many factors such as the material of the membranes. Therefore, the functions in Equations (79) and (80) are fitted to the data by adjusting D_1, D_3, and V_i. As described above, the systematic error of the amplitudes is unknown while the noise of the AFM is negligible. Instead, the same arbitrary relative error is assigned to each amplitude. By this, small deflections gain the same impact in the fitting procedure as large deflections. At the same time, an estimation of the errors of the spring constants is not possible. Figures 23(a) and 23(b) show the experimental data as well as the resulting functions for two different systems. Again, the frequency dependence of the deflections is as expected: For high frequencies, the membrane of the pressure chamber is deflected the most, whereas the membrane of the compensation chamber is only deflected very little. For low frequencies, the behaviour is reversed. The fluidic low-pass filter opens and large pressures in the pressure chamber are compensated. Instead, the membrane of the compensation chamber is deflected further. In contrast to the pretest, the complete frequency region of the compensation mechanism is measured here. The fitted functions reproduce this frequency dependence of the experimental data. Small deviations occur only on the shape of the transition from low to high frequencies and for the maximum amplitude. Most probably, these deviations are owed to the experiment.

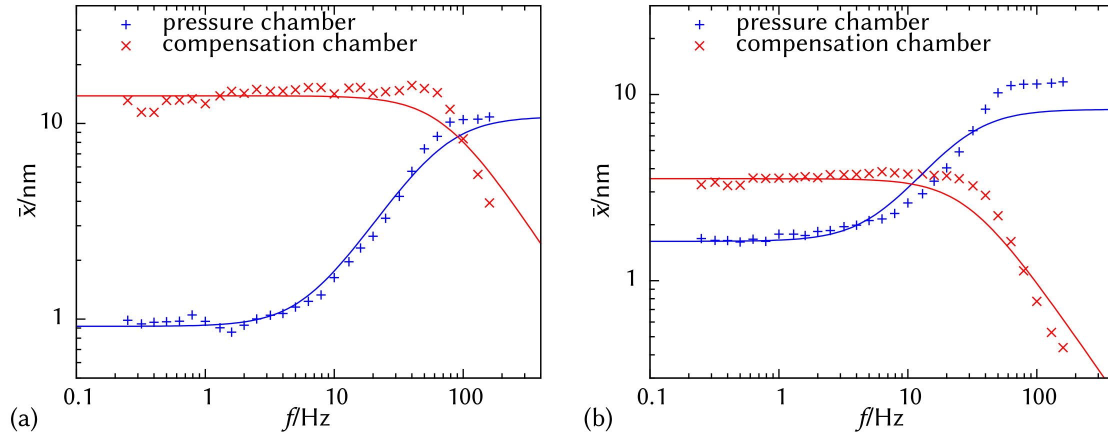

Figure 23: Experimental test of the fluidic low-pass filter. Measured amplitudes and fitted model for two exemplary systems. (a) Sensor 2; (b) Sensor 3 of Table 4.

For example, vibrations of the holder due to the piezo crystal will change the measured amplitude. The resulting spring constants for all systems are shown in Table 4.

As stated above, the prediction of the spring constants is not accurately possible. There are two factors largely influencing the spring constant, the Young's modulus of the PDMS and the stress of the membrane. An undefined stress is introduced to the membrane due to the fabrication (see Section 3.4.1). The Young's modulus depends on different parameters. In general it is defined by the choice of material. However, the Young's modulus strongly depends upon the manufacturing process. Varying the curing temperature between 25 °C and 200 °C, the mixing ratio between 1:5 and 1:15, and the thickness between 50 µm and 1800 µm changes the Young's modulus by more than a factor of two each [65–67]. Based on this, the Young's modulus of the used membranes is estimated by interpolation. Starting with a Young's modulus of about $E_{3000\,\mu\mathrm{m}} = 1.9\,\mathrm{MPa}$ interpolated from [65] for a curing temperature of 80 °C and a thickness of 3000 µm, the values for smaller thicknesses are derived using [67] (Table 5). With the Young's modulus at hand, it is possible to simulate the bending of the membranes using COMSOL Multiphysics in order to calculate the expected spring constants (see Section 3.3.1).

Figure 24 shows the averaged spring constants from the experiment (blue "+") and the estimated values (red "×"). Despite the uncertainties when estimating the spring constants, most of the experimental results match the calculated values within their spread. For the 500 µm thick membranes, the spread is the largest. For the other membrane sizes, all measured values are close to each other. Only for the thinnest membrane (50 µm), the simulated value deviates substantially from the measured value. Three factors are most probably responsible for these deviations. First of all, the thickness dependency in [67] probably was not measured for the used type of PDMS. Therefore, the actual values for the Young's modulus may differ from the values in Table 5. Second, the membrane is easily stretched upon applying on the Si-chip, thereby introducing a stress in the membrane and increasing the spring constant (see above). Most probably, this happens for thin and thus very elastic membranes. It is assumed that this is the reason for the measured value being higher than expected for the membrane with 50 µm thickness. The differing values for the very thick membranes can be caused additionally by an uneven thickness introduced during the casting process.

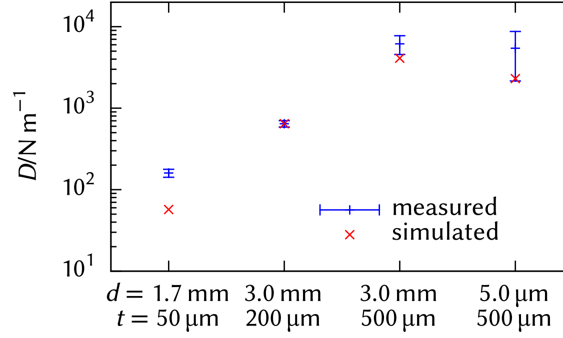

Figure 24: Comparison of measured and simulated spring constants. The measured values are the average of all values for the same membrane thickness and radius (from Siebke et al. [61]).

t/µm	E/MPa
3000	1.9
500	3.2
200	3.9
50	5.4

Table 5: Young's modulus of PDMS for different thicknesses (from Siebke et al. [61]).

3.5 Estimation of the beetle's sensitivity

In Section 2.1.2, the discrepancy between the different values of *Melanophila's* sensitivity in the literature was discussed. Different experiments and model calculations yielded between 4×10^{-5} W m^{-2} and 150 W m^{-2}. Based on an approach shown in [15], an estimation of the sensitivity based on the geometry and the material of the sensillum and known biological detection limits is presented here.[7]

Figure 25(a) shows a simplified sketch of the beetle sensillum, similar to the pressure chamber in the model description of Section 3.1.1. In this case, the compensation mechanism is omitted as it does not influence the maximum sensitivity. The sensillum is represented by a chamber with volume V. The dendrite is represented by a spring with spring constant D and surface area A. When the sensillum is illuminated, the radiant energy $\mathrm{d}Q_\mathrm{e}$ is partially stored as internal energy $\mathrm{d}U$ and partially converted to work $\mathrm{d}W$:

$$\mathrm{d}Q_\mathrm{e} = \mathrm{d}U + \mathrm{d}W\,. \tag{81}$$

The absorbed heat leads to an increase of the temperature $T = T_0 + \Delta T$:

$$\mathrm{d}U = C\,\mathrm{d}T \tag{82}$$

$$\Rightarrow \Delta U = C\Delta T = c\rho V_0 \Delta T\,, \tag{83}$$

where C is the heat capacity of the pressure chamber, c and ρ are the specific heat capacity and the density of the liquid, respectively. The deflection x of the membrane follows Hook's law:

$$\mathrm{d}W = F\,\mathrm{d}x = Dx\,\mathrm{d}x\,. \tag{84}$$

[7] Parts of this section were previously published in Siebke et al. [61].

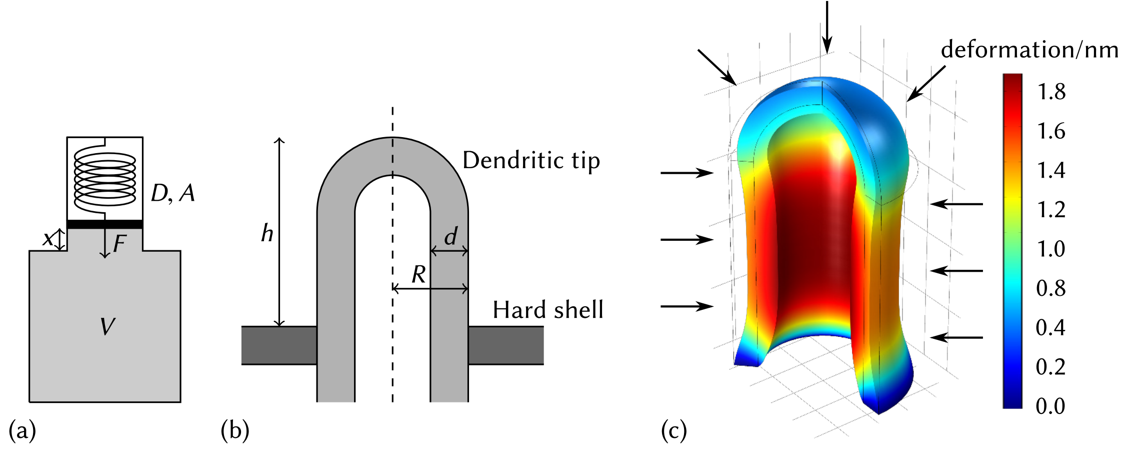

Figure 25: Simplified geometries for the estimation of the minimum required irradiance. (a) The sensillum is modelled as a chamber and a spring representing the dendrite. V is the volume of the sensillum, x is the deflection of the spring, F is the force applied by the spring, $D = 0.025\,\mathrm{N\,m^{-1}}$ and $A = 1.42\,\mathrm{\mu m^2}$ are the spring constant and the surface area of the dendrite, respectively. (b) The dendrite is represented by a cylinder with a spherical cap. Height $h = 0.9\,\mathrm{\mu m}$, radius $R = 0.25\,\mathrm{\mu m}$ [5]. The thickness of the wall is $d = 68\,\mathrm{nm}$ [68]. Not to scale. (c) COMSOL Multiphysics simulation of the deformed dendrite. The dendrite surface is exposed to a pressure indicated by the arrows. The pictured deformation is scaled to be visible (from Siebke et al. [61]).

Thermal expansion is described by

$$\Delta V = \alpha V_0 \Delta T \tag{85}$$

$$x = \frac{\Delta V}{A} = \frac{\alpha V_0}{A}\Delta T, \tag{86}$$

α being the coefficient of linear thermal expansion. Inserting into Equation (84) yields

$$\mathrm{d}W = D\frac{\alpha V_0}{A}\Delta T\frac{\alpha V_0}{A}\,\mathrm{d}T \tag{87}$$

Now, the integration from T_0 to T results in

$$W = \tfrac{1}{2}D\left(\frac{\alpha V_0}{A}\right)^2 \Delta T^2. \tag{88}$$

By using Equation (83), the following relation is obtained:

$$W = \tfrac{1}{2}D\left(\frac{\alpha V_0}{A}\right)^2\left(\frac{\Delta U}{c\rho V^0}\right)^2 = \tfrac{1}{2}D\left(\frac{\alpha \Delta U}{c\rho A}\right)^2 \tag{89}$$

$$\Rightarrow \Delta U = \sqrt{\frac{2}{D}}\frac{c\rho A}{\alpha}\sqrt{W} \tag{90}$$

$$\Rightarrow Q_\mathrm{e} = \sqrt{\frac{2}{D}}\frac{c\rho A}{\alpha}\sqrt{W} + W. \tag{91}$$

Depending on the minimum deformation energy W and the spring constant D of the dendrite, it is possible to calculate the amount of heat Q_e that has to be absorbed by the sensillum. This minimum deformation energy is unknown for *Melanophila*. However, as the IR receptors are derived from hair mechanoreceptors (see Section 2.1), it is reasonable to

		water @ 20 ℃ [72]	silicone oil AK 250 [73]
Coefficient of volumetric expansion	$\alpha/10^{-3}\,\mathrm{K}^{-1}$	0.21	0.93
Specific heat capacity	$c/\mathrm{kJ\,kg^{-1}\,K^{-1}}$	4.18	1.55
Density	$\rho/10^{3}\,\mathrm{kg\,m^{-3}}$	1.00	0.97
Minimum required irradiance	$E_{\mathrm{min}}/\mathrm{W\,m^{-2}}$	24.98	2.03

Table 6: Physical properties of water and silicone oil and the minimum radiation intensity of the sensillum (from Siebke et al. [61]).

assume that it is comparable to other highly sensitive hair mechanoreceptors found in nature. Measurements of the minimum deformation energy were e.g. conducted using the cricket *Acheta domestica*. Their hair mechanoreceptors can sense a deformation of 0.1 nm, corresponding to a deformation energy of 10^{-21} J [69].

Furthermore, the spring constant of the dendrite has to be determined carefully. This spring constant is an important property of the sensillum, strongly influencing the sensitivity. A similar approach as described in Section 3.3.1 is used to estimate the spring constant. The shape of the tip of the dendrite inside the pressure chamber is approximated as shown in Figure 25(b). Membrane thickness d and height h are taken from [5]. If the tip of the dendrite is compressed, its cytoskeleton as well as the plasma membrane are deformed (light grey structure in Figure 25(b)). The Young's modulus of the dendrite was set to $E = 6.2\,\mathrm{kPa}$, taken from [70] . The influence of the liquid inside the tip can be neglected as the volume of the tip is small compared to the complete dendrite. When the tip is compressed, the liquid is displaced into the remaining volume. The dendrite as shown in Figure 25(b) is simulated, yielding a spring constant of $D = 0.025\,\mathrm{N\,m^{-1}}$ (Figure 25(c)). Unfortunately, the precise properties of the liquid inside the sensillum, like its density and specific heat capacity, are still unknown. Therefore, water and silicone oil are used to estimate the sensitivity. Water serves to estimate the minimum sensitivity. It has a large specific heat capacity as well as a low coefficient of thermal expansion. However, most probably, the liquid inside the sensillum is optimized to reach a higher sensitivity. As an estimation for an optimized liquid, silicone oil is used, which could also be used for the biomimetic sensor [71]. The relevant properties of both liquids are shown in Table 6.

For the minimum required deformation energy of $W = 10^{-21}\,\mathrm{J}$, a response time of $\Delta t = 4\,\mathrm{ms}$, a surface of the sensillum of $A_{\mathrm{sensillum}} = 80\,\mu\mathrm{m}^2$ [15], a minimum required intensity of about $25\,\mathrm{W\,m^{-2}}$ for water and about $2\,\mathrm{W\,m^{-2}}$ for silicone oil is obtained using Equation (91). The former value is very close to the value measured for single receptors in electrophysiological experiments of down to $50\,\mathrm{W\,m^{-2}}$ (see above, [19]). This is a strong hint that this calculation actually describes the sensitivity of the beetle's organ. Furthermore, the liquid inside the sensillum is probably similar to water, e.g. hemolymph (equivalent of blood in insects). A fundamentally different liquid, e.g. silicone oil, leads to a very different result. The development of a technological sensor based on the IR receptors of *Melanophila* as presented in the next section will help to verify this calculation and to end the decade long discussion about the sensitivity of the beetle.

4 From the sensor concept to a technological sensor

With the sensor concept and the model description at hand, it is now possible to design a biomimetic sensor inspired by the detection principle of *Melanophila*. The first thing to be known to accomplish this transition is the targeted size of the sensor. In general, smaller sensors are preferred over larger sensor. Smaller sensors are more versatile as they can be employed when limited space is available. Arrays of small sensors can be used to build imaging devices (*focal plane arrays*, FPAs). Furthermore, smaller devices usually are cheaper as less material is needed for production. However, the sensitivity must not suffer from the smaller scale of the sensor. Yet, in general, small devices are even preferred due to their enlarged sensitivity compared to large scale devices [46]. To estimate the influence of the size on the sensitivity of the biomimetic sensor, the dependence of the deflection x on the geometrical dimensions can be analyzed. Using Equations (30), (31), (47), (48), (65), and (68), the membrane deflection at low and high frequencies can be derived:

$$x(\omega \to 0) \propto l, \tag{92}$$

$$x(\omega \to \infty) = \text{const}, \tag{93}$$

where l is the length scale of the sensor. For very low frequencies, the deflection increases linearly with the length, whereas at high frequencies, it is independent of the size. However, the linear scaling is only valid when the sensor is at equilibrium with the environment. The transition frequency to the equilibrium state itself is proportional to $1/l$. Therefore, larger sensors could only be more sensitive if the modulation frequency is very small and the response time is very large. A large sensor using the photomechanic detection principle without the compensation mechanism is presented in [71].

For the reasons stated above, the sensor design presented in this work aims to provide a small sensor with a length scale of a few millimetres. To incorporate the mechanical, fluidic, and electrical sensor parts into a single device, the sensor is fabricated using micro systems technology. Therefore, the sensor is referred to as µ-biomimetic. In the following sections, the sensor design as well as the technological fabrication steps are presented.

4.1 Design of the micro technological sensor

Figure 26 shows the transfer from the beetle's receptor to the design of a micro technological sensor. The overall area of the sensor is 4 mm × 4 mm, the height is about 2 mm. The micro technological sensor consists of a pressure chamber and a compensation chamber that are interconnected by a long and narrow channel. These structures are formed by two silicon wafers. Instead of the dendrite, a silicon nitride membrane is located at the top of the pressure chamber. When a fluid inside the pressure chamber expands due to the

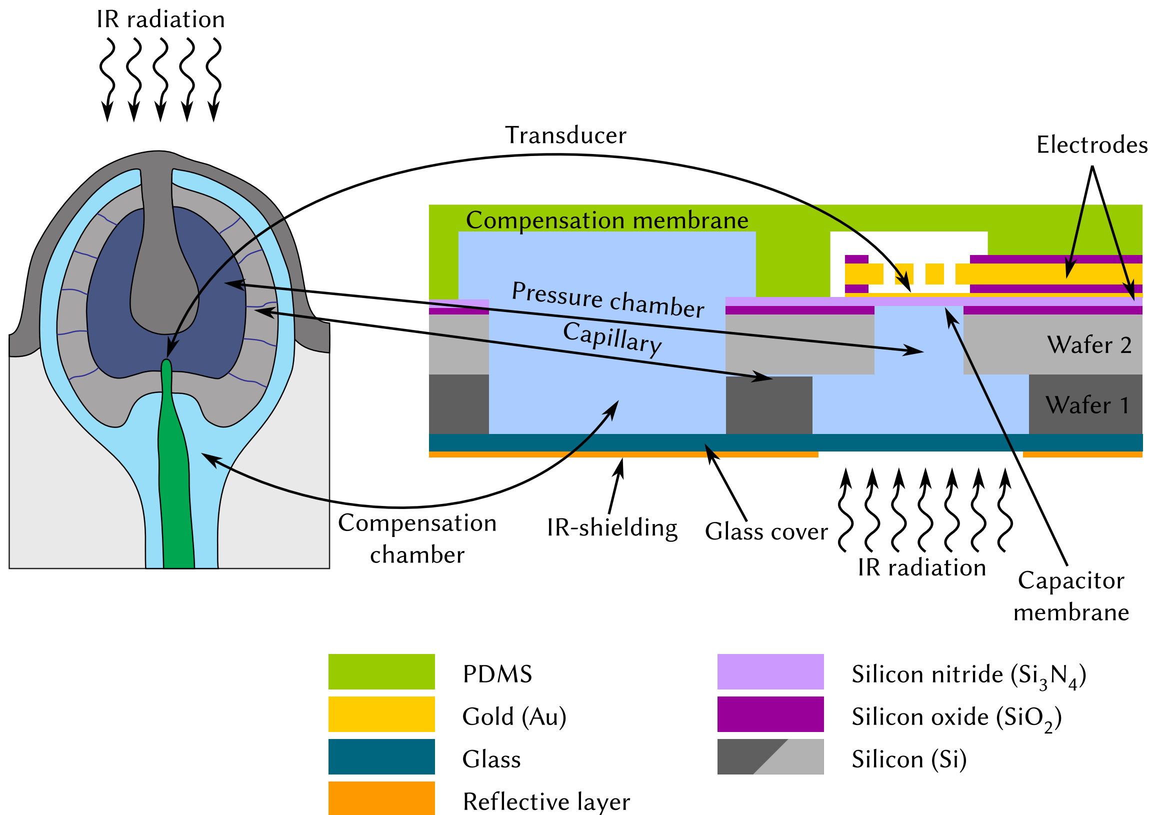

Figure 26: Transfer of the biological sensor to the technological sensor. Left: Simplified cross-section of the beetle's sensillum. Right: Cross-section of the technological IR-sensor. Not to scale (adapted from Siebke et al. [11]).

absorption of IR radiation, the membrane is deflected. The deflection of the membrane is detected capacitively. The Si_3N_4 membrane is coated with gold, thereby forming one electrode of a plate capacitor. The other, rigid, electrode is located above the membrane. By continuously measuring the change in capacitance, the deflection of the membrane and the absorbed heat can be inferred. As will be explained in Section 5.1, the electronics used to measure the capacitance is able to detect changes below 0.1 fF at a frequency of 1 Hz. Due to the large ratio between the diameter of the membrane and the electrode distance of 1000, deflections of about 0.1 nm can be detected (see Section 7.2). The compensation mechanism is implemented by the compensation chamber and the compensation channel. The compensation chamber is larger than the pressure chamber and is sealed by a thin and flexible PDMS membrane. In this way, the pressure inside the compensation chamber only changes very little if the volume increases. This design is equivalent to that in the beetle, where many nano-channels connect the pressure chamber to the outer compartment.

4.2 Parameter optimization

For the fabrication of the micro technological sensor, a compromise between the size and the feasibility has to be made. First the primary technological goal is to provide the proof of principle based on the design of Figure 26 and the model calculations (see Section 3.1). For the proof of principle, the design is optimized to facilitate the fabrication process. In a future work, the overall sensor design can be adapted to achieve a sensitivity as high as possible. Nevertheless, the response of the sensor is maximized here within the given

Parameter	Value
Overall sensor area	$4 \times 4\,\mathrm{mm}^2$
Overall sensor thickness	approx. 2 mm
Height of Si/glass wafers	300 µm
Lower diameter of the pressure chamber	1000 µm
Upper diameter of the pressure chamber	500 µm
Diameter of the compensation chamber	1000 µm
Diameter of the upper electrode	480 µm
Diameter of the lower electrode	540 µm
Distance between the electrodes	500 nm
Thickness of the upper electrode	5 µm
Thickness of the lower electrode	200 nm
Thickness of the Si_3N_4 membrane	700 nm
Thickness of the PDMS cover	approx. 1 mm

Table 7: Dimensions of the sensor used for the model calculations.

Fluidic model		Thermal model, environment, and expansion	
Parameter	Value	Parameter	Value
A_1	$1.96 \times 10^{-7}\,\mathrm{m}^2$	C_1	$2.22\,\mathrm{mJ\,K}^{-1}$
A_3	$7.85 \times 10^{-7}\,\mathrm{m}^2$	C_3	$17.2\,\mathrm{mJ\,K}^{-1}$
D_1	$12\,000\,\mathrm{N\,m}^{-1}$	σ'	$19.2\,\mu\mathrm{W\,K}^{-1}$
D_3	$150\,\mathrm{N\,m}^{-1}$	λ'	$162\,\mathrm{mW\,K}^{-1}$
l_2	16.0 mm	α'_1	$1.09 \times 10^{-13}\,\mathrm{m}^3\,\mathrm{K}^{-1}$
c_2	3.00 µm	α'_3	$1.94 \times 10^{-13}\,\mathrm{m}^3\,\mathrm{K}^{-1}$
d_2	10.00 µm		
η	1.00 mPa s		

Table 8: Parameters used for the calculations of the frequency spectra.

geometrical limits. All dimensions used here including the optimized parameters can be found in Tables 7 and 8.

4.2.1 Requirements regarding the sensor

As stated in Section 3.1, the sensitivity strongly depends upon the chopping frequency. The electronics setup is best suitable for chopping frequencies up to 1 Hz, while lower frequencies in general result in a higher sensitivity. Therefore frequencies in the range $f = 0.1\,\mathrm{Hz}$ to $1\,\mathrm{Hz}$ are chosen for the maximization of the sensitivity. At smaller frequencies, the compensation mechanism should reduce the deflection to protect the sensor.

To reliably detect a signal, a minimum deflection of the membrane of at least $\hat{x}_1 \geq 0.1\,\mathrm{nm}$ is demanded. When the mean deflection is too large, $\hat{x}_1 \gtrsim 100\,\mathrm{nm}$, the membrane touches the upper electrode and the capacitor can be damaged. The largest change in temperature of the sensor is due to changing temperatures between day and night. To estimate the deflection due to this transition, a temperature amplitude of $\hat{T}_{\mathrm{out}} = 10\,\mathrm{K}$ is chosen, cor-

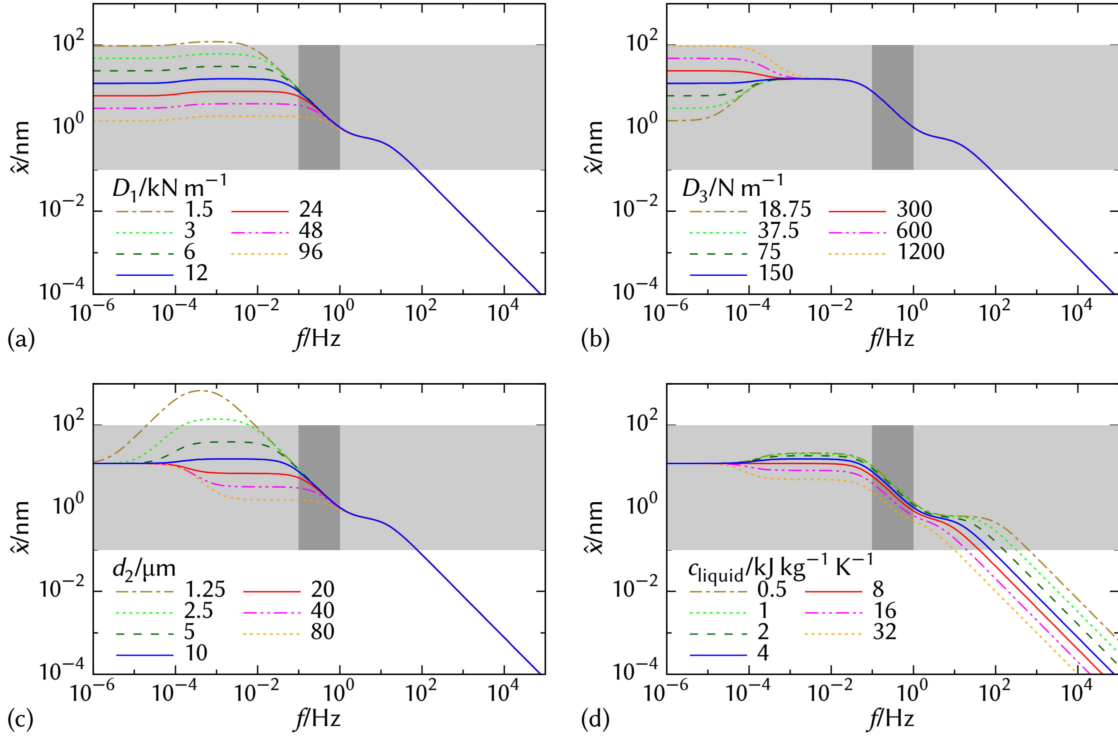

Figure 27: Influence of different parameters on the frequency spectrum of the deflection of the capacitor membrane for $\hat{T}_{out} = 10\,\mathrm{K}$ or $\hat{\Phi}_{src} = 19.2\,\mu\mathrm{W}$. The solid line denotes the parameter set used for our sensor. The grey band denotes the detectable deflections; larger deflections damage the sensor. The dark grey area marks the anticipated frequency interval. (a) Variation of capacitor membrane stiffness. (b) Variation of compensation membrane stiffness. (c) Variation of compensation channel depth. (d) Variation of liquid heat capacity.

responding to a difference between minimum and maximum temperature of 20 K. Hence, at temperature amplitudes smaller than 10 K, the deflection amplitude must not exceed 100 nm.

4.2.2 Implications of the model

Four parameters are used to optimize the sensitivity based on the overall geometry of the µ-biomimetic sensor. These are the spring constants of the membranes, the depth of the compensation channel, and the specific heat capacity of the liquid. All of these can be altered without introducing large changes to the fabrication process, e.g. the requirement of new masks for the photolithography. The graphs in this section are computed for $\hat{T}_{out} = 10\,\mathrm{K}$ as explained is Section 3.2. By varying one of the above parameters, the deflection $\hat{x}_1$ should be maximized in frequency range of 0.1 Hz to 1 Hz, unless it exceeds the maximum deflection of 100 nm at any frequency.

The first parameters that are determined are spring constants D_i of the membranes. Figures 27(a) and 27(b) show the deflection amplitude for different values of the spring constant D_1 and D_3, respectively. In both cases, an increase of D_i leads to a shift of the cut-off frequency to higher frequencies, described by Equation (73), containing the sum of D_1/A_1^2 and D_3/A_3^2. This is different for the damping. Making the capacitor membrane stiffer or the compensation membrane more flexible leads to an increased damping for low frequencies. This is reflected by Equation (74). Here, the characterising term is the quo-

tient of D_1/A_1^2 and D_3/A_3^2. To maximize the damping for low frequencies, the compensation membrane should be as flexible as possible, while the capacitor membrane should be sufficiently stiff. If the capacitor membrane is too hard, its influence on the cut-off frequency becomes too large. By using PDMS with a thickness of $d_3 = 50\,\mu\text{m}$, a spring constant as low as $D_3 = 150\,\text{N}\,\text{m}^{-1}$ can be achieved (see Section 3.4.4). As will be proven in Section 7.2, a Si_3N_4 membrane with a radius of $R_1 = 250\,\mu\text{m}$ and thickness of $d_1 = 0.5\,\mu\text{m}$ can achieve a spring constant of about $12\,000\,\text{N}\,\text{m}^{-1}$. With these values, the requirements mentioned above are met.

The third parameter that can be easily adjusted during the manufacturing process is the depth d_2 of the compensation channel (Figure 27(c)). It is verified by Equations (73) and (74) that the depth as well as the other dimensions of the channel, width and length, only influence the position of the cut-off, but not the damping factor. The geometry of the channel solely influences the γ-factor. Therefore, any change of one of these parameters is equivalent to a change of one of the other parameters. In this case, the depth d_2 is used to shift the cut-off frequency just below the measuring range. By using a depth of $d_2 = 10\,\mu\text{m}$, the actual measurement is not disturbed, but lower frequencies are damped.

The fourth parameter is the specific heat capacity c_{liquid} of the liquid inside the sensor (Figure 27(c)). A smaller heat capacity leads to a larger increase of the temperatures inside the sensor. When the frequency is sufficiently large ($\gtrsim 10\,\text{Hz}$), no heat is transferred from the capacitor to the compensation chamber. In this frequency range, the effect of a decreased heat capacity is the largest. For lower frequencies, the heat is distributed across the sensor. As the heat capacity of the silicon chip is fixed ($C_{\text{chip}} = 14.2\,\text{mJ}\,\text{K}^{-1}$), the total heat capacity of the sensor is only reduced by a small fraction when decreasing the heat capacity of the liquid. Hence the effect of changing the heat capacity for these frequencies is smaller. Finally, for low frequencies, the sensor is at thermal equilibrium with the environment, and the heat capacity has no influence at all. Using other liquids than water has almost no influence on the sensitivity in the measuring range. Therefore, water will be used to fill the sensor as this is technologically easy to handle.

Finally the sensitivity of the sensor is calculated using the parameters defined above. For the faster chopping, $f = 1\,\text{Hz}$, a detection threshold of $\hat{\Phi}_{\text{src, min}} = 18 \times 10^{-6}\,\text{W}$, $\hat{E}_{\text{src, min}} = 5.9\,\text{W}\,\text{m}^{-2}$ is obtained. By decreasing the frequency down to $f = 0.1\,\text{Hz}$, the threshold is decreased to $\hat{\Phi}_{\text{src, min}} = 2.5 \times 10^{-6}\,\text{W}$, $\hat{E}_{\text{src, min}} = 0.80\,\text{W}\,\text{m}^{-2}$. For the transition between day and night, $f_{\text{d}} = 1.2 \times 10^{-5}\,\text{Hz}$, the threshold is reduced to $\hat{\Phi}_{\text{src, min}} = 1.6 \times 10^{-6}\,\text{W}$, $\hat{E}_{\text{src, min}} = 0.51\,\text{W}\,\text{m}^{-2}$. This is equivalent to a temperature amplitude of $\hat{T}_{\text{out,min}} = 0.08\,\text{K}$. The maximum temperature difference which the sensor can withstand at this frequency is twice the amplitude $\hat{T}$ needed for the maximum deflection $\hat{x}_{\text{max}} = 100\,\text{nm}$. Therefore, the sensor is able to compensate a temperature difference of

$$\Delta T_{\text{max}} = 2\hat{T}_{\text{out,min}} \frac{\Delta x_{\text{max}}}{\Delta x_{\text{min}}} = 160\,\text{K}. \tag{94}$$

When the sensor is assembled at a temperature of $T_0 = 300\,\text{K}$, it can be operated in a broad range between about $T_{\text{min}} = 250\,\text{K}$ and $T_{\text{max}} = 350\,\text{K}$.

4.3 Process flow

In this section, the process flow of the biomimetic sensor is presented (Figures 28 to 34). As the complete process consists of more than 50 individual steps, only the most relevant steps are shown here. Multiple deposition steps are subsumed, photolithography and

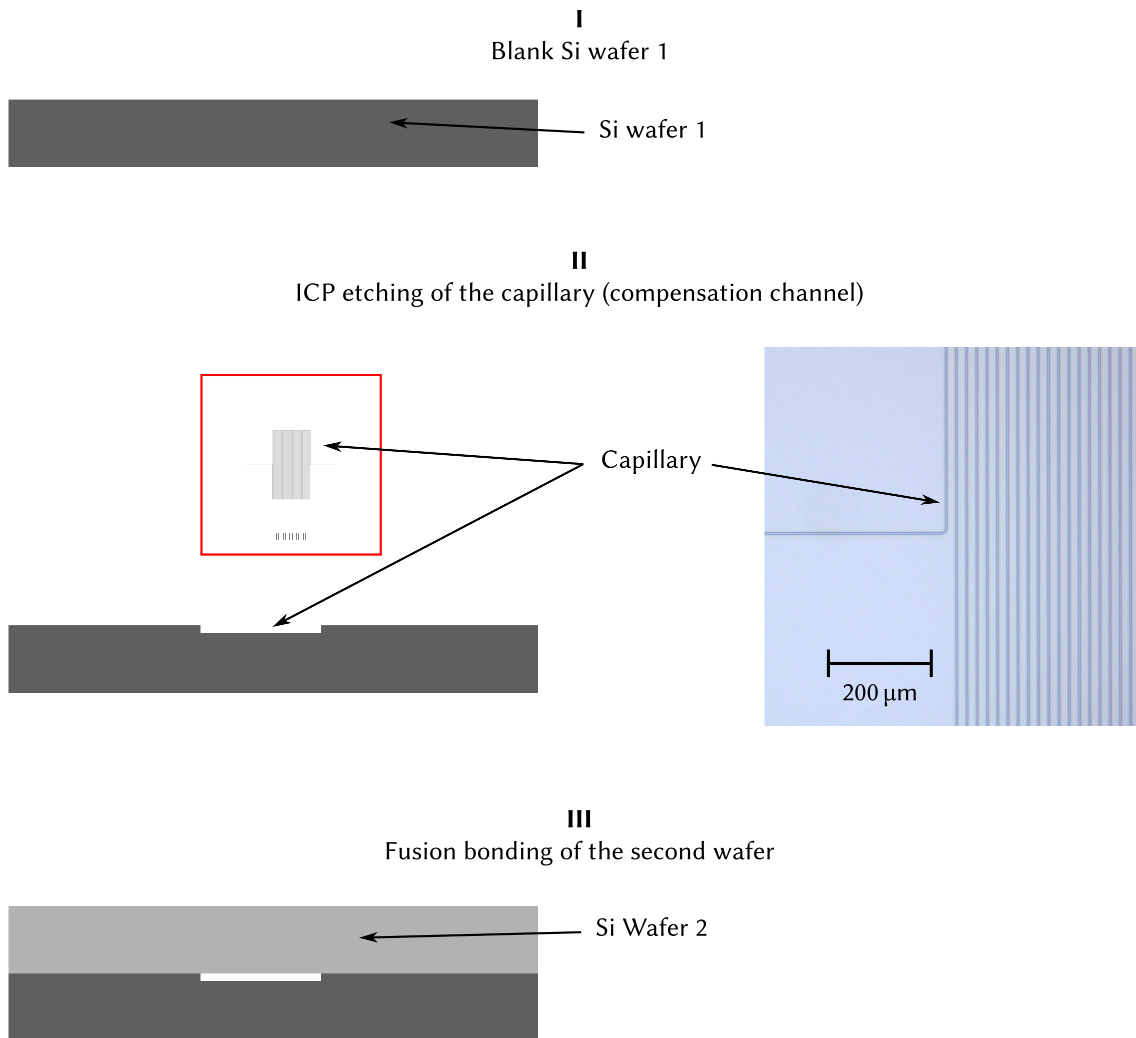

Figure 28: Steps I – III of the micro-technological process flow of the µ-biomimetic sensor. Not to scale. The red square shows a detail of the photolithography mask corresponding to a single sensor.

resist stripping are neglected in this description. Instead, the photolithography mask corresponding to a single sensor is shown for structuring steps. For a detailed description of the individual deposition, etching, and photolithography steps, see Section 2.3. Here, only the most basic process to fabricate the micro capacitor is shown. In Section 7.1, optimized and more complex processes with a higher yield are presented. After the micro technological processing steps, the sensor has to be filled bubble-free with water and sealed. This is explained in the next section. The complete process sequence is described in Appendix A.

The process starts with a blank silicon wafer (I). In the first step, alignment marks are etched on the bottom side of this wafer (not shown). This step is necessary to ensure the correct alignment of the capillary, which will be buried between two wafers, with respect to all other structures. In the next step, the capillary is etched into the top of the wafer (II) using an ICP process. Afterwards a second wafer is bonded on top of the first wafer by means of fusion bonding (III). Without the alignment marks on the bottom, it would be impossible to align further structures relative to the capillary. By thermal oxidation, a SiO_2 layer is created on both sides of the wafer. On the top side, it will be used as an etch stop during Si etching, on the bottom side it serves as a hard mask (see below). A layer of Si_3N_4 is deposited on both sides on the wafer using an LPCVD process. This layer

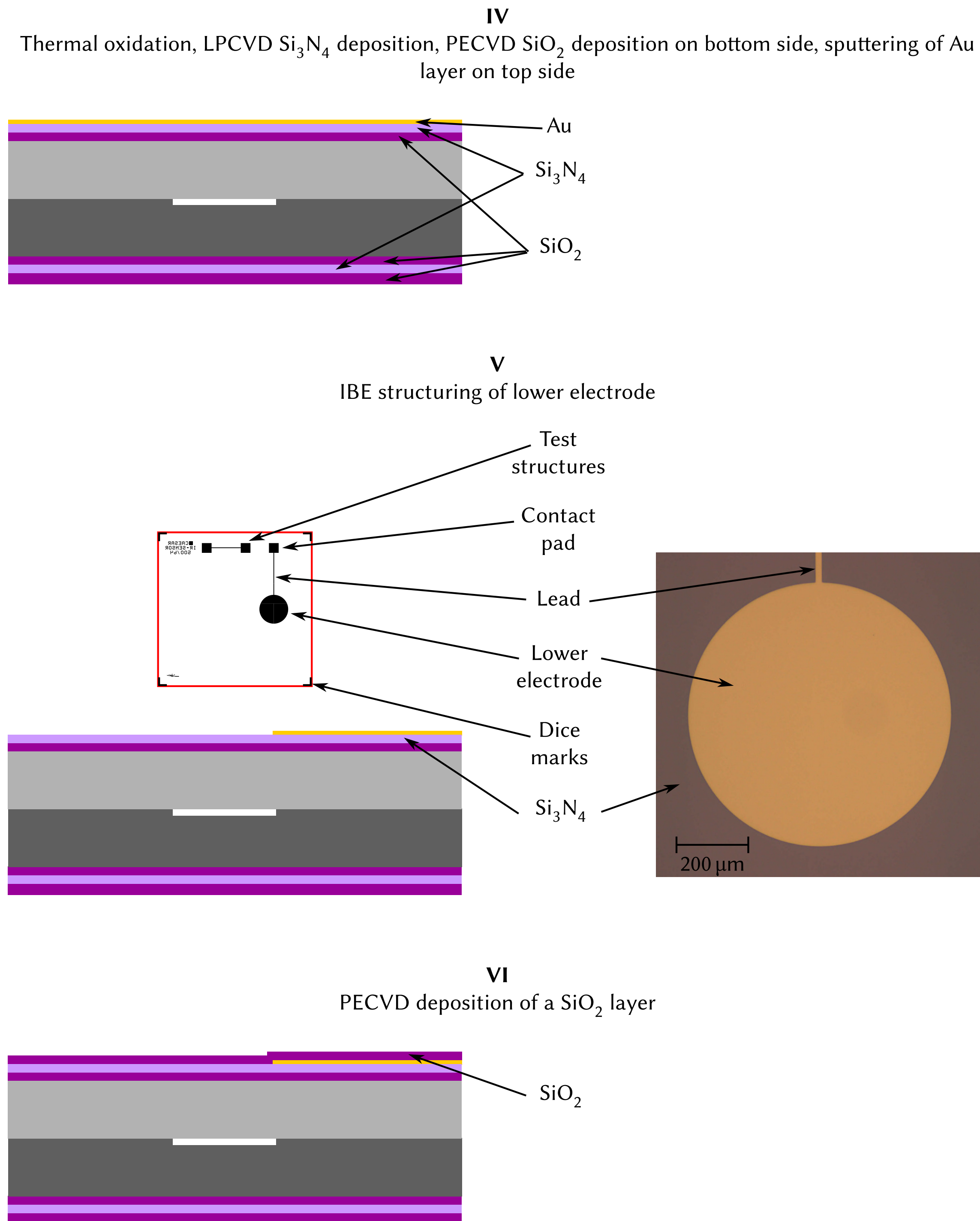

Figure 29: Steps IV – VI of the micro-technological process flow of the µ-biomimetic sensor. Not to scale. The red square shows a detail of the photolithography mask corresponding to a single sensor.

is used as a membrane of the pressure chamber and as a hard mask. On the bottom side, an additional PECVD SiO_2 layer is deposited to further reinforce the hard mask. On the top side, a layer of gold is sputtered (IV). This layer is structured using an IBE process to form the lower electrode including lead and contact pad as well as dicing marks and test structures (V). A layer of PECVD SiO_2 is deposited on the top side (VI) and is etched using RIE at the contact pads and the position of the compensation membrane (VII). At the latter position, also the underlying Si_3N_4 and SiO_2 layers are etched using RIE (VIII).

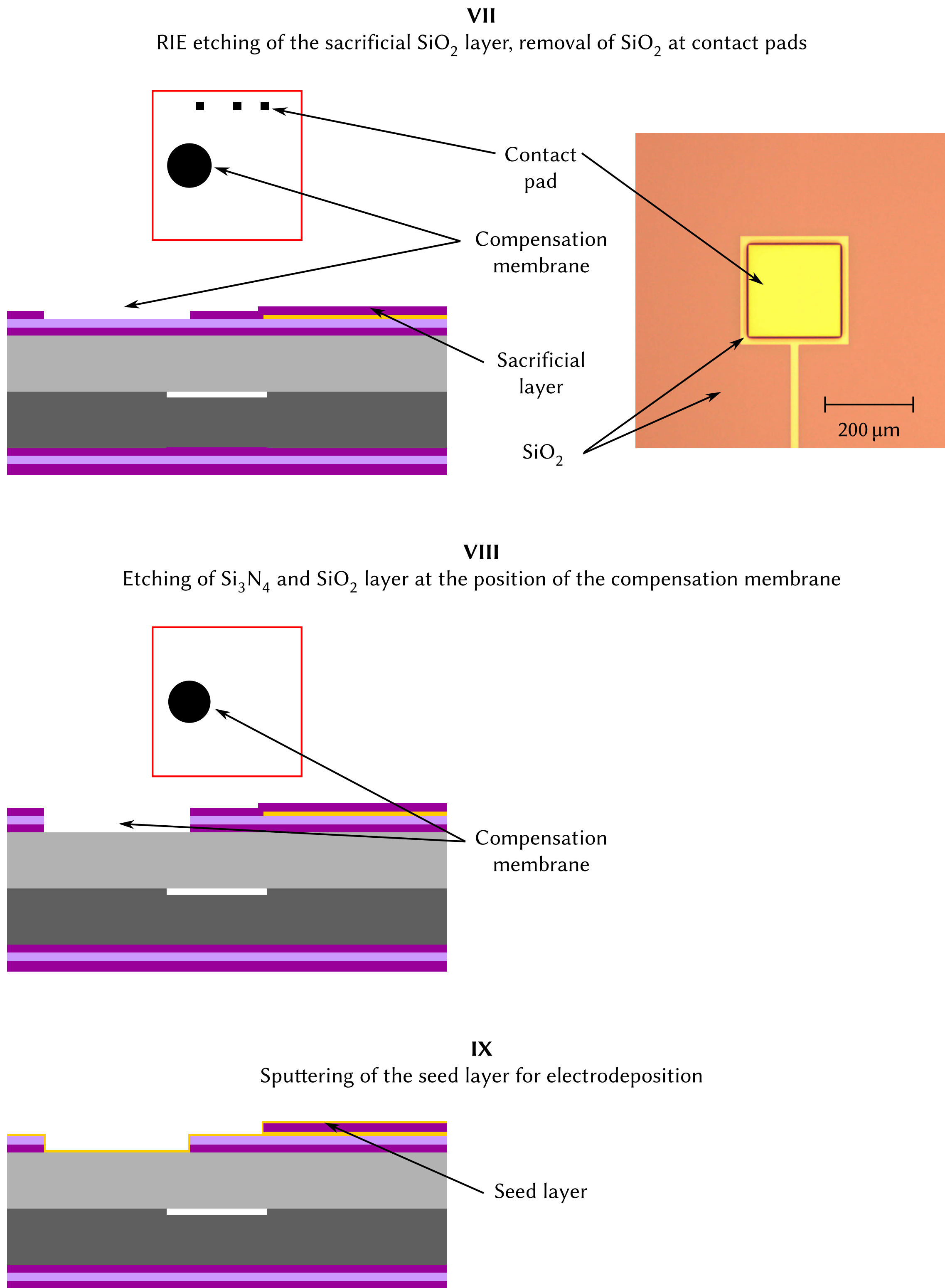

Figure 30: Steps VII – IX of the micro-technological process flow of the µ-biomimetic sensor. Not to scale. The red squares show a detail of the photolithography mask corresponding to a single sensor.

To fabricate the upper electrode, first an Au seed layer is sputtered on top of the wafer. Sputtering instead of vapour deposition is crucial in this step to create a continuous layer that is not interrupted at edges (see also Section 2.3.2.2). On top of the seed layer, a thick resist (AZ9260, ~ 10 µm) is spun on and structured (X). During the electroplating process,

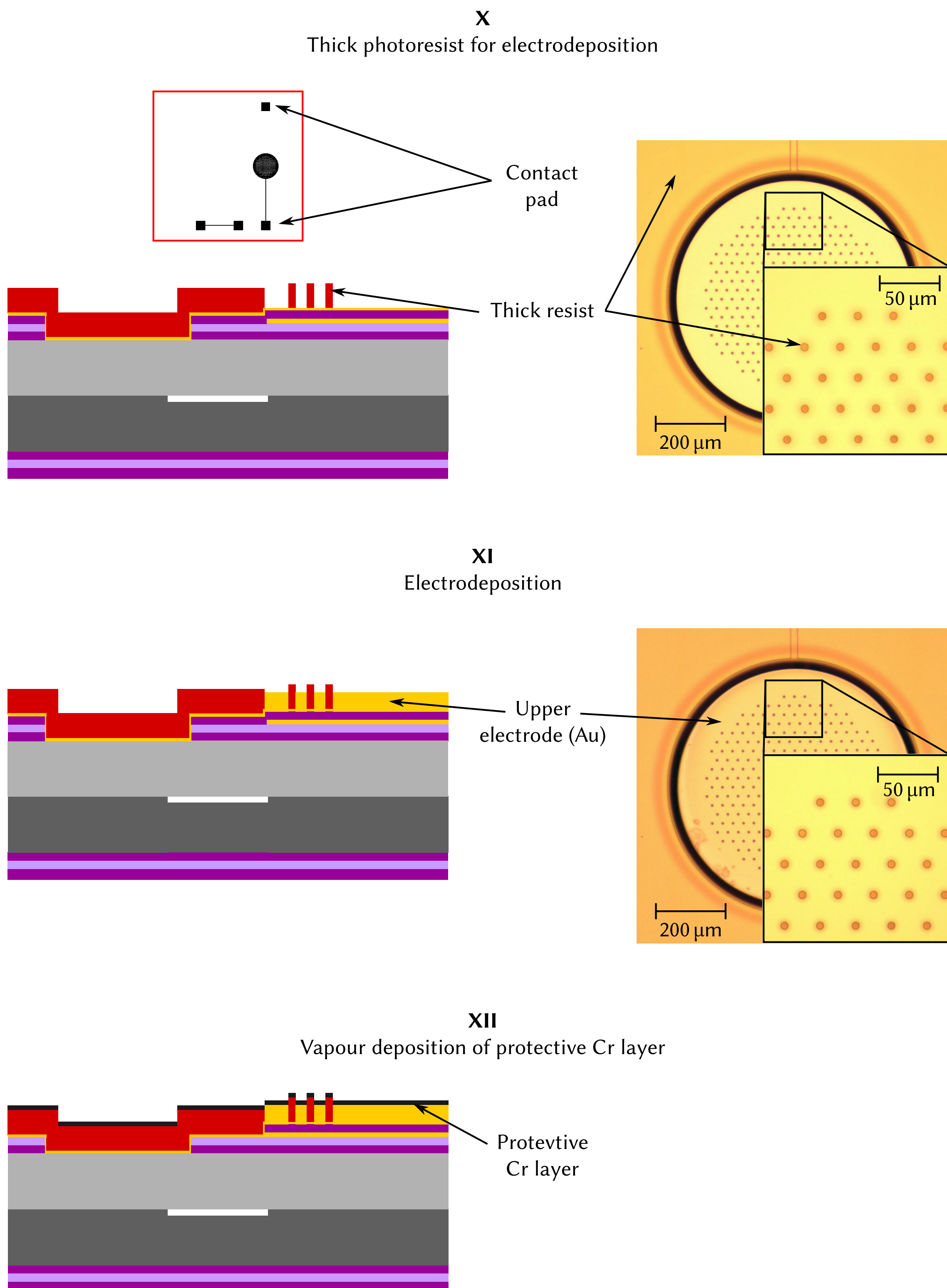

Figure 31: Steps X – XII of the micro-technological process flow of the µ-biomimetic sensor. Not to scale. The red square shows a detail of the photolithography mask corresponding to a single sensor.

gold is deposited at all metal surfaces that are immersed in the electrolyte (XI). Due to the continuous seed layer, the wafer only needs to be contacted at the outermost edge. Prior to the stripping of the resist, a layer of chrome is vapour deposited on the top side. Due to the vapour deposition, edges of the resists are not covered (XII). This allows for a lift-off

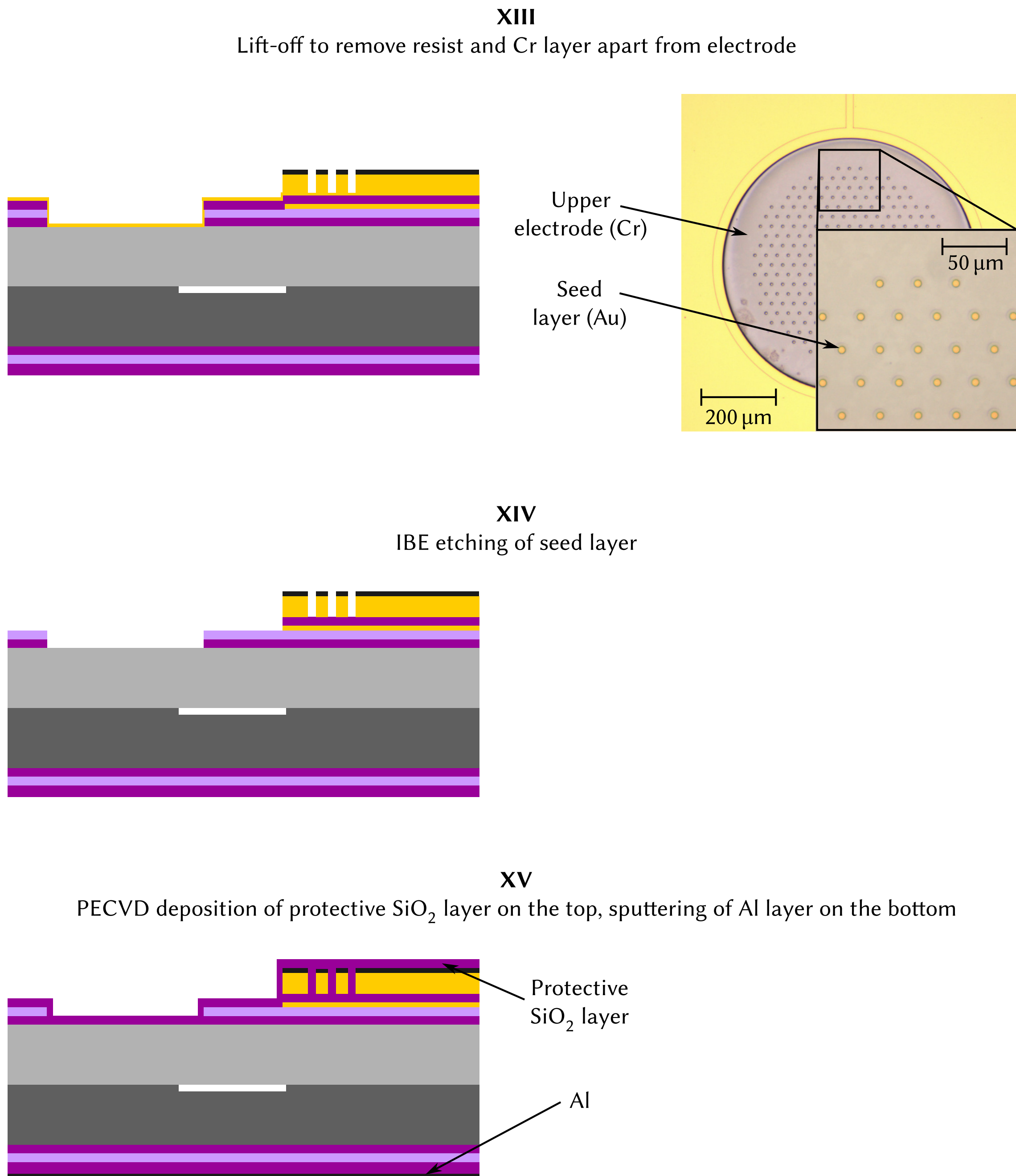

Figure 32: Steps XIII – XV of the micro-technological process flow of the µ-biomimetic sensor. Not to scale.

process during which the wafer is immersed in a resist solvent. The resist is removed and the chrome on top of the resist is lifted off (XIII). The fabrication of the upper electrode is finished upon removing the seed layer using IBE (XIV). To protect the top side of the wafer during the subsequent steps, it is covered by a PECVD SiO_2 layer. An layer of Al is sputtered on the bottom (XV). The Al layer and the underlying SiO_2-Si_3N_4-SiO_2 layer is etched using IBE and RIE, respectively, at the positions of the pressure and compensation chamber (XVI). Now, the first half of the Si is etched through by DRIE (XVII). The upper half of the pressure chamber has a smaller diameter than the lower half. However, it is not possible to use photoresist on the bottom side of the wafer due to the deep (300 µm) structures. Instead, the layer stack made of Al, SiO_2, and Si_3N_4 that was structured prior

XVI

IBE etching of Al layer, RIE etching of SiO_2-Si_3N_4-SiO_2 sequence to form a hard mask

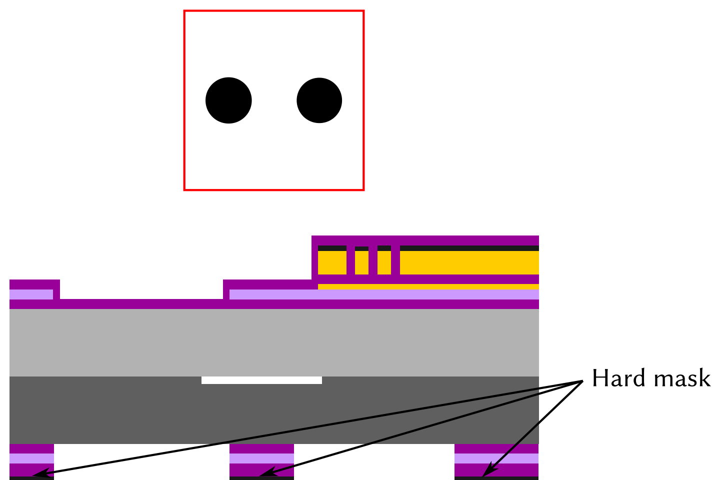

XVII

ICP etching of first half of pressure and compensation chamber

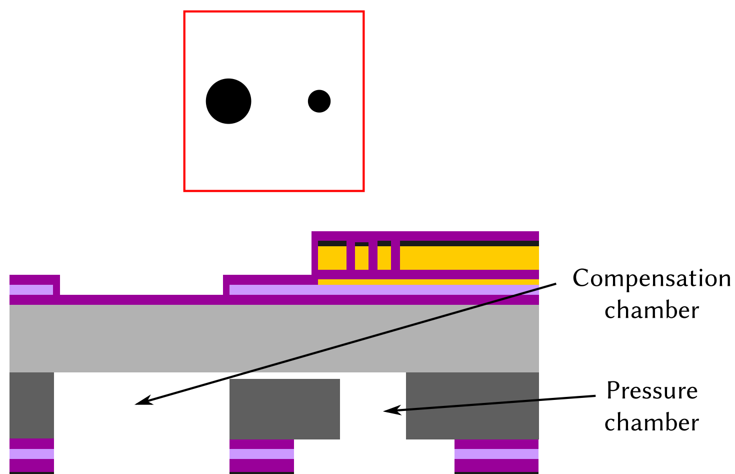

XVIII

ICP etching of second half of the pressure and compensation chamber, IBE etching of Al mask

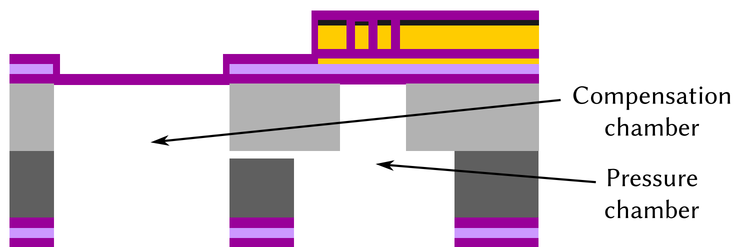

Figure 33: Steps XVI – XVIII of the micro-technological process flow of the µ-biomimetic sensor. Not to scale. The red squares show a detail of the photolithography mask corresponding to a single sensor.

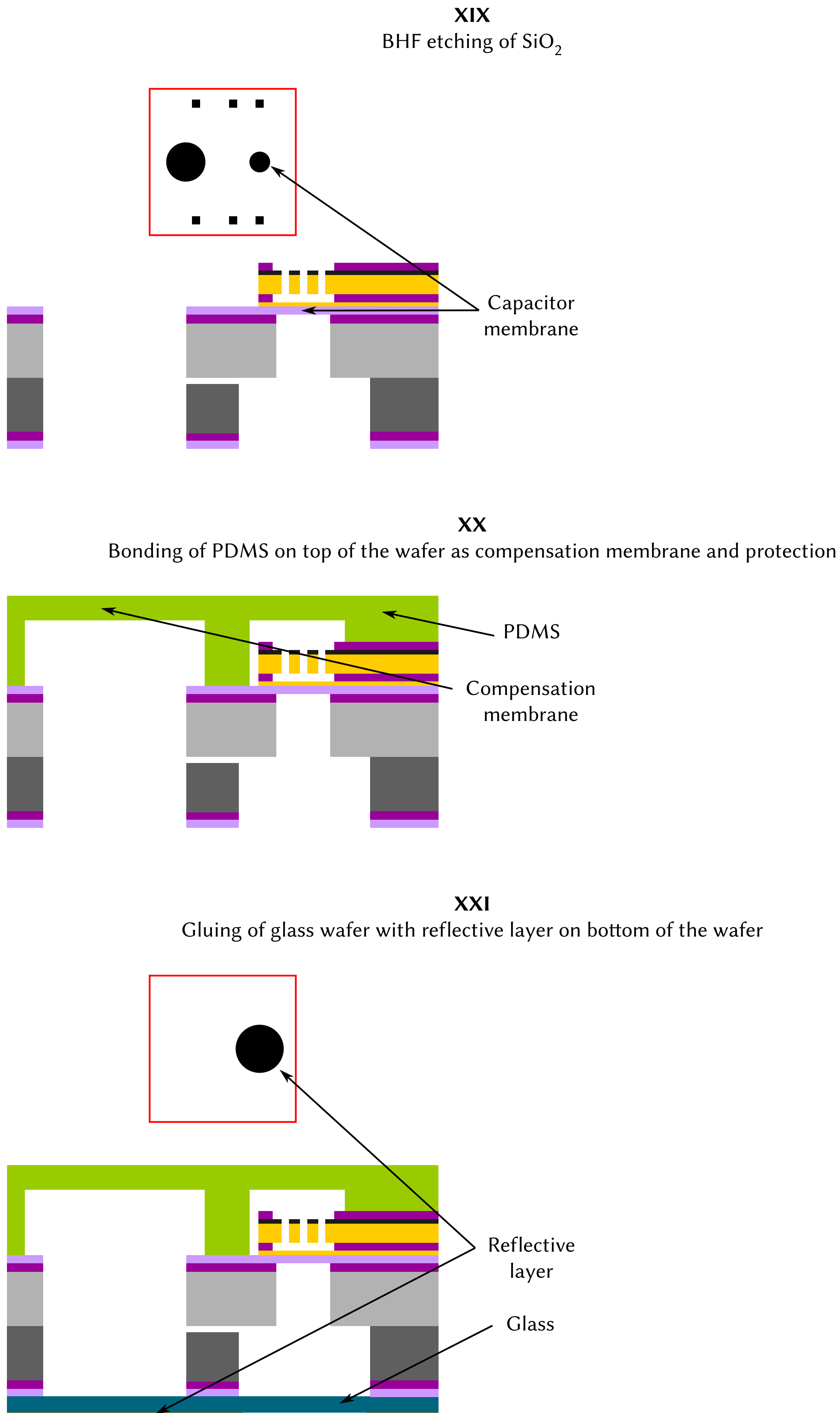

Figure 34: Steps XIX – XXI of the micro-technological process flow of the μ-biomimetic sensor. Not to scale. The red squares show a detail of the photolithography mask corresponding to a single sensor.

to the deep etching, is used as a mask. Again, DRIE is used to etch through the second wafer. However, the DRIE etch process is interrupted shortly before the wafer is completely etched through. The Al layer is removed by IBE and the DRIE is resumed (XVIII). This intermediate step is necessary as the IBE would damage the Si_3N_4 membrane otherwise. To remove the sacrificial layer of SiO_2 between the electrodes and other unneeded SiO_2 structures, the wafer is immersed in BHF (XIX). A cast PDMS structure is bonded on top of the wafer. This structure provides the thin and flexible membrane of the compensation chamber and protects the sensor surface (XX). Finally, the sensors are filled bubble-free with water (see next section) and a glass wafer is glued on the bottom side to close the sensors. The glass wafer is coated with a reflective layer, e.g. gold, except for the pressure chamber (XXI).

4.4 Bubble-free filling and assembly

The final steps of the fabrication of the biomimetic IR sensor consist of the assembly of the Si chip, the PDMS cover, and the glass wafer as well as the bubble-free filling with a suitable liquid, e.g. water. Any bubble present in the sensor will deteriorate the response. First, bubbles will shrink if the pressure increases. This reduces the deflection of the membranes of the sensor and thereby the sensitivity. Therefore, bubbles lead to a change of the effective spring constant. Second, the presence of bubbles introduces nonlinearities to the sensor response and makes it unpredictable. Therefore, it is pivotal to have a bubble-free sensor. However, the bubble-free filling of channels with a diameter of a few micrometres is a general problem in microfluidics.[1]

4.4.1 Bubble-free Filling

Based on a patented filling method [75], an optimized procedure was developed and successfully tested. In the sensor, the channel is located between two silicon wafers. Therefore, it is almost impossible to check for bubbles in the final setup. In order to characterize the bubble-free filling, a simplified test structure is used for the development of the filling procedure. The second Si wafer is replaced by a glass wafer that is bonded on top of the Si wafer containing the channels and chambers. Figure 35 I shows the simplified cross-section of one sensor prior to the filling procedure as described in the following:

The bubble-free filling starts with the exposition of the sensors to an oxygen plasma (Plasma System 300 Semi-Auto, PVA TePla, Germany; 400 W power, 400 ml min^{-1} O_2). The plasma leads to the hydrophilization of the silicon and glass surfaces [76]. Immediately following the hydrophilization, the sensors are immersed in water. Water enters the channel through both chambers at the same time leading to the inclusion of few bubbles in the channel (Figure 35 II). Apart from the bubbles, the channel is completely wetted. The sensors are removed from the water and placed in a vacuum chamber. Below the sensors, a vessel containing degassed water is located. The pressure inside the vacuum chamber is reduced to 1 mbar – below the vapour pressure of water. Thereby, the air in the vacuum chamber is completely displaced by vapour and the water inside the sensor channel evaporates. The vacuum chamber and the sensor are completely filled with water in gas and liquid phase: the channel in the sensor is fully wetted (Figure 35 III). By means of a moveable stage inside the chamber, the sensor is again immersed in water. Due to the

[1]This section is an excerpt of results that were obtained as part of a bachelor thesis (Thiesler [74]) and were in parts published in Siebke et al. [61].

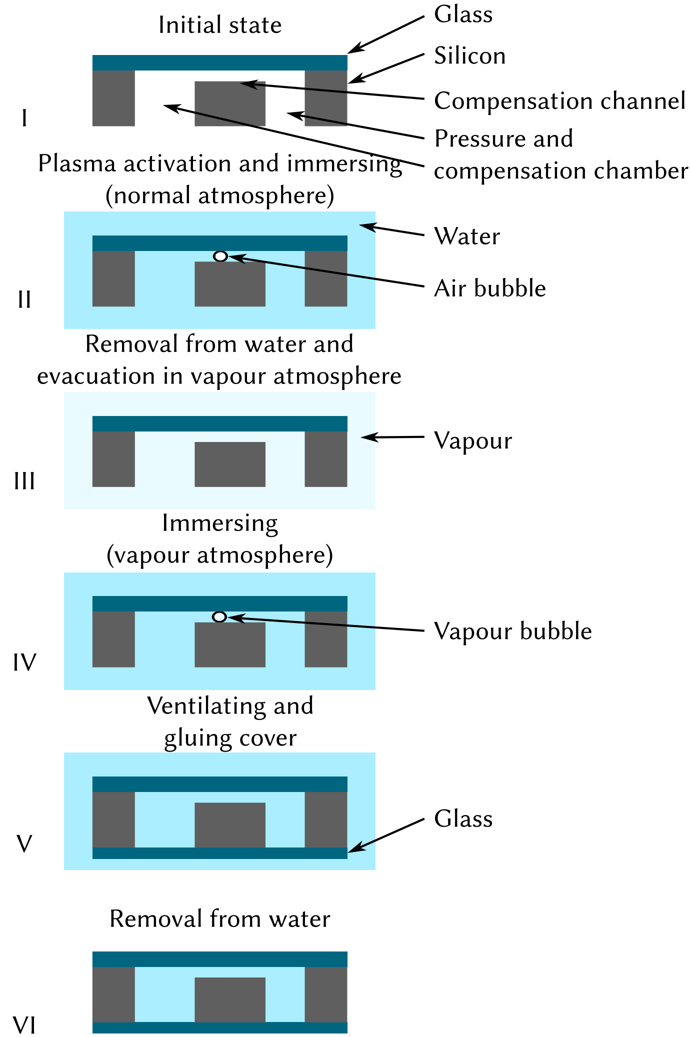

Figure 35: Procedure for bubble-free filling. In the beginning, the sensor is empty. Throughout steps I-VI, the sensor is filled bubble-free with water and is sealed. Not to scale (from Siebke et al. [61]).

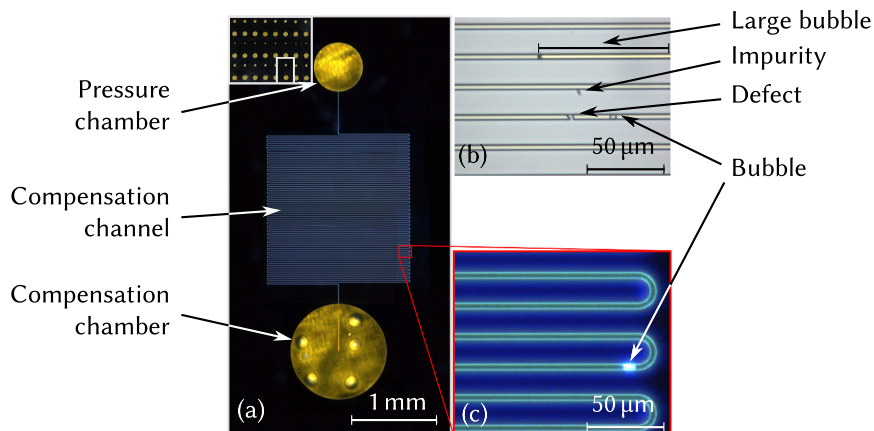

Figure 36: The micro-channel after the filling procedure. (a) Si-chip of a sensor. The inset shows a part of the wafer used for this test. (b) Different kinds of bubbles and other obstructions occurring in the channel. (c) Image taken using dark field microscopy. Bubbles can be easily detected (from Siebke et al. [61]).

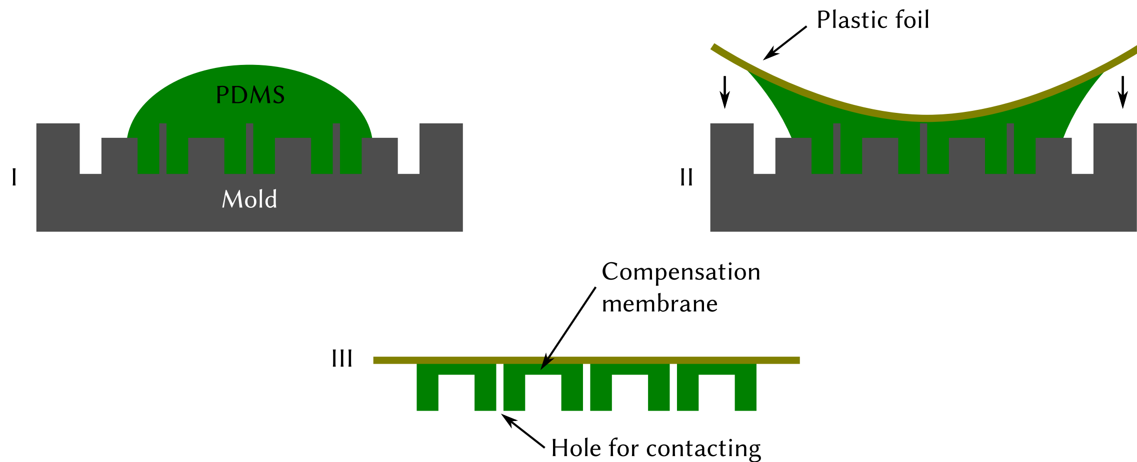

Figure 37: Casting of the PDMS layer. I: The liquid PDMS is cast in an aluminium mould. II: A plastic foil is attached. III: After curing, the foil with the PDMS layer is removed from the mould. Not to scale (after Thiesler [74]).

vapour atmosphere, there is no possibility for an air bubble to be formed. Instead, possible bubbles condense upon venting the vacuum chamber (Figure 35 IV). The sensor is sealed under water by fixing a cover using PDMS glue (Figure 35 V). Finally the sensor can be safely removed from the water-filled vessel (Figure 35 VI).

Figure 36 shows a sensor that is filled bubble-free by this filling procedure. Figure 36(a) shows the sensor chip with the two chambers and the compensation channel. Some bubbles are located in the lower chamber. By sealing the sensor under water, the formation of such bubbles is prevented. Figure 36(b) and (c) show the different defects that can occur during the bubble-free filling. Using the technique described above, it is possible to fill the compensation channels with a diameter of few micrometres with water with a process yield of 95 %.

4.4.2 Manufacturing of the PDMS layer

The PDMS layer fulfils two purposes: At the position of the compensation chamber, this layer is very thin ($\lesssim$ 50 µm) to provide an elastic membrane. The remaining area, most important the capacitor, are protected by the PDMS with a thickness of about 1 mm. Additionally, the layer contains two holes per sensor to electrically contact the capacitor. To fabricate the PDMS layer, PDMS (Sylgard 184, Dow Corning, USA) is cast into an aluminium mould and degassed in a vacuum chamber to remove air bubbles (Figure 37 I). Afterwards, a 0.3 mm thick plastic foil is placed on the still liquid PDMS (II) and pressed against to squeeze out excess material. After curing at 80 °C, the rigid plastic foil is used to remove the soft PDMS from the mold and to transfer it to the silicon wafer containing the sensors.

4.4.3 Assembly of the sensor

After the micro technological processing, three steps are remaining to assemble the complete sensor (Figure 38). In the first step, the PDMS structure is glued on the top (I). A thin layer of of PDMS (Sylgard 186, Dow Corning, USA) applied to the PDMS structure is used as glue and is cured at 80 °C afterwards. In the second step, the sensor is filled bubble-free with water (II, see above). While the wafer containing the sensor is immersed in water,

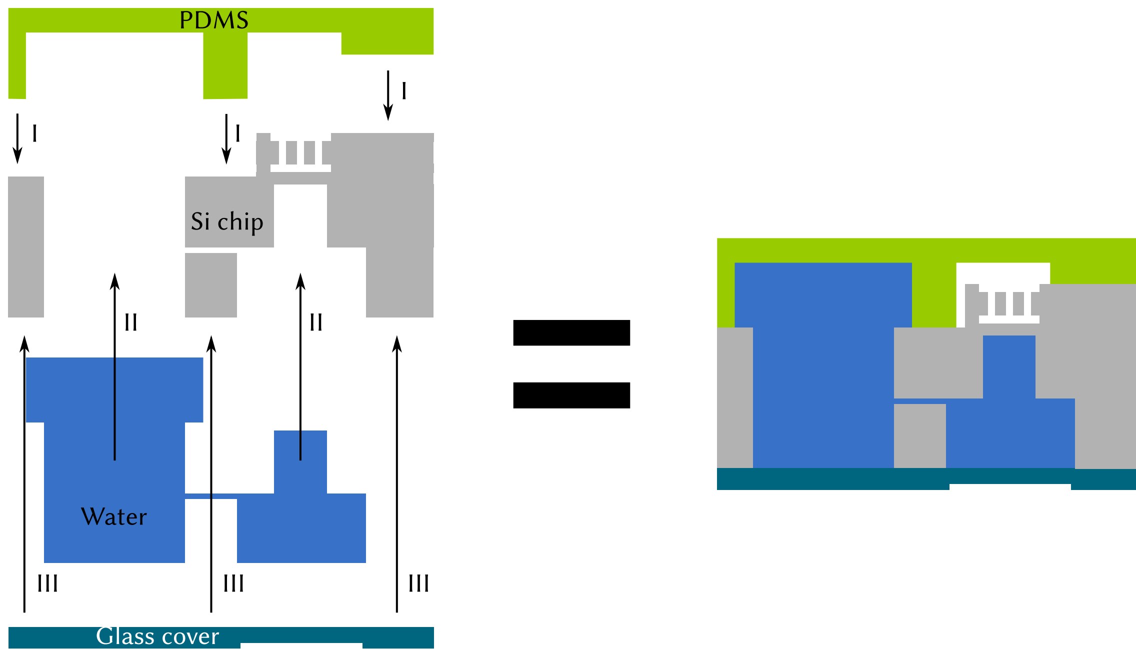

Figure 38: Assembly of the µ-biomimetic sensor. I: The PDMS layer is attached to the Si-chip. II: The system is filled with water bubble-free. III: The glass cover is glued. Not to scale.

the glass wafer with a reflective coating is glued on the bottom side to close the sensors. To accomplish this, the glass wafer is coated with PDMS (Sylgard 186). The PDMS cures under water and the sensors can be taken out.

5 Readout of the μ-biomimetic sensor

To employ the μ-biomimetic sensor, additional components are required (Figure 39). First, the capacitance has be to measured continuously. Second, the recorded data has to be analysed and the amplitude for the used modulation frequency has to be calculated. In this work, the measurement of the capacitance is done using a tailored electronics. The measured data is transmitted to a computer which carries out the analysis. In the future, the analysis can be integrated into the electronics. However, at the moment, the split solution is preferred due to the higher flexibility of a computer software compared to an electronics with a fixed range of functions. The development of the electronics and the software is presented in the next two sections. In order to characterize the IR sensor, a modulated IR source is needed in addition to the measurement electronics. In Section 5.3, the IR radiator developed in this work is presented as well as the complete test setup used to characterize sensors (see also Chapter 6).

5.1 Measurement electronics

The measurement electronics mainly consists of three parts (Figure 40). The most important part is the capacitance-to-digital converter (CDC). It measures the capacitance and provides digital data to a microcontroller. The microcontroller controls the CDC and converts the measured data to a suitable form to be transmitted to a computer. The data is transmitted via USB (universal serial bus). However, there is no electrical connection between the microcontroller and the computer. Instead, the data is transmitted via a digital isolator to galvanically decouple the computer and the electronics. The electronics boards is produced in two variants. One includes the CDC on the same PCB (printed circuit board) and is used to connect capacitors on a wafer using a test probe. The other board does not include the CDC. Instead, it is located on a separate PCB that is directly connected to a PCB containing a sensor to minimize the lead length.

The deflections of the capacitor membrane that are expected for the biomimetic sensor are very small ($\lesssim 1\,\mathrm{nm}$). To compensate the small deflections, the change in capacitance has to be measured with the highest possible resolution. The AD7745 (Analog Devices, USA) is able to measure capacitance changes with a resolution of down to 4 aF with a full range of ±4 pF. The accuracy of the CDC (4 fF) is much worse than the resolution. However, due to the modulated input, only changes in capacitance need to be measured.

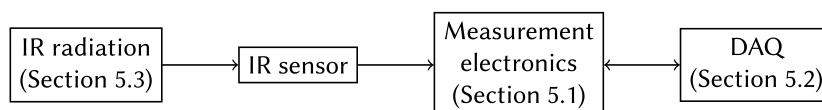

Figure 39: Components required to characterize an IR sensor.

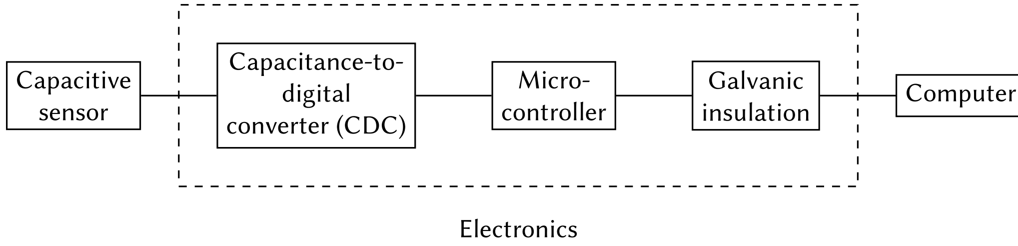

Figure 40: Components of the electronics used to read out the μ-biomimetic IR sensor.

Resolution @ 9 Hz	4 aF
Resolution @ 16 Hz	5 aF
Resolution @ 90 Hz	40 aF
Accuracy	4 fF
Range	4 pF
Capacitive offset	17 pF
Measurement rate	9 Hz to 90 Hz

Table 9: Properties of the capacitance-to-digital converter AD7745 [77].

Therefore, the ability to measure constant capacitances is negligible. Furthermore, the input range can be shifted by an offset of up to 17 pF to allow measurements in the range of 17 ± 4 pF. This feature allows to further increase the sensitivity by using capacitors with a larger base capacitance and thus larger changes. At the same time, the resolution is not impaired for larger capacitances. The actual resolution of the CDC depends on additional factors. The CDC itself can be operated at different speeds. In general, a lower speed corresponds to a better resolution (Table 9). However, the resolution of the CDC is impaired by environmental influences, e.g. electromagnetic noise due to AC power lines. At a measurement frequency of 16.1 Hz, signals with a frequency of 50 Hz and 60 Hz are strongly suppressed. Experimental tests verified that the frequency of 16.1 Hz provides the best resolution. Even higher frequencies provide a worse resolution and, in addition, cannot be exploited due to the current speed of the data transmission.

During the capacitance measurement, a voltage is applied to the capacitor. The voltage can be adjusted between $\pm V_{DD}/8$ and $\pm V_{DD}/2$, where V_{DD} is the supply voltage of the CDC. Due to the small electrode distance, the capacitor is susceptible to electrical breakdown at small voltages. With a breakdown field strength of $3.0\,\mathrm{kV\,mm^{-1}}$ [78] and a plate distance of 500 μm, this voltage is as low as 1.5 V. Therefore, the lowest voltage compatible to all ICs of 3.3 V is chosen and measurements should be carried out at $\pm V_{DD}/4$ or less. In addition to the capacitance measurements, the CDC is able to measure the temperature on-chip or with an external probe, the supply voltage, and an external voltage.

The CDC is connected to a microcontroller (ATmega8L, Atmel Corporation, USA) via I²C (a serial data bus). Depending on the application, the CDC is located on the same PCB as the remaining electronics, or it is placed on a separate, small PCB that is located as close a possible to the sensor to minimize lead lengths. As the data is transmitted digitally between the CDC and the microcontroller, the measured information is not deteriorated by to additional cables. The data transmitted by the CDC has to be decoded and converted into suitable units before it can be analysed. The software that runs on the microcontroller (the *firmware*) controls the CDC, receives and converts measured data, and is responsible for

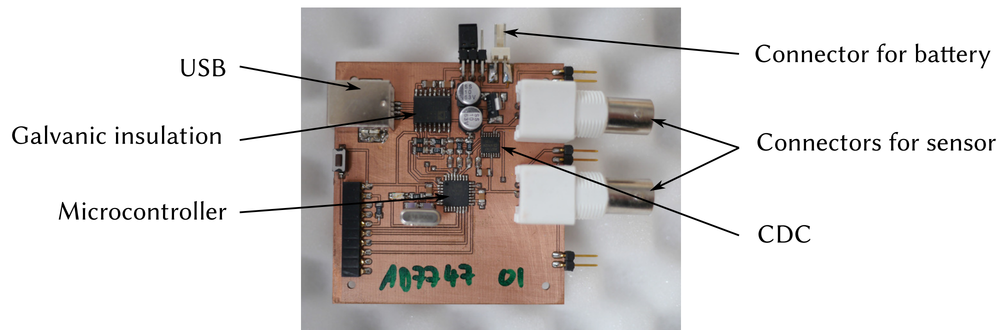

Figure 41: Electronics board for the read out the µ-biomimetic IR sensor.

the communication with a computer via USB. The aim of the software development was to carry out as much calculations as possible on the microcontroller instead of the computer. Additionally, it should be able to control the CDC without external input. This design was chosen to simplify the transition from the current setup, which still requires a computer for operation, to a stand-alone system. Such systems could be equipped with a display for the measured heat flux. To further simplify the transition, the software was coded in a modular way, simplifying the addition of further functions in future developments. One additional task that is performed by the firmware is the initialization of the capacitive offset. When the CDC is powered on, the capacitive range is ±4 pF. By issuing a command to the firmware, it iteratively increases the capacitive offset until a capacitance can be measured. Then the offset is further adjusted to centre the capacitance around zero.

To keep the cost of the electronics low and to reduce power consumption, no dedicated USB transmission IC is employed. Instead, the firmware makes use of the software-only implementation V-USB (Objective Development Software GmbH, Austria [79]). Using this piece of software, only few additional passive electronic components are required to create a USB compliant device. It features a limited, but sufficient speed and has demonstrated high stability.

To prevent the transmission of noise from the computer to the measurement electronics via the USB line, a galvanical insulation is employed. Such an insulation is non-trivial for a bidirectional interface like USB as the same leads are used for both directions. To accomplish the insulation, the ADum3160 (Atmel Corporation, USA) Digital Isolator is used. This IC detects the transmission direction and switches accordingly. The downside of the galvanical isolation is the requirement of an additional power supply. As the total power consumption of the electronics is only about 30 mW [77, 80, 81], standard alkaline AA batteries are used to provide a noise-free supply.

5.2 Data acquisition (DAQ)

The computer which the electronics is connected to runs a purpose-built software. The software fulfils three tasks (Figure 42): First all necessary parameters of the CDC can be adjusted. These include the measurement time for the capacitance and voltage channels, the voltage applied to the capacitor during the measurement, and a capacitive offset. Second the software records samples at an adjustable rate. Third it displays a real-time FFT (fast fourier transform) spectrum for monitoring the measurement process.

Figure 43 shows the start screen of the graphical user interface (GUI) of the software. Before a measurement can be started, the connection to the electronics has to be established.

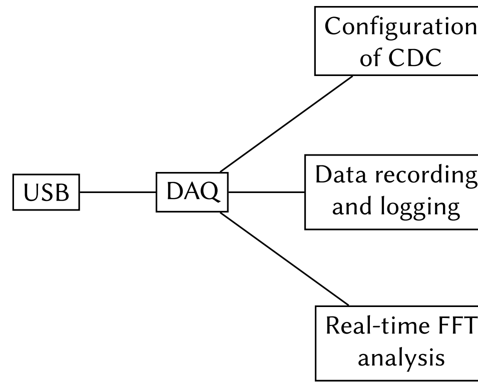

Figure 42: Functions of the data acquisition software.

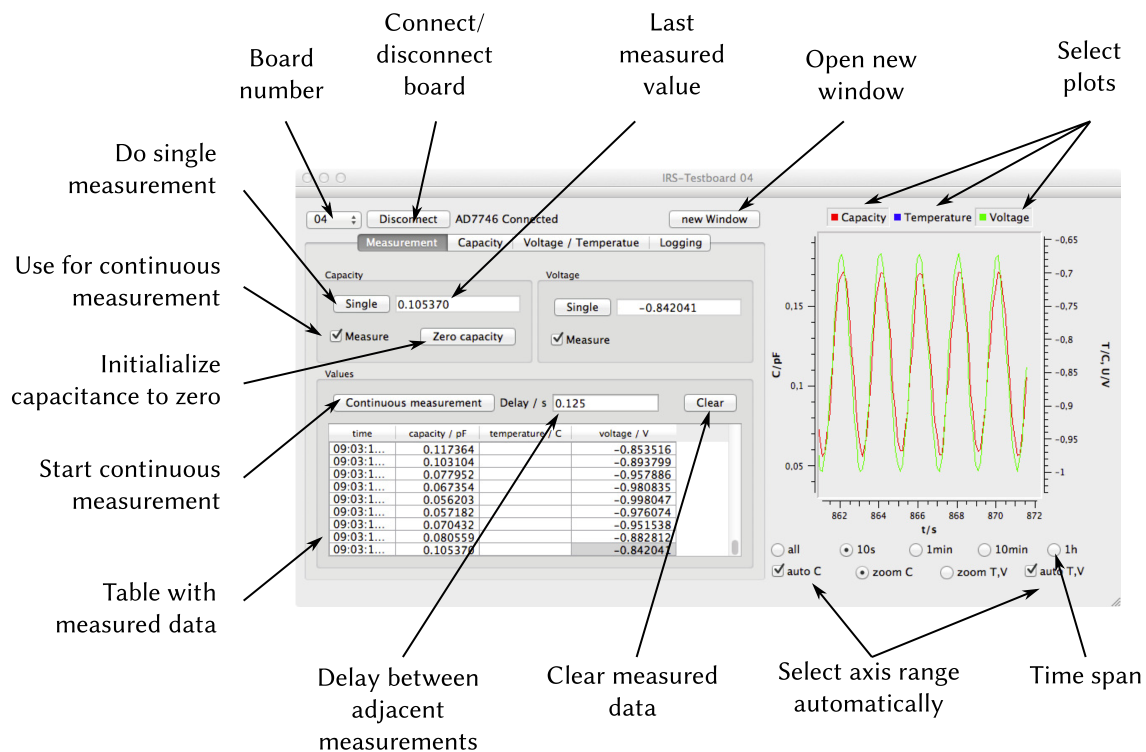

Figure 43: Window of the DAQ used to start and stop measurements and plots of the capacitance, temperature, and voltage.

Each electronics board has a different number that can be selected before connecting. Due to the different numbers, simultaneous measurements of several sensors are possible. After connecting, the measurement can be started directly. However, if the capacitance is larger than 4 pF, the capacitive should be initialized first via the “Zero capacity” button. By using the “Single” buttons, a single capacitance, voltage, or temperature is measured. To do continuous measurements, the respective “Measure” box has to be checked and the measurement can be started using the “Continuous measurement” button. The delay between two adjacent measurements can be set using the “Delay” field. All measured values are displayed in a table as well as plotted in the right side of the window. The plot can be adjusted to show the capacitance, voltage, and/or the temperature. Furthermore, the

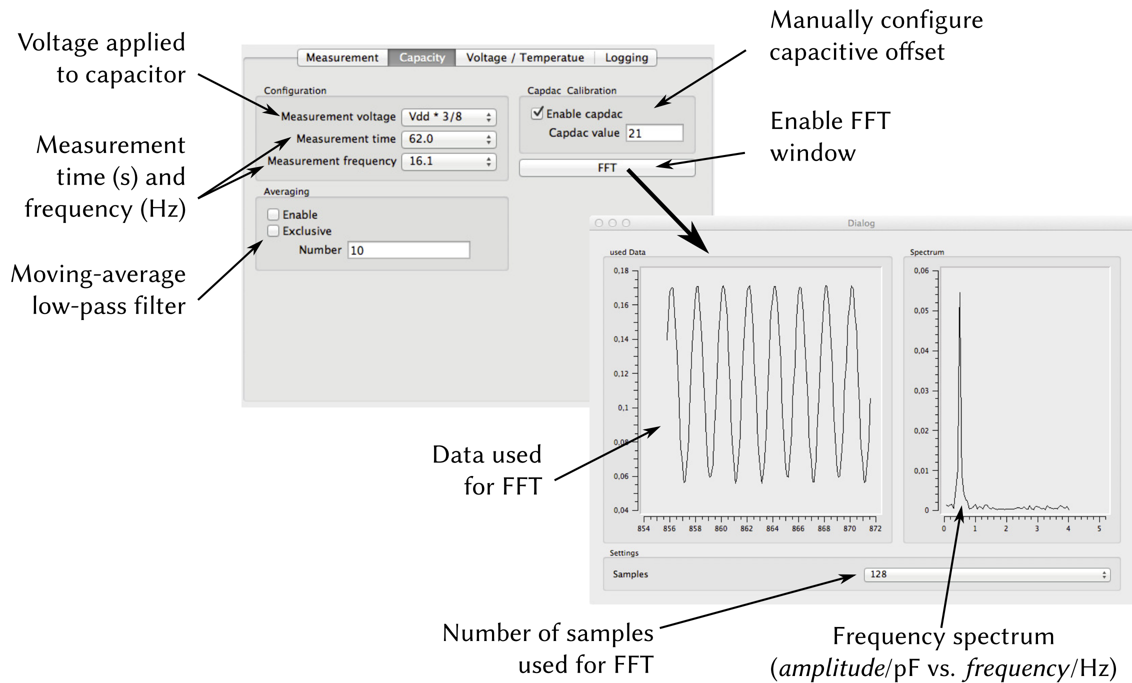

Figure 44: Windows of the DAQ used to configure the capacitance measurements and for the real-time FFT.

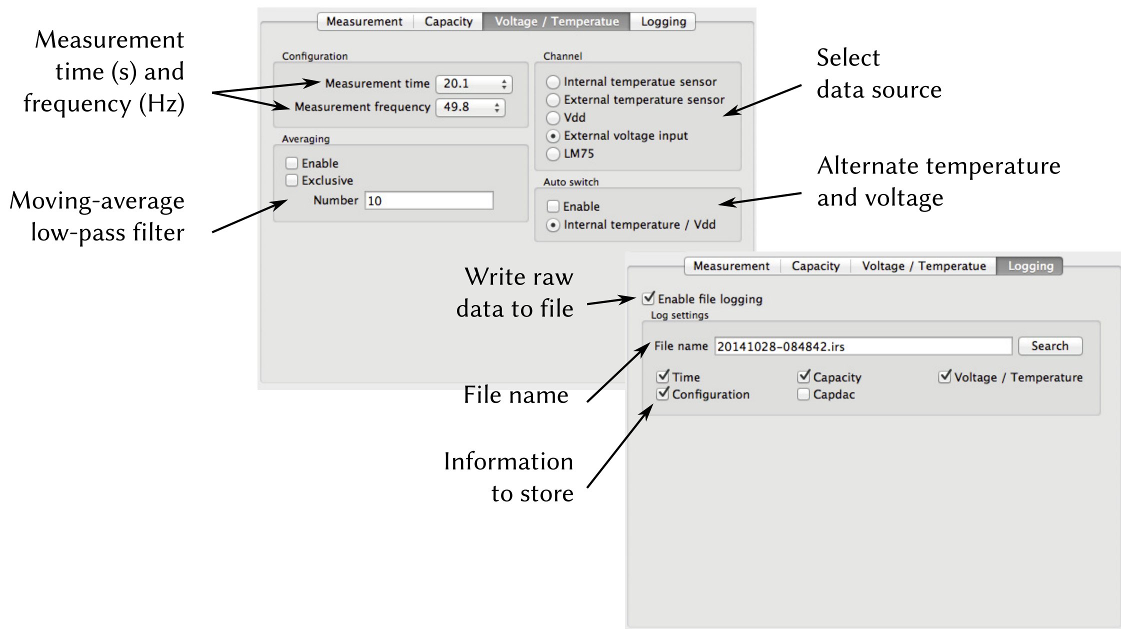

Figure 45: Windows of the DAQ used to configure the voltage and temperature measurements and the storage of measured data.

time span between the most recent measurement and the last measurement that should be displayed can be chosen.

By selecting the “Capacity” tab, various settings of the CDC can be adjusted (Figure 44). The most important settings are the measurement time and the voltage that is applied to the capacitor during the measurement (see above). Additionally, the capacitive offset can be set manually if required. Usually this is done automatically by the firmware of

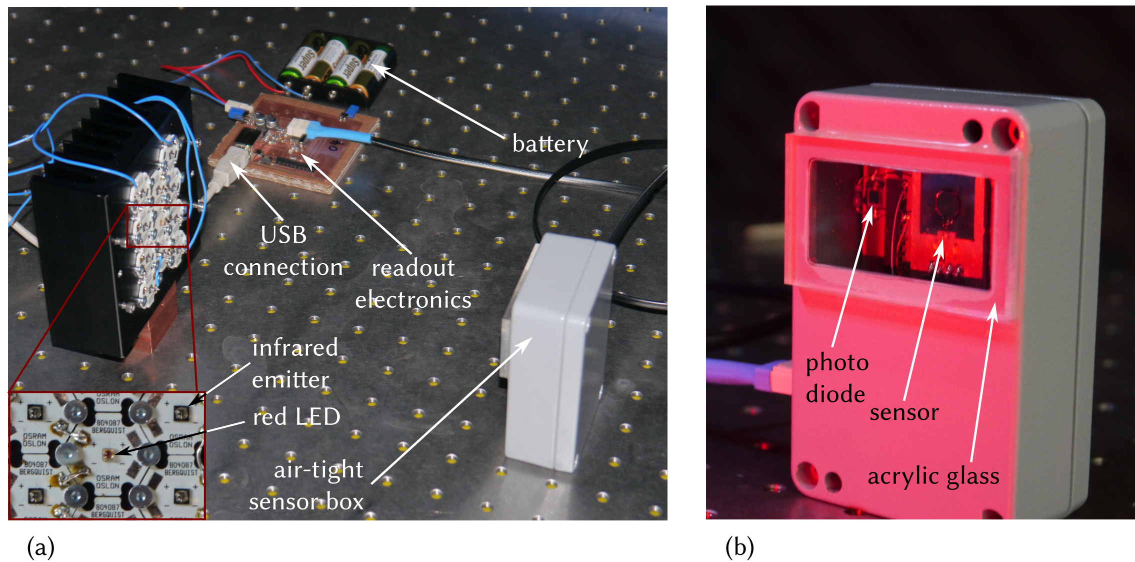

Figure 46: Experimental setup for testing the sensors. (a) The IR emitter array, the readout electronics and the sensor box. (b) The illuminated air-tight sensor box including the frontend electronics, the sensor, and a photo diode.

the electronics. To filter noise from the measured data, a moving-average low-pass filter can be activated. Note, however, that the filtered data is only displayed in the software. Further analysis is always based on the raw, unfiltered data. To monitor the frequency-dependent amplitude in real-time during the measurement, a second window can be opened that displays the frequency spectrum calculated by a fast Fourier transform (FFT). In this window, the number of samples used for the FFT can be chosen. Afterwards the data set used to calculate the current spectrum is displayed on the left side. The frequency spectrum is shown on the right side.

Figure 45 shows the configuration of the voltage and temperature measurement and the data logging. As stated above, the CDC can measure voltages and temperatures in addition to the capacitance. However, only one voltage or temperature can be measured at a time. The current source can be selected on the “Voltage/Temperature” tab. Alternatively, the software can alternately record the internal temperature and the external voltage. As for the capacitance, the measurement time or frequency can be set and a moving-average low-pass filer can be activated.

As the software only contains simple analysis methods, the final evaluation is carried out using further tools. Therefore, the measured data can be stored in a file (Figure 45, “Logging” tab). The information that is stored can be selected precisely. By default, all data is stored in a file named after the current date and time.

5.3 Test setup

To characterize an IR sensor, the sensor and the CDC are mounted in an airtight metal box with a window made of transparent acrylic glass (PMMA) (Figure 46(b)). This enclosure removes the influence of the air pressure inside the laboratory, which often changes due to the air condition, doors opening and closing, etc. In this case, the split electronics is used. The CDC is inside the enclosure, close to the capacitor, whereas the other PCB is connected to the box by an additional cable (Figure 46(a)). During a measurement, the box

with the sensor is placed in front of a modulated IR source. A second box was constructed that allows to precisely heat the sensor.[1] At the back of this box, a Peltier element with a block of copper in between is mounted. The block of copper stabilizes the temperature and contains a temperature probe. The Peltier element is driven by a controller circuit (QC-PC-CO-CH1 in conjunction with QC-PC-D-CH1, Quick-Ohm Küpper & Co., Germany). The temperature controlled box is placed in a shell made of expanded polystyrene as thermal insulation.

Usually, black-body radiators are used to characterize IR sensors. However, they are slow and need mechanical modulation, e.g. by a chopper wheel (see Section 2.2.2). To simplify the characterization process in this work, an IR source based on semiconductor IR emitters was developed (Figure 46(a)). The source consists ten OSRAM SFH 4725S [82] IR-emitters with a total radiant flux of $\Phi = 935\,\mathrm{mW}$ each and a peak wavelength of $\lambda = 940\,\mathrm{nm}$ and one red OSRAM LH CP7P [83] LED with a total radiant flux of $\Phi = 940\,\mathrm{mW}$ and a peak wavelength of $\lambda = 645\,\mathrm{nm}$ for security reasons. These values are mean values for a current of $I_f = 1\,\mathrm{A}$ and can be slightly different for the equipped emitters. All emitters are mounted on a large heat sink to prevent overheating. As the radiation of the IR-emitters is barely visible, the red LED is used to align the array at a low power. The emitter array is controlled by an external electronics. The electronics contains two constant current LED sources. They are sinusoidally modulated by a PWM (pulse width modulation) signal generated by a microcontroller. The firmware allows to set different modulation frequencies and to run programmable sequences. Once set up, a single chip is measured without further interaction. For most tests, five different modulation frequencies between 1/16 Hz and 1 Hz are chosen. Higher frequencies could only be measured with reduced resolution of the CDC and are omitted for this reason. To measure the phase between the irradiation and the sensor response, a photodiode is used. Together with a parallel resistor, it is attached to the voltage input of the CDC (Figure 46(b)).

As the narrow-band radiation from the IR source shown here is different from the broad-band radiation emitted by a black body radiator, the response of both cannot be directly compared. However, the IR array can be used to compare sensors of the same kind throughout this work. Furthermore, the comparatively short wavelength allows to omit an absorber on the silicon surface of the sensor. At larger wavelengths, silicon becomes transparent and absorbs less radiation. Therefore, depending on the field of application, different absorber materials have to be chosen. Using the IR array, this is not required for test purposes. It is the other way round for the PMMA window. It is transparent for the IR array, but becomes opaque for large wavelengths. Finally the electronic modulation rules out a source of fake signals: As the changes in capacitance are very small, the movement of material near the sensor can induce similar changes. It was found out that a chopper wheel rotating in front of the sensor can produce a signal that cannot be distinguished from the actual IR signal.[2]

The distance between the IR-emitters and the sensor is 20 cm. The maximum irradiance for a current of $I = 1\,\mathrm{A}$ at this distance is calculated to be $E_{pp} = 116\,\mathrm{W\,m^{-2}}$. Therefore, the amplitude for a sinusoidal oscillation of the emitter current between 0 and I_f is $E_0 = \frac{1}{2}E_{pp} = 58\,\mathrm{W\,m^{-2}}$. The complete setup is located inside of a large metal box, preventing disturbances due to electromagnetic radiation.

[1] This box was developed within the scope of a bachelor thesis (Thiesler [74]).

[2] This test was made in cooperation with the institute of zoology of the university of Bonn.

6 Proof of the detection principle on a larger scale

The sensor as described in Chapter 4 is a complex system, combining several distinct features. Each of the features introduces additional steps in the production process and its functioning needs to be verified. First and foremost, there is the pressure chamber with the capacitor membrane on top. This combination is the key feature of the sensor and is responsible for the actual measurement. Second, there is the compensation mechanism, consisting of the micro-fluidic system, the compensation chamber, and the PDMS membrane. The compensation mechanism does not improve the sensitivity but rather prevents damage to the sensor. Its theoretical behaviour is described and verified in Sections 3.1 and 3.4. Lastly the final sensor is filled with water. The feasibility of the bubble-free filling was shown in Section 4.4.

To study the influence of different design parameters solely on the sensitivity of the sensor, there is no need to look at the complete and miniaturized sensor. Rather, it suffices to study the pressure chamber and the capacitor without the compensation mechanism. Therefore, a simplified variant of the sensor was developed on a larger scale. This consists only of the capacitor and the pressure chamber. Due to the simpler layout and the larger size, it shortens the fabrication process drastically. In general, this sensor can be filled with water. Here, air-filled sensors are produced and tested as these allow the verification of the simulated spring constant of the Si_3N_4 membrane. This is not possible for water-filled sensors (see Section 6.4.2). Nevertheless, this simplified sensor uses the same capacitive heat sensing mechanism as the micro sensor.[1]

6.1 Design of a simplified sensor

The simplified sensor consists of two Si-chips with an area of 15 mm × 15 mm (Figure 47). On one chip, an electrode is located on a Si_3N_4 membrane as is the lower electrode of the capacitor in the complete sensor. On the other chip, the electrode is fixed. The pressure chamber is sealed by a piece of silicon on top of the assembly. The sensor assembly is placed in the trench of a PCB. This unit of the PCB and the silicon chips is from now on referred to as the simplified sensor. The sensor can be directly connected to a second PCB that contains the CDC of the measurement electronics (see also Section 5.1). In the following, the fabrication of the sensor is described in more detail.[2]

The process starts with a blank Si wafer (Figure 48, 300 µm thick). First 5 µm deep trenches are etched into the silicon which will later contain the electrode and contact pad and are used for gluing (II). The depth of the etching later defines the distance between

[1] Parts of this chapter were published in Siebke et al. [84] and Siebke et al. [61].

[2] The complete sequence is found in Appendix A.

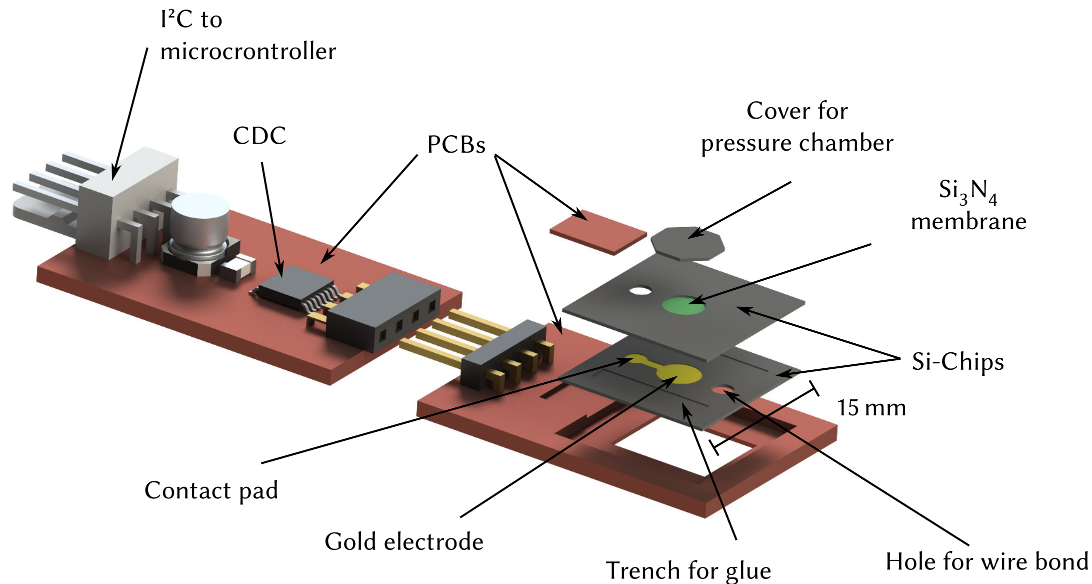

Figure 47: Schematics of the sensor. Drawing of the sensor connected to the frontend electronics. The size of the bond pad and the depth of the trenches are not to scale. The conducting paths on the PCBs are not shown (from Siebke et al. [84]).

the electrodes. Afterwards the wafer is thermally oxidized and a layer of LPCVD Si_3N_4 is deposited to be used as membrane. A layer of gold is sputtered on the top side (III). In the next step, the gold layer is structured to create the electrode, the contact pad and a connecting lead (IV). The capacitor consists of a fixed electrode and a flexible electrode. Therefore, on part of the chips, the Si_3N_4, SiO_2, and Si is removed below the membrane by means of RIE and ICP etching (V left). In addition, holes are created, which are used to contact the electrode on the complete assembly (V left and right). To prevent damaging the membrane due to the low selectivity of the RIE process, the SiO_2 layer below the membrane is removed via BHF wet etching (VI). The residual Si_3N_4 layer above the contact hole is removed mechanically before glue is inserted into the large trenches of one of the two chips (VII). Both chips are put together so that the electrodes face each other and each contact pad is accessible via the hole of the other chip. As the glue is inserted into the trenches, a spreading on the inner surface is prevented. Otherwise, the electrode distance would arbitrarily depend on the amount of glue between the chips. Furthermore, a piece of silicon is glued on top of the pressure chamber (VIII). Finally the two-chip assembly is fixed on a PCB featuring fitting trenches. A small PCB is inserted above the assembly to establish a connection between one chip and the electronics using wire bonds (Figure 50(a)). The other electrode is accessed from the bottom.

The process flow of the simplified sensor is adapted in a way that the number of lithography masks could be reduced to three. After the complete processing sequence, each Si-wafer contains chips with and without membrane. In addition, four different electrode sizes are produced simultaneously. The electrode and membrane sizes can be varied independently by rotating the mask with respect to each other. Altogether, this design allows for a fast production of sensors with varying parameters.

Figure 50(a) shows the chips assembly inside the PCB without the cover. For the shown sensor, the electrode is smaller than the membrane. Due to a small misalignment, part of the lower electrode can be seen through the transparent Si_3N_4 layer. On Figure 50(b),

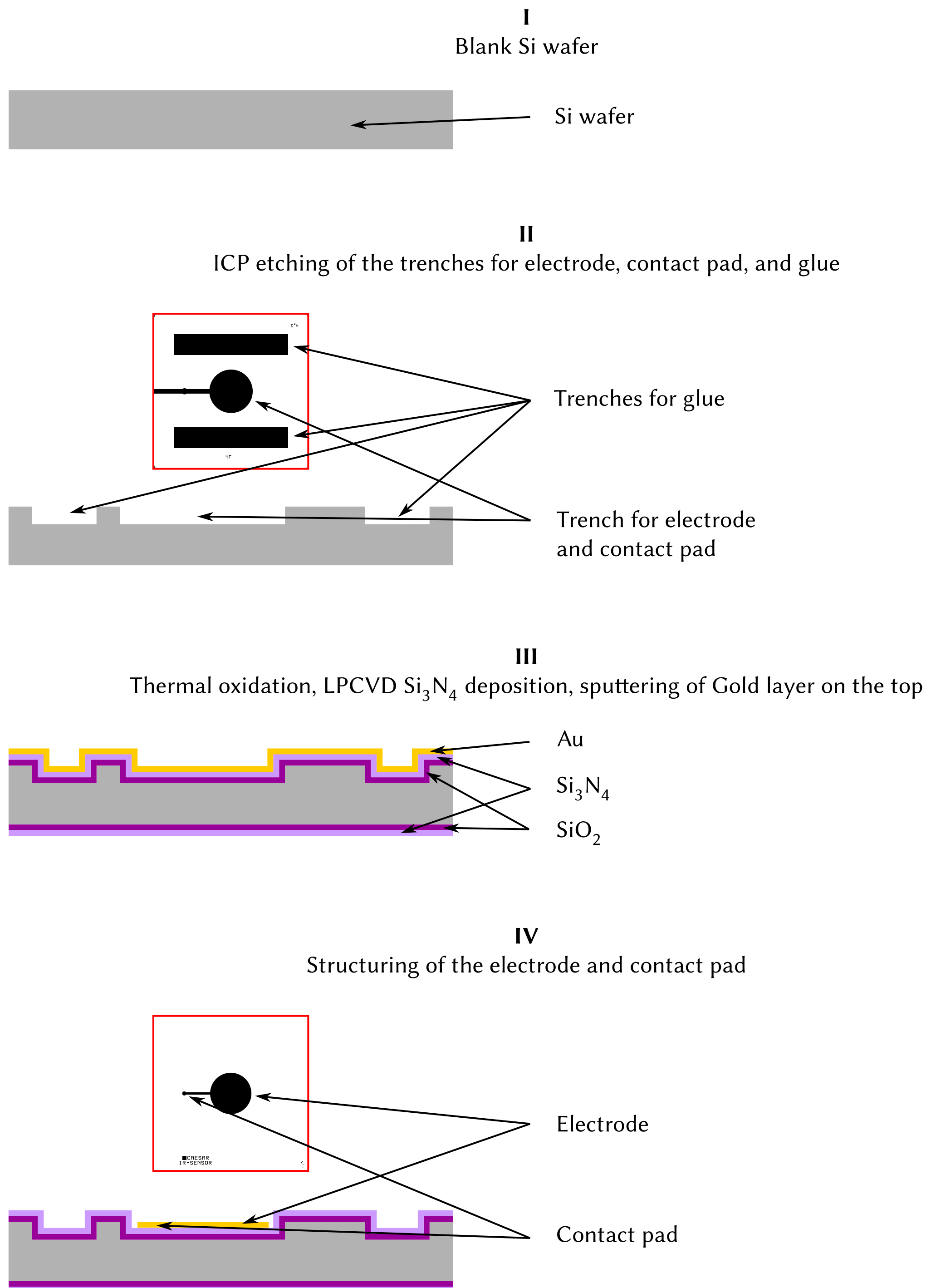

Figure 48: Steps I – IV of the micro-technological process flow of the simplified sensor. Not to scale. The red squares show a detail of the photolithography mask corresponding to a single sensor.

the complete sensor including the CDC is shown. The pressure chamber is closed and to protect the bond wires and the small PCB inset, they are fixated by small amounts of glue.

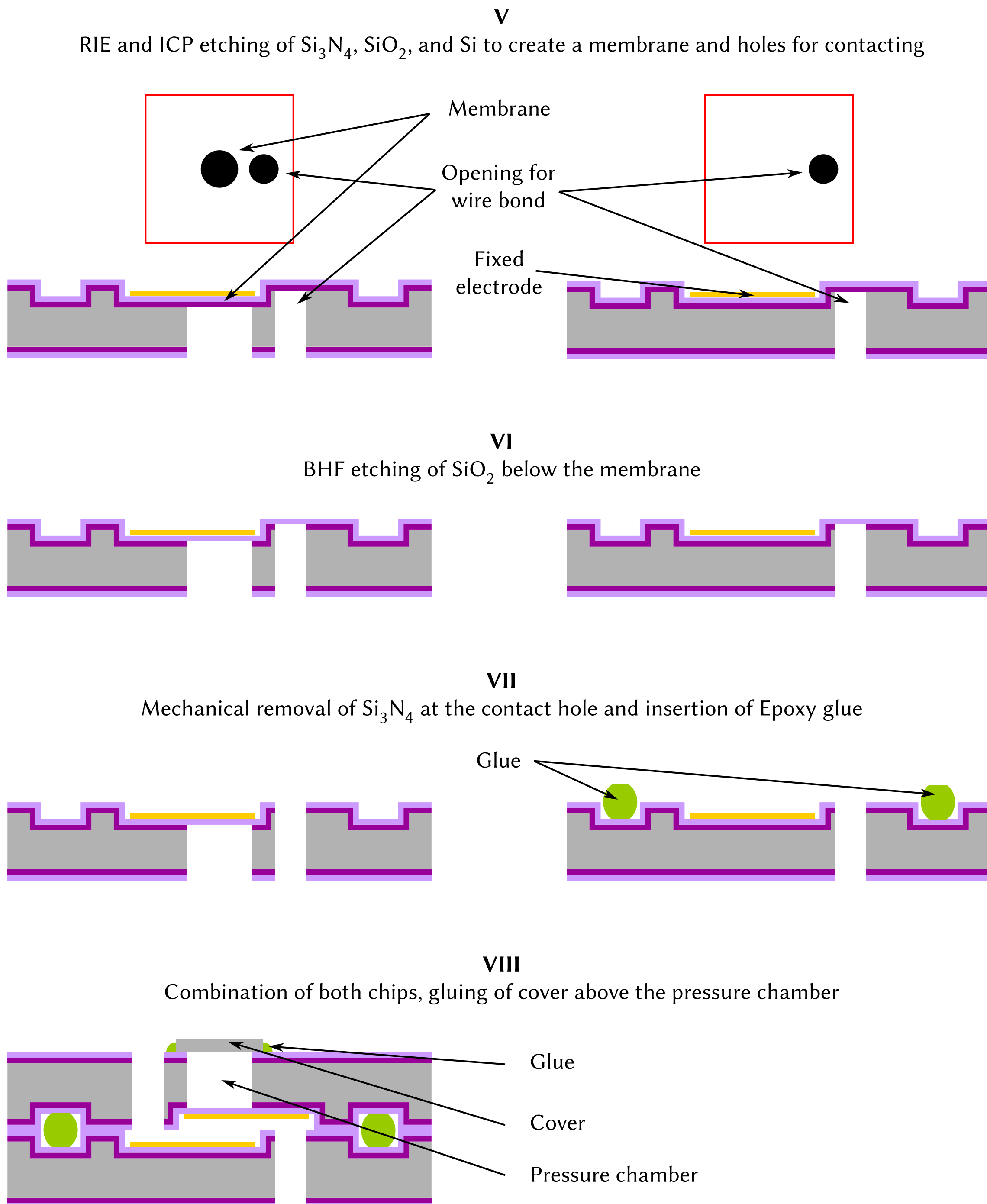

Figure 49: Steps V – VIII of the micro-technological process flow of the simplified sensor. Left and right part correspond to top and bottom electrode. Not to scale. The red squares show a detail of the photolithography mask corresponding to a single sensor.

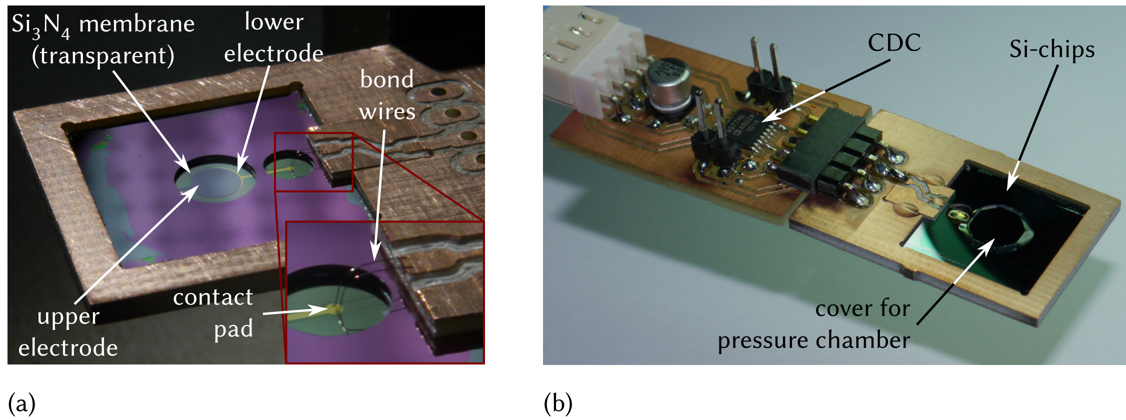

Figure 50: Assembled sensors. (a) Sensor without the cover of the pressure chamber. Membrane diameter is 5 mm, electrode diameter is 3 mm. Due to a slight misalignment of the Si chips with respect to each other, part of the lower electrode is visible through the transparent Si_3N_4 membrane. (b) Complete sensor connected to the frontend electronics. The fragile bond wires are covered by glue as mechanical protection. (adapted from Siebke et al. [84]).

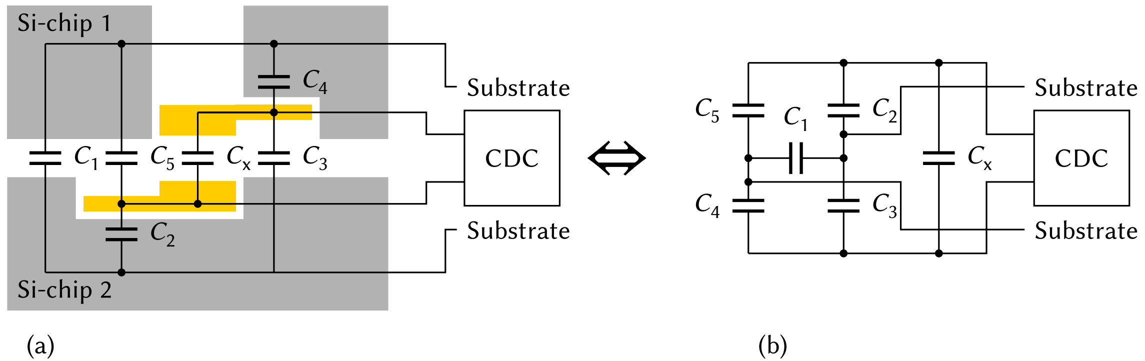

Figure 51: Parasitic capacitances. (a) Occurrence of the parasitic capacitances in the sensor. The drawing only show the Si substrate (grey) and the gold electrodes and leads (yellow). All insulators (air, SiO_2, and Si_3N_4) are represented by empty space. Not to scale. (b) Equivalent circuit of the parasitic capacitances (from Siebke et al. [84]).

6.2 Parasitic capacitances

The capacitors formed by the two electrodes as described in Section 6.1 have a base capacitance (without IR radiation) C_x between 2.8 pF and 17.4 pF. However, in the initial design, the total capacitance connected to the CDC is much larger due to parasitic capacitances. They render the sensor unusable as the total capacitance is increased beyond the range of the CDC. Therefore, different ways to remove or circumvent the parasitic capacitances are discussed in the following.

Parasitic capacitances are inevitably present due to the finite conductance of the Si substrate. Therefore, each combination of (semi)conductor - insulator - (semi)conductor forms a capacitor. All of these combinations can be described by five capacitances (C_1 to C_5, Figure 51):

- C_1 is formed by the two Si chips, taking into account the gold covered areas, the holes, and the trenches,

t_{SiO_2}/µm	0.5		8.0	
$t_{Si_3N_4}$/µm	0.5		1.0	
d/mm	2	3	2	3
C_1/pF	3928.6	3835.0	659.9	645.0
C_2/pF	182.3	360.0	16.0	31.5
C_3/pF	1.3	1.2	1.0	0.8
C_4/pF	64.2	74.1	64.2	74.4
C_5/pF	1.3	1.2	1.3	1.2
C_p/pF	47.7	61.4	13.5	22.1
C_x/pF	2.8	6.3	2.8	6.3
C_{tot}/pF	50.5	67.6	16.2	28.3

Table 10: Parasitic capacitances. t_{SiO_2} and $t_{Si_3N_4}$ are the thickness of the SiO_2 and the Si_3N_4 layer of the chip with the fixed electrode, respectively. For the chip with the membrane, $t_{SiO_2} = t_{Si_3N_4} = 0.5\,\mu m$ for each configuration. d is the membrane and electrode diameter. C_x is the capacitance of the electrodes. C_p is the total parasitic capacitance parallel to C_x. C_{tot} is the total capacitance connected to the CDC (from Siebke et al. [84]).

- C_2 is formed by the Si chip with the fixed electrode and the fixed electrode on the same chip including the lead,
- C_3 is formed by the Si chip with the fixed electrode and the lead of the other electrode,
- C_4 is formed by the Si chip with the movable electrode and the lead of the movable electrode, and
- C_5 is formed by the Si chip with the movable electrode and the lead of the fixed electrode.

For C_4, the electrode itself does not contribute as the silicon on the back side is removed. For the calculation of C_1 to C_5, the different distances due to the trenches as well as the relative permittivities ε of SiO_2 and Si_3N_4 are taken into account. In general, the formula used to calculate the parasitic capacitances is

$$C_i = \varepsilon_0 \int_A \mathrm{d}A' (t_{\mathrm{air}} + t_{\mathrm{SiO_2}}/\varepsilon_{\mathrm{SiO_2}} + t_{\mathrm{Si_3N_4}}/\varepsilon_{\mathrm{Si_3N_4}})^{-1}, \tag{95}$$

where A is the area and t is the layer thickness ($\varepsilon_{SiO_2} = 3.9$ [85], $\varepsilon_{Si_3N_4} = 8.0$ [86], $\varepsilon_0 = 8.9\,\mathrm{pF\,m^{-1}}$). The total parasitic capacitance C_p of Figure 51 is calculated using Kirchhoff's circuit laws by solving the following linear system:

$$C_1 U_1 = C_2 U_2 + C_3 U_3, \tag{96}$$
$$C_1 U_1 = C_4 U_4 + C_5 U_5, \tag{97}$$
$$C_3 U_3 = C_p U_p + C_4 U_4, \tag{98}$$
$$-U_5 = U_1 + U_2, \tag{99}$$
$$-U_3 = U_1 + U_4, \tag{100}$$
$$-U_p = U_1 + U_2 + U_4 \tag{101}$$
$$\Rightarrow C_p = \frac{C_1(C_2+C_5)(C_3+C_4) + C_2C_3(C_4+C_5) + C_4C_5(C_2+C_3)}{C_1(C_2+C_3+C_4+C_5) + (C_2+C_3)(C_4+C_5)}, \tag{102}$$

where U_i is the voltage along C_i. The total parasitic capacitance is connected in parallel to C_x. Therefore, $C_{tot} = C_p + C_x$ is the total capacitance connected to the CDC. Using

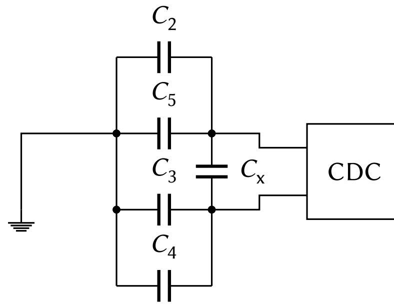

Figure 52: Equivalent circuit of the parasitic capacitances after the connection of the Si substrate to ground. C_1 is omitted as both terminals are interconnected (from Siebke et al. [84]).

the standard layer thicknesses for the Si_3N_4 and SiO_2 layers of 0.5 µm each, the resulting total capacitances are too large (Table 10) to be measured by the CDC. To circumvent this problem, three different methods were tried, which are described in the following sections.

6.2.1 Substrate grounding

The first and simplest solution is to use a feature of the CDC that allows for large parasitic capacitances to ground. Any capacitance connected between one of the CDC pins and ground should not affect the measurement. By connecting the Si substrate of the two sensor chips to ground, the circuit simplifies from Figure 51 to Figure 52. C_1 vanishes completely, as both terminals are connected to ground level. Now, only C_x should be visible to the CDC. In reality, however, this solution cannot be employed. On the one hand, the total capacitance seen by the CDC is now sufficiently small. On the other hand, there is a strong dependence of the capacitance upon the illumination of the silicon. An increase of the light level leads to an immediate decrease of the capacitance and vice versa. This is contrary to the expected behaviour for two reasons. First, the response of the sensor has inverse phase with respect to the light level. For the sensor, the capacitance is expected to increase at the same time as the volume of the pressure chamber expands. Second, a visible retardation of the response with respect to the input signal is expected. As neither is the case, a different mechanism is deduced. The wavelength corresponding to the band-gap energy of Si is $\lambda_g = 1.1$ µm. Therefore, the absorption of visible light and near IR radiation leads to the production of charge carriers. These in turn increase the conductance of the Si, improving the coupling of the substrate to ground level. For the CDC it now seems that less of the parasitic capacitances is connected, leading to an apparent decrease of the sensor capacitance. As the wavelength of the IR radiator is below λ_g, the apparent change in capacitance is due to the photoconductive response of the silicon substrate.

6.2.2 Thickening the insulating layers

The second solution is to avoid large parasitic capacitances in the first place. As the capacitance is anti-proportional to the distance of the electrodes, it can be reduced by increasing the thickness of the insulating SiO_2 and Si_3N_4 layers. However, the processing imposes certain limits and the layer thickness cannot be chosen arbitrarily. The time for the thermal oxidation to produce a SiO_2 layer grows exponentially with the thickness whereas Si_3N_4 layers tend to burst with increased thickness. In addition, the layer thickness cannot be changed for the chip with the membrane. An increase of thickness of the Si_3N_4 layer results in a stiffer membrane and thus in a less sensitive sensor. An increase of the thickness

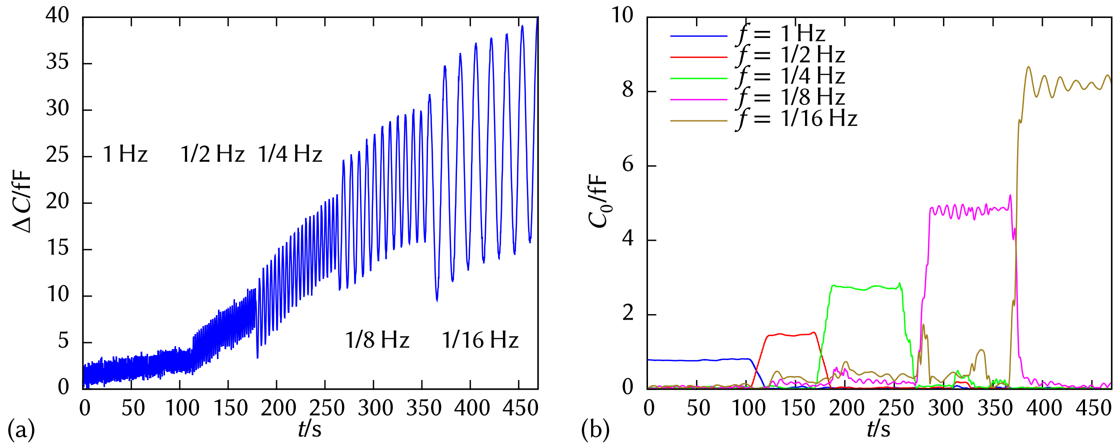

Figure 53: Sample measurement for different modulation frequencies with reduced time spans. (a) Raw data. ΔC is the measured capacitance relative to an arbitrary offset. The drift is due to the overall heating of the sensor. (b) Capacitance responses of the sensor at different frequencies. Note that the amplitude C_0 is only half of the peak-to-peak value (from Siebke et al. [84]).

of the SiO_2 layer imposes a strong tension on the membrane. The membrane bursts before or during the removal of the SiO_2. Therefore, only the layer thickness for the chip with the fixed electrode can be increased. Table 10 shows the resulting capacitances for a 1 µm thick Si_3N_4 layer and a 8 µm thick SiO_2 layer. The total capacitance of the 2 mm electrode is now sufficiently small. The capacitance of the 3 mm electrode is slightly above the maximum. By plugging in a large series capacitor between the sensor and the CDC, the capacitance but also the sensitivity are reduced below the maximum. When evaluating the experimental data, the series capacitor has to be accounted for.

6.2.3 Reducing the electrode diameter with respect to the membrane diameter

The third way to further minimize the parasitic capacitance is to reduce only the size of the electrodes whereas the size of the membrane stays constant. This results in sensors for which only the central area of the membrane is covered by the electrode (Figure 50(a)). The size of the electrode strongly influences C_2 and limits the total parasitic capacitance. In combination with the previously described thick insulation layer, membrane diameters of 4 mm and 5 mm can be used with electrode diameters of 2 mm and 3 mm, respectively. A small drawback due to the reduced electrode size is the smaller measuring capacitance, also leading to a reduced capacitance change upon deflection. Nevertheless, this effect is negligible as the central part of the membrane is further deflected than the border regions.

6.3 Analysis of experimental data

As explained in Section 5.3, the sensor is irradiated by a modulated IR source during the experimental characterization. To detect other IR sources, the incident radiation has to be chopped externally to provide a modulated signal (see Section 2.2.2). Figure 53(a) shows an example of a capacitance measurement at different modulation frequencies. Starting from the highest frequency, all modulation frequencies ranging from 1/16 Hz to 1 Hz are presented. The amplitude of the irradiance is constant for all frequencies. As expected, the response of the sensor increases with decreasing frequencies, i.e. increasing periods.

However, a drift of the response is also visible. This is due to the overall heating of the sensor as the mean irradiance is larger than zero.

To remove the drift and noise from the raw data of Figure 53(a), the data is digitally filtered. A digital filter can be defined by its impulse response, i.e. the response to the discrete delta function

$$\delta[j] = \begin{cases} 1, & (j = 0) \\ 0, & (j \neq 0). \end{cases} \tag{103}$$

Note that in this section, time and frequency are represented by discrete integer values j and k, denoted by square brackets []. For reasons of simplicity, the explicit conversion to actual time and frequency values is left out in this description. A digital filter can be applied by convolving the input signal $x[j]$ with the impulse response $h[j]$:

$$y[j] = (h * x)[j] \equiv \sum_{l=0}^{M} h[l]x[j-l], \tag{104}$$

where $y[j]$ is the filtered signal. In this case, the impulse response is also referred to as filter *kernel*. A commonly used digital low-pass filter is the windowed-sinc filter with a Blackman window (for more details about digital filters, please refer to e.g. [87]):

$$h_l[j \neq M/2] = K\frac{\sin(2\pi k_c(j - M/2))}{j - M/2}\left[0.42 - 0.5\cos\frac{2\pi j}{M} + 0.08\cos\frac{4\pi j}{M}\right], \tag{105}$$

$$h_l[j = M/2] = 2\pi k_c K, \tag{106}$$

where M is the *length* of the filter and k_c is the cut-off frequency. The filter consists of $M + 1$ samples from $j = 0$ to $j = M$. The bandwidth BW of this digital filter is the frequency range in which the response drops from 99 % to 1 % of the input signal. It is given by

$$BW = \frac{4}{M}. \tag{107}$$

Therefore, a larger filter can be used to remove more noise, as the cut-off frequency can be chosen closer to the modulation frequency without losing information. High-pass filters are generated from low-pass filters by *spectral inversion*:

$$h_h[j] = \begin{cases} -h_l[j], & (j \neq M/2) \\ -h_l[j] + 1, & (j = M/2). \end{cases} \tag{108}$$

A band-pass filter can be accomplished by the convolution of a low-pass and high-pass filter (with different cut-off frequencies):

$$h_b = h_l * h_h. \tag{109}$$

For each modulation frequency, such a band-pass filter is applied to the raw data. The cut-off frequencies of the high-pass and low-pass filters are chosen according to the length of the signal. Finally, to obtain the amplitude of a specific frequency, the corresponding component of the discrete Fourier transform (DFT) is calculated:

$$X[k] = \frac{1}{N}\sum_{j=0}^{N-1} x[j]\exp(-2\pi i jk/N), \tag{110}$$

#	d_e/mm	d_m/mm	t_m/nm	C_{tot}/pF
1	2	2	500	14.2
2	2	2	500	16.0
3	2	2	500	16.1
4	2	2	500	15.7
5	3	3	500	28.6
6	3	3	500	26.7
7	3	3	500	26.0
8	3	3	500	24.8
9	2	2	300	16.2
10	2	2	300	16.2
11	3	3	300	27.6
12	3	3	300	25.9
13	2	4	500	13.9
14	3	5	500	19.3

Table 11: Total base capacitance of the sensors, including parasitic capacitances. d_e: electrode diameter, d_m: membrane diameter, t_m: membrane thickness, C_{tot}: total capacitance.

where $X[k]$ is the amplitude of frequency k and N is the number of samples used to calculate the DFT. The resulting amplitudes of the different frequencies are shown in Figure 53(b). Due to the small number of samples used to generate this figure, the amplitudes have a certain ripple. Therefore, in the following experiments the number of samples that is recorded is much larger.

6.4 Results

In total, 14 sensors with different membrane and electrode diameter and membrane thickness were analyzed (Table 11). The obtained capacitances are in good accordance to the expected values (Table 10 for $t_{SiO_2} = 8\,\mu m$ and $t_{Si_3N_4} = 1\,\mu m$). Some capacitances are slightly below the predictions, which can be explained by the layer of glue. If it spreads beyond the trench, the glue enlarges the distance between the electrodes and decreases the capacitance. Sensors 13 and 14 are different from the other sensors as the electrode diameter is smaller than the membrane diameter to reduce the total capacitance (see Section 6.2.3).

During the first experiment, all sensors were operated at room temperature. This experiment provides a qualitative test of the functioning mechanism. To verify the predicted behaviour of the sensors, a second experiment was performed using different temperatures. It allows for the determination of the spring constants of the membranes and the comparison to simulated values.

6.4.1 Room temperature

Figure 54 shows the measured amplitudes for each sensor at room temperature (without additional heating or cooling). In Figure 55, identical sensors are subsumed, also showing the spread across each group. The only exception are sensors 13 and 14, which are the only ones of their kind.

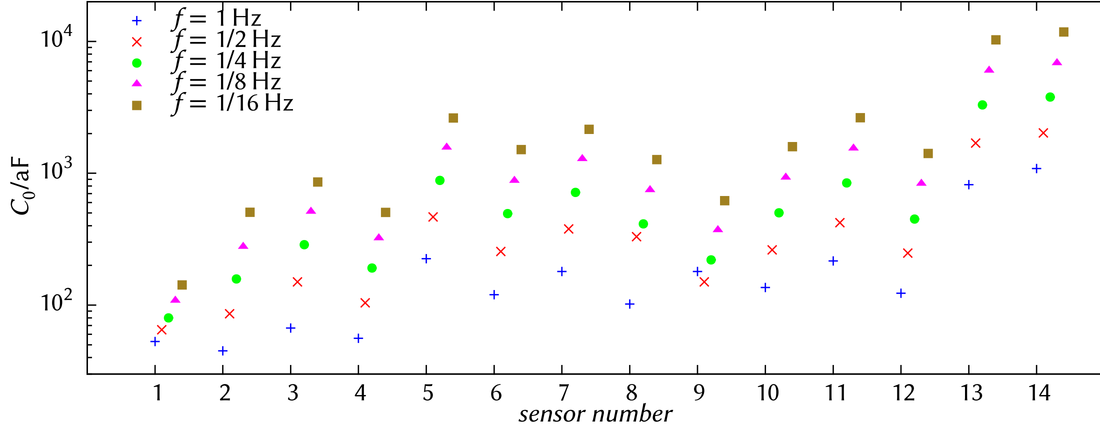

Figure 54: Amplitude $C_0(f)$ of the sensor response to a sinusoidal oscillation of the irradiance with an amplitude of $E_0 = 58\,\mathrm{W\,m^{-2}}$ at the frequency f (from Siebke et al. [84]).

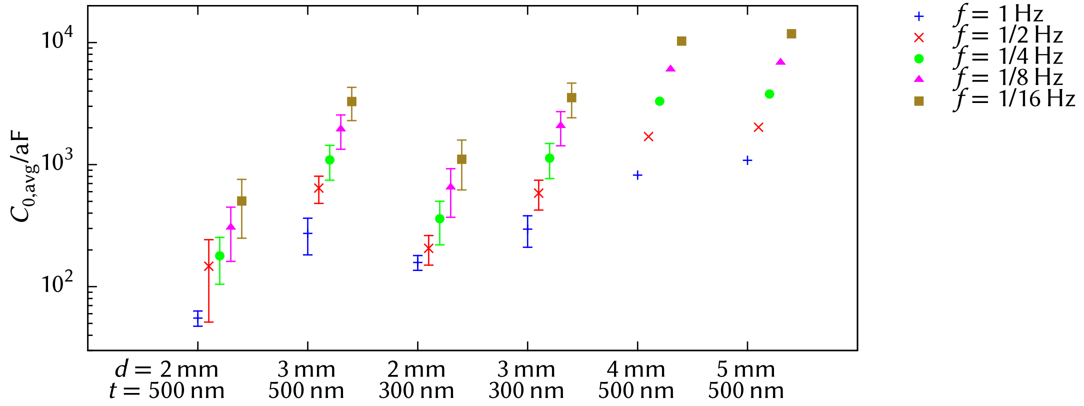

Figure 55: Averaged amplitude $C_{0,\mathrm{avg}}$ and spread for identical sensors. The first and second value on the x axis denote the membrane diameter and the membrane thickness, respectively. For all 2 mm and 3 mm membranes, the electrode has the same diameter as the membrane. For the 4 mm and 5 mm membranes, the electrode diameter is 2 mm and 3 mm, respectively. For these two, only a single sensor was tested, hence the spread could not be determined (from Siebke et al. [84]).

The sensors with the smallest membranes (2 mm diameter) and the 500 nm thick Si_3N_4 layer exhibit the smallest response (sensors 1 to 4). This result is expected for several reasons. First, the smaller and the thicker a membrane is, the stiffer it is. Second, the deflection of a small electrode induces a smaller change in capacitance than the same deflection of a large electrode. Due to the different area, the base capacitance $C_0 = \varepsilon_0 A/d$ of the small electrode is smaller and so is the change in capacitance ΔC. Third, the specific heat capacity of silicon is much higher as of air. As the silicon is removed below the membrane, a smaller membrane also implies a larger remaining volume of silicon and a larger total heat capacity. Therefore, the same amount of heat leads to a smaller change in temperature of the sensor and a smaller deflection of the membrane.

As expected, the sensors with the 3 mm membranes show a larger response than those with the 2 mm membranes. Yet, there is no significant difference between the sensors with the 500 nm thick Si_3N_4 layer and the 300 nm thick Si_3N_4 layer. At least for the 2 mm mem-

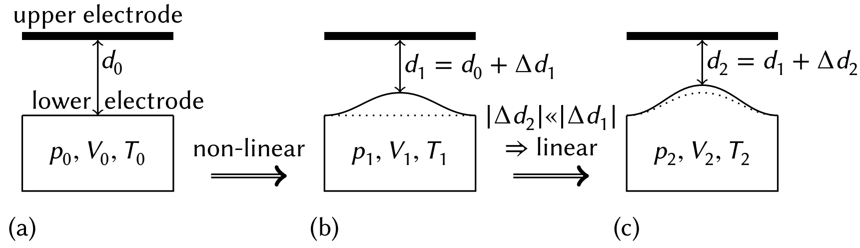

Figure 56: Temperature dependent deflection of the air-filled sensor. ΔT_1 is too large for a linear approximation of the capacitance. The superimposed temperature change ΔT_2 is sufficiently small for a linear approximation. Note that d_i is the mean deflection in the calculation.

brane, a small increase is visible that is not significant. However, the difference between the different thicknesses will become unambiguously visible in the next section.

Finally, the sensors with the largest (4 mm and 5 mm) membranes show the largest response. These sensors use 2 mm and 3 mm electrodes, respectively. Most probably, these particular sensors almost have the same response due to the manufacturing spread.

6.4.2 Verification of the expected deflection

As the sensor is filled with a gas, it is possible to determine the spring constant of the membrane. This in turn allows to verify the simulated membrane deflection. For this, the air in the pressure chamber is pivotal. If the sensors were filled with water, the determination of the spring constant would not be possible water is an incompressible of fluid. The determination of the spring constant starts with the initial capacitance of a plate capacitor (Figure 56(a)):

$$C_0 = \frac{\varepsilon_0 A}{d_0}, \tag{111}$$

where A is the area of the electrodes, d_0 the initial electrode distance, and $\varepsilon_0 = 8.85\,\mathrm{pF\,m^{-1}}$ the vacuum permittivity. As the pressure increases in the pressure chamber, the membrane is deflected towards the fixed electrode and the electrode distance decreases. The deflection Δd_1 of the membrane is described by the spring constant D:

$$\Delta d_1 = d_1 - d_0 = -\Delta p_1 \frac{A}{D}. \tag{112}$$

During the experiment, the sensor is heated from T_0 to $T_1 = T_0 + \Delta T_1$ by the Peltier heater (Figure 56(b)). The pressure difference can be calculated using the ideal gas law:

$$\frac{p_0 V_0}{T_0} = \frac{(p_0 + \Delta p_1)(V_0 + \Delta V_1)}{T_0 + \Delta T_1} \tag{113}$$

$$\overset{(112)}{\Rightarrow} (p_0 + \Delta p_1)(V_0 + \Delta p_1 \frac{A^2}{D}) = \frac{p_0 V_0}{T_0}(T_0 + \Delta T_1) \tag{114}$$

$$\Rightarrow p_0 \Delta p_1 \frac{A^2}{D} + \Delta p_1 V_0 + (\Delta p_1)^2 \frac{A^2}{D} = \frac{p_0 V_0}{T_0} \Delta T_1. \tag{115}$$

The term proportional to $(\Delta p_1)^2$ is neglected as $\Delta p_1/p_0 \simeq \Delta T_1/T_0 \ll 1$ ($V \simeq$ const.). Therefore,

$$p_0 \Delta p_1 \frac{A^2}{D} + \Delta p_1 V_0 \simeq \frac{p_0 V_0}{T_0} \Delta T_1 \tag{116}$$

$$\Rightarrow \Delta p_1 = \frac{p_0 V_0}{T_0(V_0 + p_0 A^2/D)} \Delta T_1 \tag{117}$$

$$\overset{(112)}{\Rightarrow} d_1 = -\Delta p_1 \frac{A}{D} + d_0 = -\frac{p_0 V_0 A}{T_0(V_0 D + p_0 A^2)} \Delta T_1 + d_0. \tag{118}$$

Due to the IR source, a small temperature change $\Delta T_2 = T_2 - T_1$ is superimposed (Figure 56(c)). For small changes of the electrode distance due to ΔT_2, the capacitance change is given by

$$\Delta C_2 \simeq -C_1 \frac{\Delta d_2}{d_1}, \tag{119}$$

where C_1 is the capacitance at temperature T_1 and $\Delta d_2 = d_2 - d_1$ is the change in distance due to ΔT_2. Using Equations (111) and (118),

$$\Delta C_2 = -\frac{\varepsilon_0 A}{d_1} \cdot \frac{\Delta d_2}{d_1} = -\frac{\varepsilon_0 A}{d_1^2} \Delta d_2 \tag{120}$$

$$= -\frac{\varepsilon_0 A}{\left(-\frac{p_0 V_0 A}{T_0(V_0 D + p_0 A^2)} \Delta T_1 + d_0\right)^2} \Delta d_2 \tag{121}$$

$$= -\frac{\varepsilon_0 A}{\left(-\frac{A}{T_0(D/p_0 + A^2/V_0)} \Delta T_1 + d_0\right)^2} \Delta d_2 \tag{122}$$

is obtained. Using Equation (118), Δd_2 can be rewritten to

$$\Delta d_2 = -\frac{p_1 V_1 A}{T_1(V_1 D + p_1 A^2)} \Delta T_2 \tag{123}$$

$$= -A \frac{p_1 V_1}{T_1} \cdot \frac{1}{(V_0 + \Delta V_1) D + (p_0 + \Delta p_1) A^2} \Delta T_2. \tag{124}$$

As $\Delta V_1 = \Delta p_1 \frac{A^2}{D}$,

$$\Delta d_2 = -A \frac{p_1 V_1}{T_1} \cdot \frac{1}{V_0 D + 2\Delta p_1 A^2 + p_0 A^2} \Delta T_2 \tag{125}$$

$$\overset{(117)}{=} -A \frac{p_0 V_0}{T_0} \cdot \frac{1}{V_0 D + \frac{2 p_0 V_0}{T_0(V_0/A^2 + p_0/D)} \Delta T_1 + p_0 A^2} \Delta T_2 \tag{126}$$

$$= -\frac{A}{\frac{D T_0}{p_0} + \frac{A^2 T_0}{V_0} + \frac{2}{V_0/A^2 + p_0/D} \Delta T_1} \Delta T_2. \tag{127}$$

Inserting into Equation (122) finally yields

$$\Delta C_2 = \frac{\varepsilon_0 A}{\left(-\frac{A}{T_0(V_0 D + p_0 A^2)} \Delta T_1 + d_0\right)^2} \cdot \frac{A}{\frac{D T_0}{p_0} + \frac{A^2 T_0}{V_0} + \frac{2}{V_0/A^2 + p_0/D} \Delta T_1} \Delta T_2 \tag{128}$$

$$= \frac{\varepsilon_0}{\left(-\frac{1}{T_0(D/p_0 + A^2/V_0)} \Delta T_1 + \frac{d_0}{A}\right)^2 \left(T_0 \left(\frac{D}{p_0} + \frac{A^2}{V_0}\right) + \frac{2}{V_0/A^2 + p_0/D} \Delta T_1\right)} \Delta T_2. \tag{129}$$

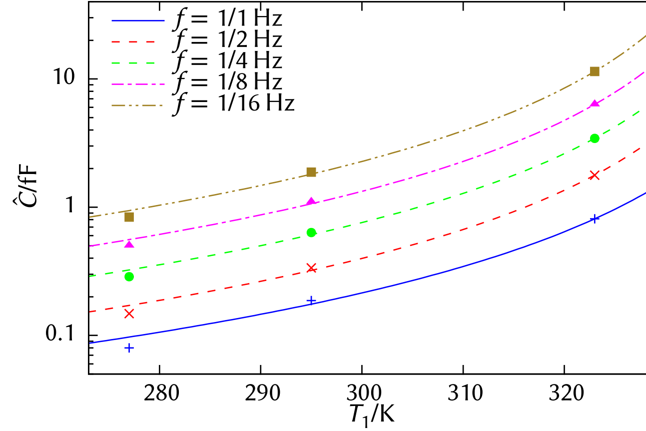

Figure 57: Amplitudes for different modulation frequencies at different temperatures for one sensor. The lines show the fit of Equation (129) (from Siebke et al. [84]).

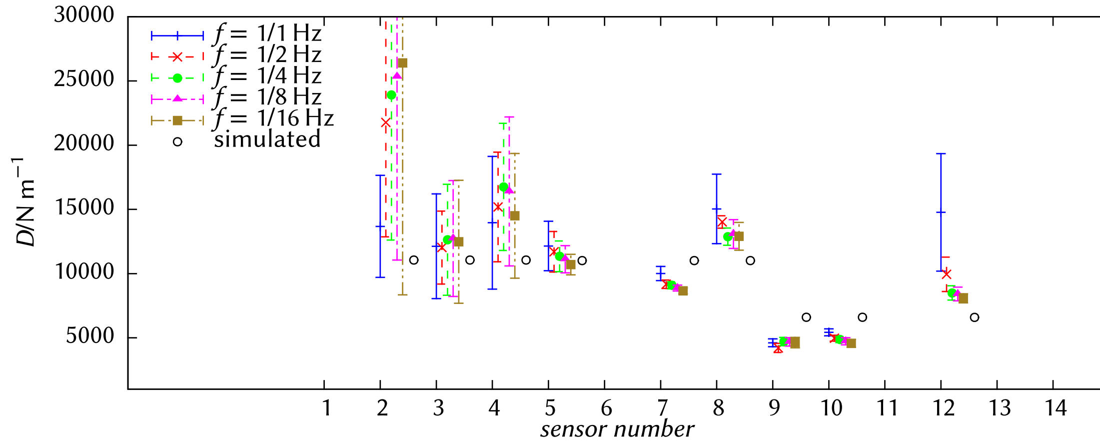

Figure 58: Spring constants calculated from Figure 57 for each frequency and the simulated value. The simulated value is independent of the frequency.

This formula depends on three temperatures. $T_0 = T_{\text{room}} = 295\,\text{K}$ is the initial temperature at which the sensor is assembled; $p_0 = 10^5\,\text{Pa}$ and $V_0 = At$ are the corresponding pressure and volume of the pressure chamber (height $t = 10\,\mu\text{m}$). After assembling, the sensor is heated to T_1 by the Peltier heater. At this temperature, the sensor is irradiated by the IR source, introducing the temperature change ΔT_2. ΔC_2 is the change in capacitance only due to ΔT_2. It depends on T_1 due to the pre-deflection of the membrane that changes the electrode distance. As the source is sinusoidally modulated, ΔC_2 and ΔT_2 are interpreted as the amplitude of the oscillation.

The response of the sensor is measured at three temperatures (4 °C, 22 °C, 50 °C) for five different modulation frequencies (1 Hz, 1/2 Hz, 1/4 Hz, 1/8 Hz, 1/16 Hz). The lowest temperature of 4 °C is accomplished by placing the experimental setup into a freezer, which is switched off during the measurement. To maintain a constant temperature, the sensor is heated to 4 °C during this measurement.[3] The measured amplitudes are shown in Figure 57 for one sample sensor. For each frequency, the measurements at three dif-

[3]These measurements were part of a bachelor thesis Thiesler [74].

ferent temperatures are shown. An increase of the temperature does reduce the electrode distance and enlarge the capacitance. The same IR signal leads to the same deflection independently of the temperature. Therefore, the change in capacitance and the sensitivity becomes larger for higher temperatures. This was also predicted by Equation (130). In Figure 57, the fit of Equation (130) to the experimental data with respect to the unknown temperature change ΔT_2 and the spring constant D for each frequency is presented. The spring constants for all tested sensors are shown in Figure 58. In addition to the fitted spring constants, Figure 58 also shows the simulated spring constants (black circle, see Section 3.3.1). In the simulation, the influence of the membrane diamter is small while the spring constant scales linearly with the membrane thickness. The errors are determined by the fit of Equation (130) to the experimental data. The results are in good accordance to the expected behaviour. The large errors, especially for sensors 2 to 4, arise probably due to the following: As stated above, the measurement at the lowest temperature was done in a freezer. Therefore, water might condense on the sensor and deteriorate the response. Especially the difference between thick membranes (500 nm, sensors 2 to 8) and thin membranes (300 nm, sensors 9 to 12) is clearly visible. Minor differences between experimental and simulated values can be explained by uncertainties in the Young's modules, the layer thickness, and the residual stress. These parameters strongly depend on the local gas mixture during the microtechnological deposition process. The gas mixture depends on the position of the wafer in the process chamber and on the position on the wafer. Taking these variations into account, the experimental values match the simulated values within the expected range.

Figure 57 shows a further reason for the need of the compensation mechanism. At different temperatures, the same radiation intensity lead to different amplitudes of the capacitance. Without the compensation mechanism, the capacitor membrane may already be deflected without external source due to the ambient temperature. As soon as the compensation mechanism is included, the sensor adapts itself to different temperatures. Then, the amplitude of the capacitance is independent of the temperature and does not require further corrections.

7 On the way to the μ-biomimetic sensor

In the previous chapters, different components of the μ-biomimetic IR sensor were presented. The response of the sensor including the compensation mechanism was theoretically described. The functioning of the fluidic compensation mechanism as well as the capacitive sensing were experimentally verified. Furthermore, a process for the bubble-free filling and the read-out electronics were shown. As all parts were proven to work as expected, the fabrication of the full-featured and small-scale sensor can be addressed now. The process flow for this sensor was presented in Chapter 4. While parts of this process are based on established procedures, the fabrication of the μ-capacitor represents a particular challenge.

The capacitor in the sensor strongly influences the sensitivity of the sensor. To detect the slightest pressure changes in the pressure chamber and thus the deflections of the membrane, the area of the electrodes has to be as large as possible and the electrode distance has to be as small as possible. A larger area and a smaller distance imply a larger base capacitance and therefore larger changes in capacitance. The influence of the electrode distance is even stronger: For a constant deflection, the relative distance change depends on the absolute distance. Therefore, the sensitivity of the capacitor to deflections increases roughly linearly with the area and with the inverse square of the distance.

Due to the large ratio of 1000 between the electrode diameter of 0.5 mm and the distance between the electrodes of 0.5 μm, the fabrication of the micro capacitor cannot be achieved reproducibly using the standard sacrificial layer process described in Chapter 4. This chapter covers the evaluation and further development of different procedures for the fabrication of this capacitor. Finally the first experimental characterization of a working μ-capacitor is shown. The successful fabrication constitutes the most important building block of the development of the complete μ-biomimetic sensor.[1]

7.1 Manufacturing of the μ-capacitors

To fabricate hollow structures as the air-filled capacitor of the μ-biomimetic sensor by means of micro systems technology, the use of *sacrificial layers* is inevitable. It is only possible to deposit new layers directly on top of other layers. Therefore, to fabricate the upper electrode of the capacitor with a certain distance to the lower electrode, an intermediate layer with a thickness equal to the anticipated distance has to be created as place holder. After the creation of the upper electrode, this sacrificial layer is removed to create a hollow structure. As the upper electrode, in contrast to the lower electrode, has to be rigid, it is made of a thick (5 μm) layer of gold.

[1] Parts of this chapter were published in Siebke et al. [11, 55, 61, 84].

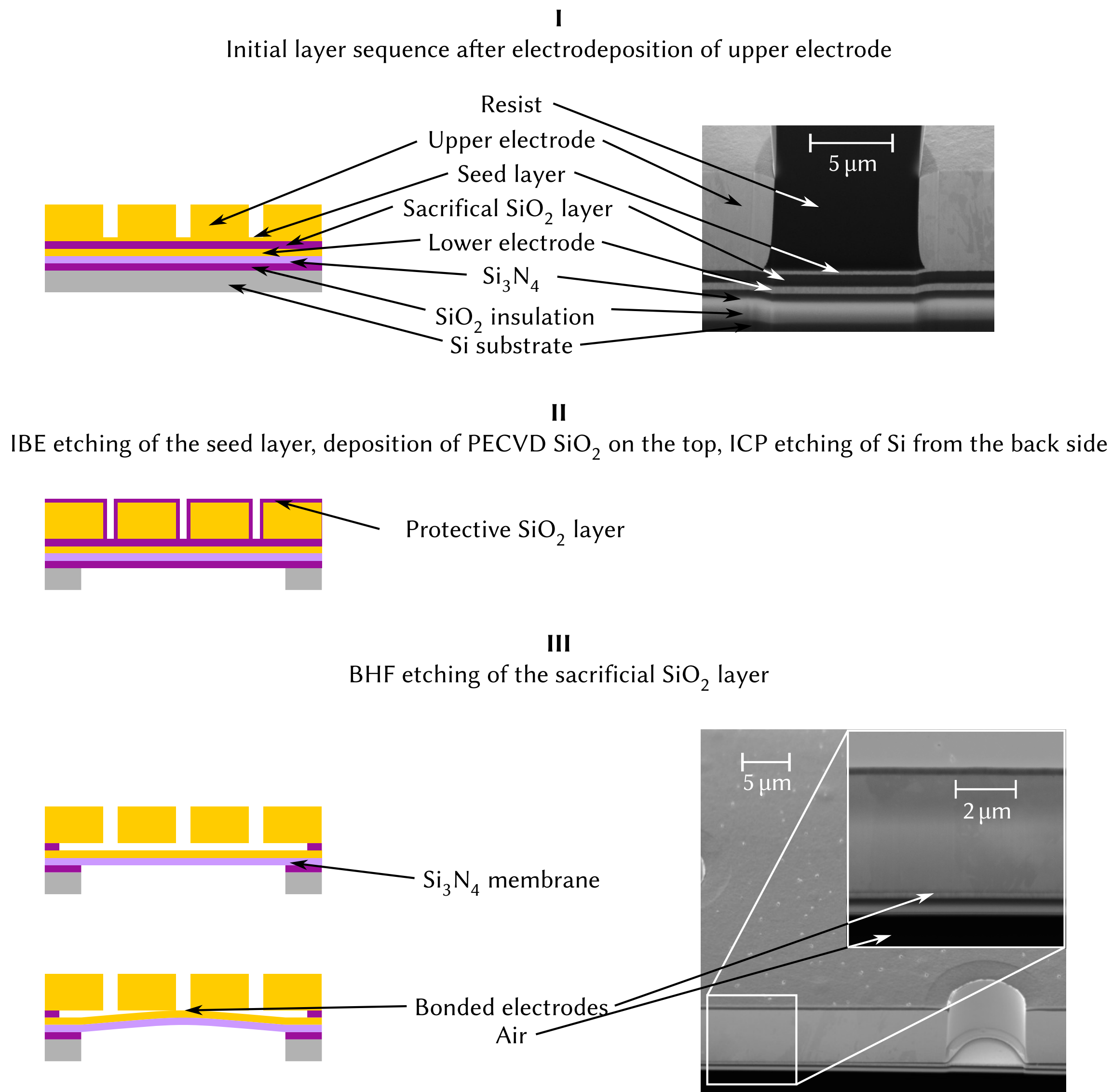

Figure 59: Micro-technological process flow of μ-capacitor using the standard process. Drawing not to scale (adapted from Siebke et al. [11, 61]).

Figure 59 I shows the layer sequence of the capacitor after the electrodeposition of the upper electrode. The thin seed layer is only needed for the latter process and is removed by means of IBE etching afterwards. Note that in the SEM (scanning electron microscope) image on the right, the resist, which defines the structure of the upper electrode, is still present. In the most simple design, the sacrificial layer is made of SiO_2. The deposition of this SiO_2 layer is well handled using a PECVD[2] process, while the isotropic removal, also in the space between the electrodes, is achieved by wet etching with buffered hydrofluoric acid (BHF). Prior to the removal of the sacrificial layer, another PECVD SiO_2 layer is deposited on the top of the wafer to protect the surface during the processing of the back side. Then the silicon substrate below the Si_3N_4 membrane is removed (Figure 59 II). Due to the structure of the pressure and compensation chamber, this step actually consists of many smaller steps (see Section 4.3).

[2]For a description of the processes, see Section 2.3.

After the back side processing, the wafer is immersed in BHF. The acid etches the SiO_2 layer below the membrane, the protective SiO_2 layer on top of the capacitor as well as the sacrificial layer (Figure 59 III). Finally the wafer is rinsed with water, displacing the etchant between the electrodes. However, upon drying, capillary forces draw the two electrodes together and the capacitor is destroyed, see Figure 59 III.

To minimize the capillary forces, the water between the electrodes could be removed using *critical point drying* (also referred to as *supercritical drying*). First, the water is replaced by acetone which is then replaced by liquid (high pressure) CO_2. A direct replacement of water by liquid CO_2 is not possible, as these two liquid to do mix with each other but both mix with acetone. Afterwards, pressure and temperature are increased beyond the critical point of CO_2. Now the pressure is reduced and the CO_2 will eventually enter the gas phase. In this way, the transition of liquid to gas is made without crossing the phase boundary. The gaseous CO_2 can leave the space between the electrodes without destroying the capacitor. While critical point drying might enable the use of the standard sacrificial layer process, most conforming machines are only able to handle small samples for biological research. A sufficiently large dryer was not available for the fabrication of the μ-biomimetic sensor. Instead, two proposed process changes were evaluated and further developed to finally yield functioning μ-capacitors without the need for critical point dryers.

7.1.1 Sacrificial a-Si layer process

Ultimately, the failing of the standard process is due to the use of a wet etchant to remove the sacrificial layer. A possible way out is to use a sacrificial layer that can be etched by an isotropic plasma enhanced process. Silicon seems to be a suitable candidate, as it can be etched isotropically using SF_6 gas in an ICP reactor. Therefore, the previously described process was modified to use a sacrificial layer made of silicon. Silicon is deposited by means of PECVD as amorphous silicon (a-Si) (Figure 60 I). As in the standard process, the silicon is removed from the back side while the capacitor is protected by an additional SiO_2 layer (Figure 60 II). This protective layer and the SiO_2 layer below the membrane are still removed by BHF (Figure 60 III). The sacrificial layer however is removed in the very end by means of isotropic ICP etching (Figure 60 IV). Two problems occurred during this last step. First, the plasma did not reach far enough between the electrodes to remove the complete layer as shown in Figure 60 III. The finite range could not be observed in pre-tests without the lower electrode. This is why the combination of the two electrodes might act as a shield for the plasma. While the exact reason is unclear, it can be easily circumvented by reducing the distance between the holes in the upper electrode. To accomplish this, a single photolithography mask was replaced by a modified version with a smaller hole distance.

However, further tests of the process with reduced hole distance revealed a more severe problem (Figure 61). The clean removal of the sacrificial a-Si layer as in Figure 60 III could not be reproduced. Instead, a porous structure remains after etching and prevents the removal of the complete layer. Such residuals could not be observed in Figure 60 III. An increase of the plasma power and longer etching times could not solve this problem. On the contrary, the plasma eventually attacked the gold surface of the electrodes. The residuals could have the following origin: The a-Si layer deposited by means of PECVD is not homogeneous. It shows instead a certain porosity increasing with the layer thickness. During the electrodeposition process, gold may enter into the hollow structure and produce the observed structure that cannot be removed later. It is unknown why the quality of the

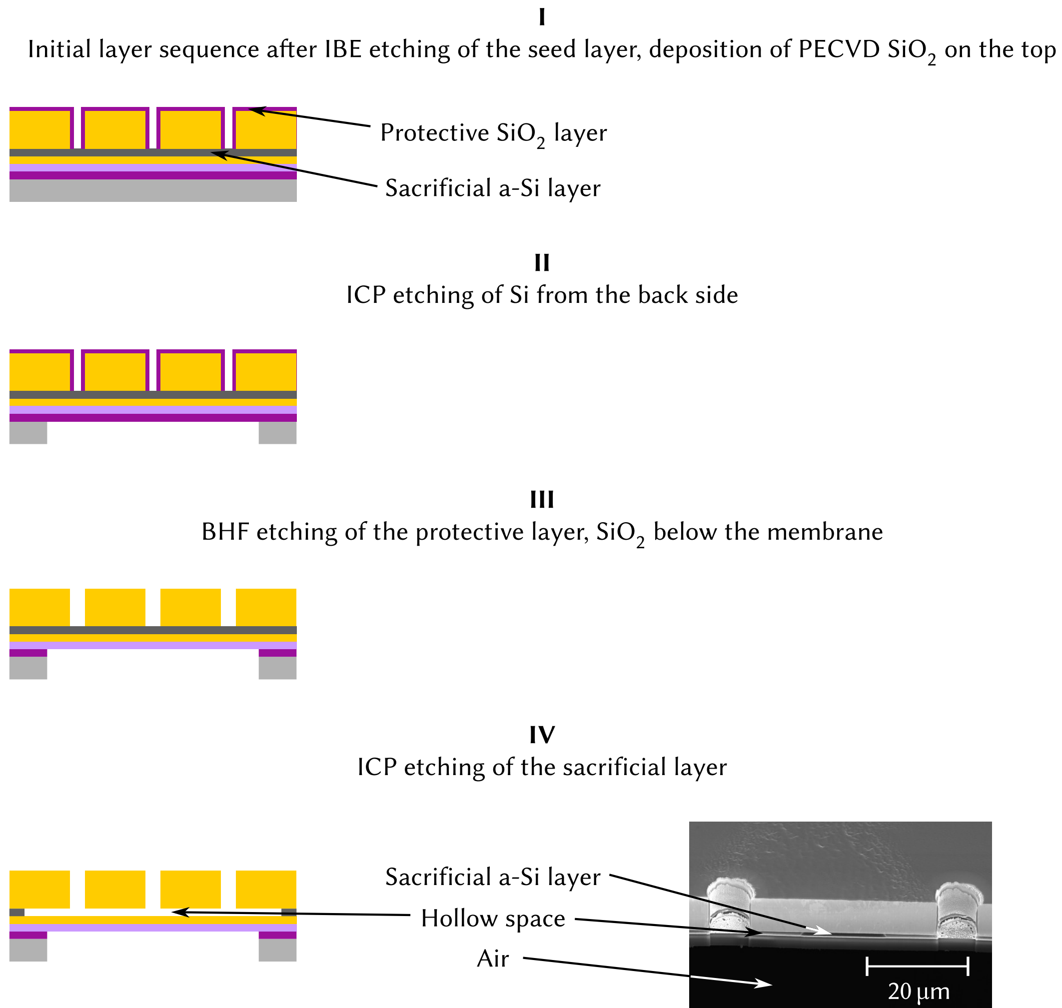

Figure 60: Micro-technological process flow of µ-capacitor using the sacrificial a-Si layer process. Drawing not to scale (adapted from Siebke et al. [11]).

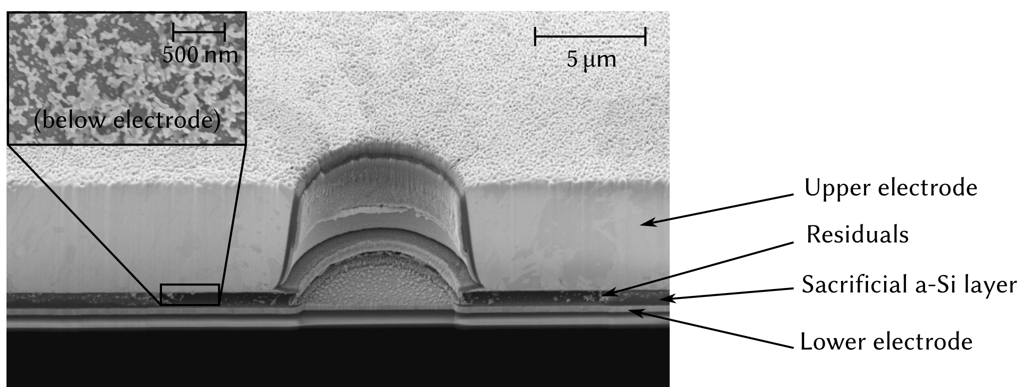

Figure 61: Residuals of the sacrificial layer after ICP etching.

layer varies between processes with the same parameters. In future tests, the formation of a porous gold structure could be prevented by introducing an additional SiO_2 layer on top the a-Si layer. Before the a-Si layer is removed in a plasma process, the SiO_2 would be

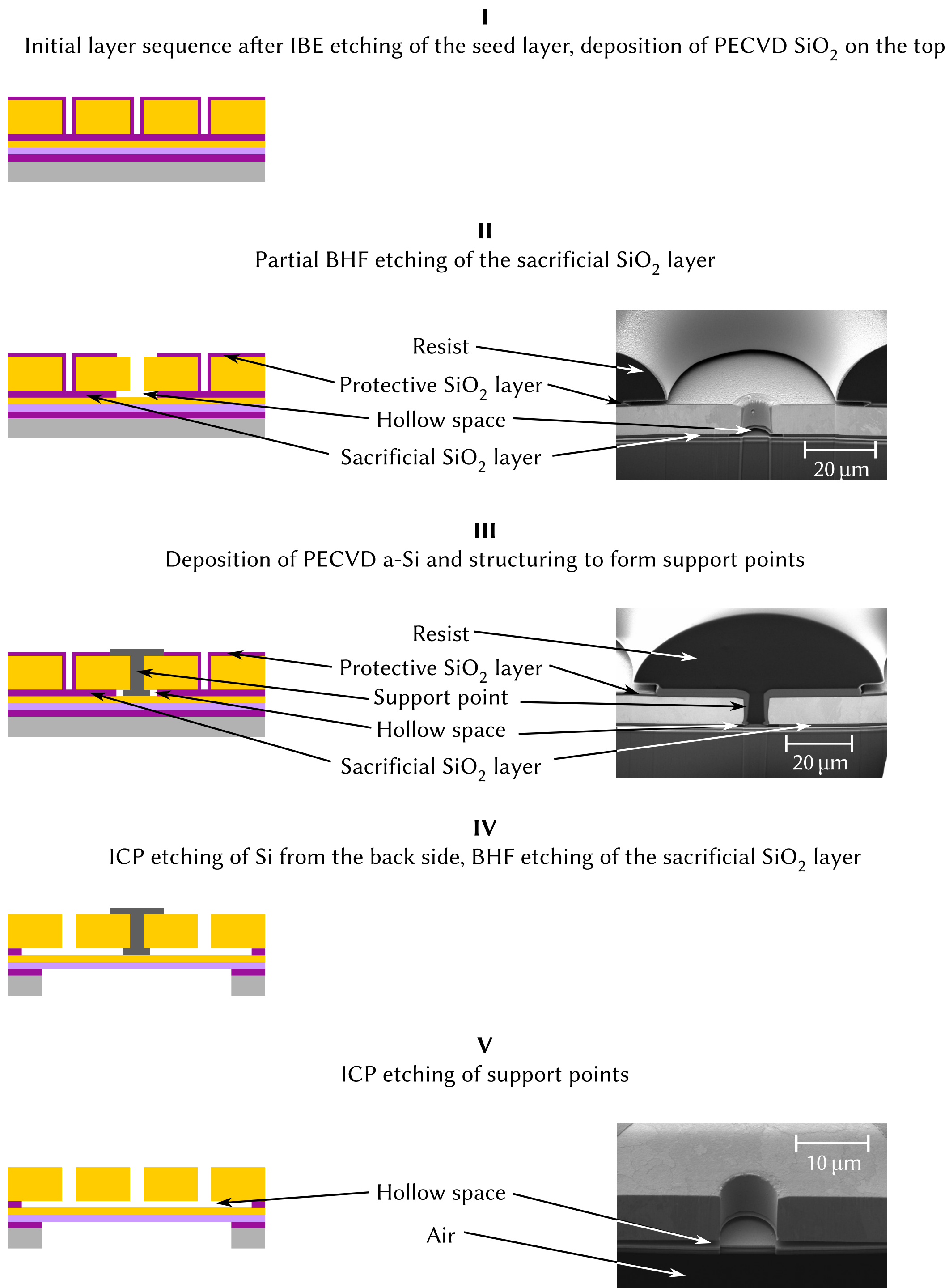

Figure 62: Micro-technological process flow of µ-capacitor using the support point process. Drawing not to scale (adapted from Siebke et al. [11]).

removed by means of BHF etching. Although the membrane might bend due to capillary forces, the removal of the a-Si layer would also release the membrane.

7.1.2 Support point process

Instead of using a sacrificial layer that is dry etched, the membrane is fixed during wet etching and drying in this process. The starting sequence is the same as for the standard

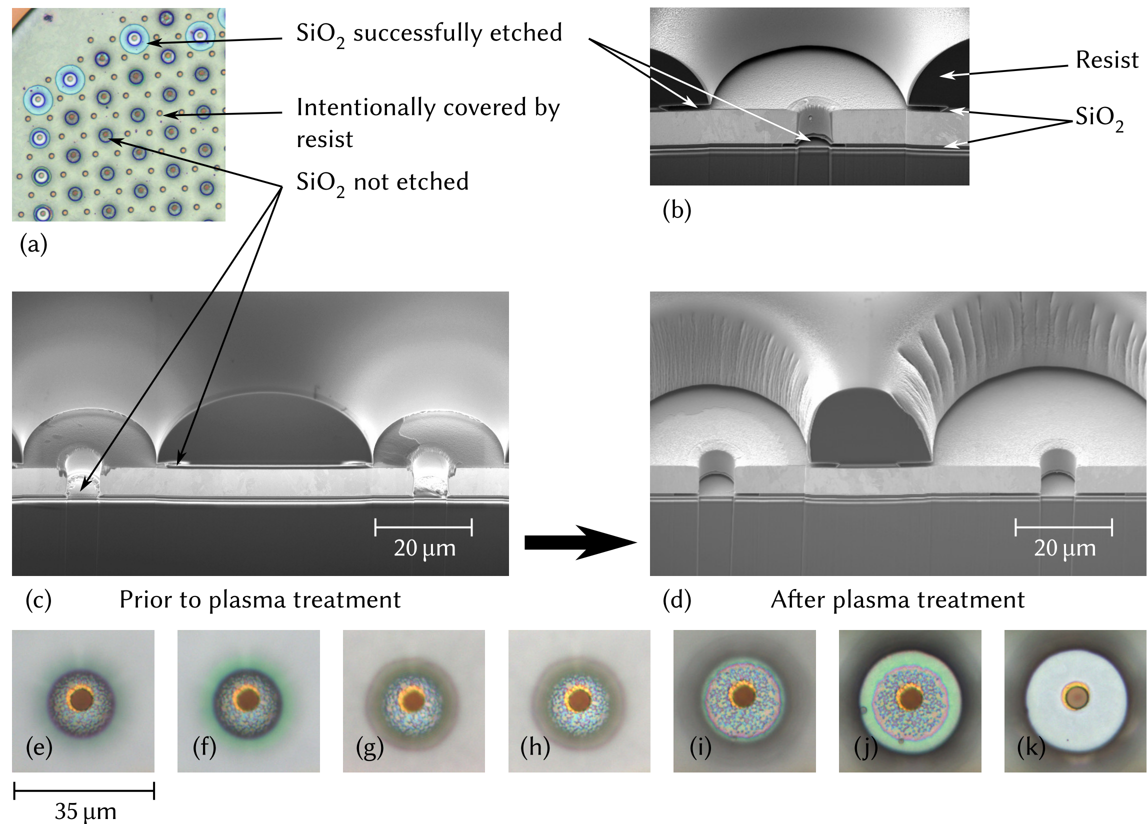

Figure 63: Residual resist preventing the BHF etching of the sacrificial layer.

process (Figure 62 I). In contrast to the standard process, the sacrificial layer is only etched partially using BHF (Figure 62 II). The rest of the layer is protected by photoresist. After stripping the photoresist, the wafer is covered with amorphous silicon (a-Si) in a PECVD process (the same as in the sacrificial a-Si layer process). The a-Si fills part of the empty space. The resulting support points ensure a minimum distance between the electrodes during wet etching of the sacrificial layer and drying (Figure 62 III). During the subsequent wet etching of the residual SiO_2 layer, the membrane is protected (Figure 62 IV). The last step is the dry etching of the support points using an isotropic ICP process (Figure 62 V). The corresponding SEM image shows a part of the capacitor where the sacrificial SiO_2 was successfully removed during the second BHF etching. But the small image is deceptive. In fact, only a small part of the sacrificial layer could be removed. During the second BHF etching, the etchant only enters a small number of holes in the electrode. Probably, the surface of the electrode is rendered hydrophobic during the plasma etch to structure the support points. In the subsequent second BHF etch, the surface is only badly wetted and therefore the yield is very low.

A similar problem also occurred during the first BHF etching. Nevertheless, the reason was a different one and was eventually solved. Figure 63(a) shows a top view of the capacitor after the first BHF process. Most of the holes are covered by photoresist to protect the sacrificial layer at this point. The upper electrode has a height of about 5 µm. Therefore, a sufficiently thick resist has to be used to ensure a complete coverage of the wafer. In the original process, a common choice, the AZ960 resist with a nominal thickness of about 10 µm, was used. But the development of the resist was quite erratic. At some positions, the resist is completely removed and the SiO_2 layer above and below the upper electrode

is etched as expected (Figure 63(b)). The removal of the protective SiO_2 layer above the electrode is also visible on the microscope image. Due to the removal of this layer below the resist, a second, larger circle emerges (light blue in the image). Yet at most positions, a small layer of resist remains after developing and prevents the etching of the SiO_2 layers (Figure 63(c)). This residual layer could not be prevented by increasing the development or exposition time. Instead, is was possible to remove this layer by means of plasma ashing in an O_2 plasma at a low rate. Figure 63(e) – (j) shows one of the initially blocked holes after several steps of plasma treatment. Finally the wafer was again immersed in BHF and the SiO_2 was successfully removed (Figure 63(k) and (d)). The only difference between Figure 63(b) and (d) is the different structure of the resist that was attacked by the oxygen plasma. To prevent the necessity of adding additional steps to the complete process, different alternative resists were tested. As a result, instead of the AZ9260, the AZ1518 with a thickness of about 5 μm is used now. Although this thickness is above the specified range, the resist can be developed as desired. Therefore, it is also used in further developments of the support points process as presented below.

7.1.3 Optimized support point process

The greatest difficulties of the support point process are encountered during the BHF etching. In the first etch step, this was solved by using a different resist. However, in the second etch step, the wafer surface hardly wets independent of the choice of resist. As this could not be circumvented by an additional O_2 plasma activation prior to the BHF etching, the complete process was modified. The new process again starts with the same layer sequence as the standard with a sacrificial SiO_2 layer (Figure 64 I). Instead of etching only a part of the sacrificial layer, the complete layer is removed in one BHF etching step (Figure 64 II). In contrast to the standard process, at this time, the silicon substrate is still present and prevents the membrane from bending. The upper electrode is sufficiently stable due to its thickness of about 5 μm. During the BHF etching, the protective SiO_2 layer is also removed from the capacitor surface. To restore the protection of the surface and to stabilize the membrane during the next steps, a layer of amorphous silicon (a-Si) is deposited. As in the previous process, the a-Si enters through the holes and forms support points that act as spacers between the two electrodes (Figure 64 III). Then the silicon and the SiO_2 layer below the membrane are removed (Figure 64 IV). As the etching rate of SiO_2 and Si_3N_4 during plasma etching is similar, the SiO_2 layer has to be removed by means of wet etching using BHF. At this point the presence of the support points is pivotal. Without them, the BHF would enter the space between the two electrodes. During drying, capillary forces would pull the electrodes together. The support points and the a-Si layer prevent the sticking and protect the capacitor during the remaining process steps. The a-Si layer is removed at the very end using an isotropic ICP process (Figure 64 V).

Using this optimized support point process, it was possible for the first time, to fabricate functioning μ-capacitors with an aspect ration of 1000. In addition, the number of BHF etch steps is reduced by one and two less photolithography masks are used during the fabrication in contrast to the original support point process.

7.2 The first sensors based on the μ-capacitor

By employing the modified support point presented in the last section, it was possible to fabricate the first μ-capacitors. However, during the development of the process, the complete process flow was reduced to the fabrication of only the capacitor. Therefore, only the

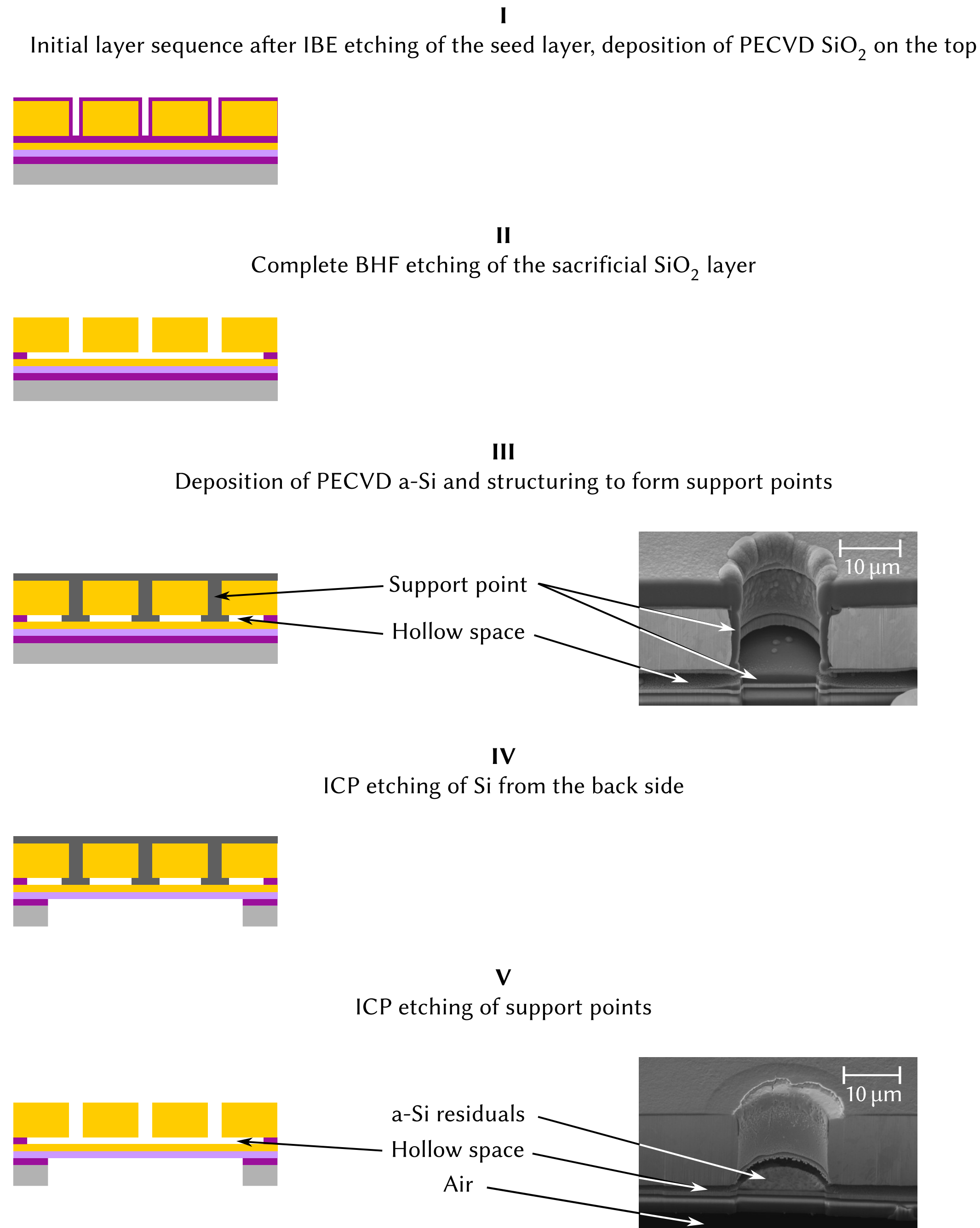

Figure 64: Micro-technological process flow of μ-capacitor using the modified support point process. Drawing no to scale (adapted from Siebke et al. [55, 61]).

second wafer with the capacitor was produced and features necessary for the compensation mechanism were left out. Yet, it was possible to obtain working sensors using these capacitors.

To obtain IR sensors, a pressure chamber had to be formed. This was achieved by glueing the wafer containing the capacitors on a glass wafer. The glass wafer is coated with a 50 μm thin layer of PDMS that is cured at room temperature after the Si-wafer is attached. By this sealing of the pressure chamber below the capacitor, first air-filled prototypes were obtained (Figure 65). To prevent the membrane from being deflected towards the upper electrode during the assembly, the wafer with the capacitors was preheated to 50 °C. Upon

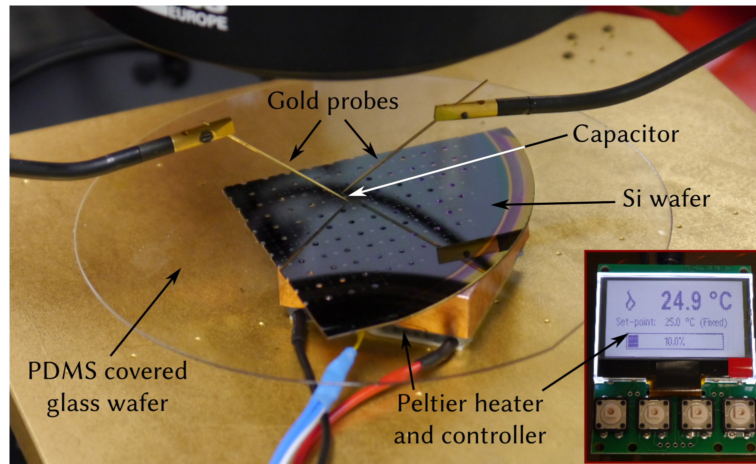

Figure 65: µ-capacitors on a point probe station. The Si wafer is glued on a glass wafer to form a pressure chamber. The two gold coated probes contact a single capacitor. The assembly is heated by means of the Peltier heater below the wafer.

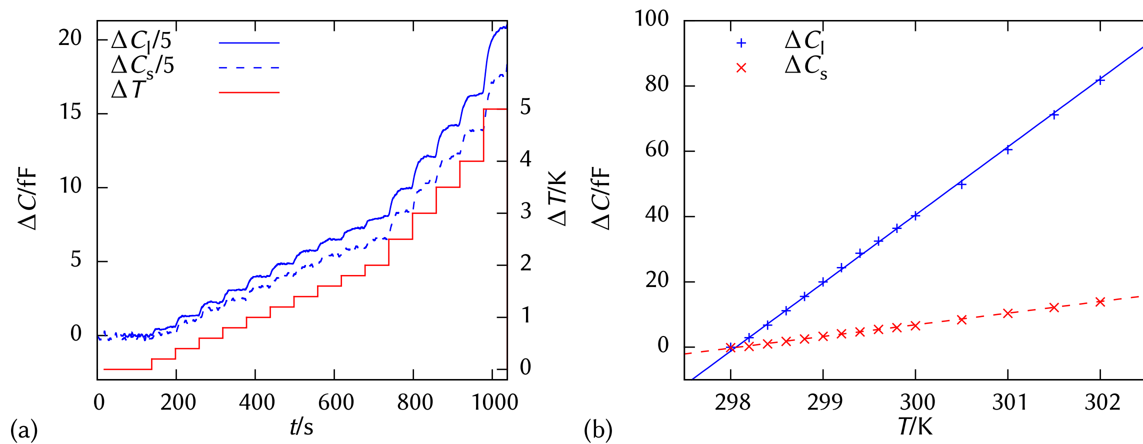

Figure 66: Measurement of the change in capacitance ΔC depending on the chip temperature T. (a) During the measurement of the capacitance, the temperature was stepwise increased. $\Delta C \equiv 0$ for $T = 298\,\text{K}$. (b) For each temperature, the mean capacitance is extracted. The solid line shows the fit of (130) (adapted from Siebke et al. [55]).

cooling to room temperature, the membrane is pulled away from the upper electrode. Note, that these sensors do not feature the compensation mechanism.

For a function test, the sensor was heated using a similar Peltier heater as for the simplified sensor (Figure 65, see Section 5.3). The change in capacitance was measured using the electronics presented in Section 5.1. However, this time the CDC could not be placed near the capacitor as it is still contained on a wafer. Instead, the electrodes are contacted on a point probe station, which is connected to the electronics board that includes the CDC. Figure 66(a) shows the results for two µ-capacitors with different membrane diameters ($d_l = 500\,\text{nm}$ and $d_s = 300\,\text{nm}$). The dotted red line shows the target temperature. The actual temperature of the heater and the sensor is established with a delay. Therefore, the slope of the capacitance in Figure 66(a) does not reflect the speed of the sensor but the speed of the heater. The larger sensor can already resolve temperature differences of about 0.01 K, the smaller one of about 0.05 K.

d/mm	D_{exp}/N m^{-1}	D_{sim}/N m^{-1}
0.3	12 754 ± 49	12 189
0.5	12 506 ± 33	11 545

Table 12: Diameter, experimental and simulated values of the spring constant of the μ-capacitor.

Due to the gas inside the sensor, it is possible to determine the spring constant of the membranes. This is similar to the procedure used for the simplified sensor (see Section 6.4). However, due to the smaller diameter of the membrane, Equation (129) can be simplified to

$$\Delta C_2 = \frac{\varepsilon_0 A^2 p_0}{\left(p_0 \frac{A}{D}\left(1 - \frac{T_1}{T_0}\right) + d_0\right)^2 D T_0} \Delta T_2. \tag{130}$$

Here, $T_0 = 232\,\text{K}$ and $p_0 = 10^5\,\text{Pa}$ are the temperature and the pressure at which the sensor was assembled and $T_1 = 295\,\text{K}$ is the room temperature. $\Delta T_2 = T_2 - T_1$ is the difference of the current temperature to room temperature.

Figure 66(b) shows the resulting dependence of the capacitance to the temperature. The solid line shows the fit of Equation (130) to the experimental data. The sensor exhibits a linear behaviour in this range as expected. The resulting spring constants including the error of the fit and the simulated values (see Section 3.3.1) are shown in Table 12. The experimental values only differ very slightly from the expected values. The errors of the fitted spring constants are even smaller because they do not include process inhomogeneities that change e.g. the Young's modulus. Furthermore, such measurements can be used for sensor calibration: By measuring the capacitance, the temperature can be inferred.

8 Conclusion and outlook

In this work, the development of a biomimetic uncooled IR sensor based on the IR receptors of *Melanophila acuminata* was presented. Starting from the biological model, a sensor design was developed, including a model description and readout electronics. Figure 67 shows an overview of topics pivotal for the sensor development that were addressed in this work. Text coloured in green denotes completed tasks whereas the yellow text denotes tasks requiring further work. In the following, the results of the individual chapters and of the complete thesis will be discussed.

In Chapter 2, the IR receptors of the beetle *Melanophila acuminata* were presented. An overview of the different sensitivity measurements in the literature revealed a large discrepancy. The difference between behavioural and electrophysiological measurements could be explained by the large number of receptors in one organ and the inherently different definitions of the sensitivity. However, the estimation based on the distance that beetles have travelled to seek fires is incompatible to these results. To end the decade long discussion, a model of the sensillum was developed in this work, able to reproduce the values of the electrophysiological measurements. It is based on a simplified geometry of the receptor, material properties and biological limits of sensation. It does not rely on the

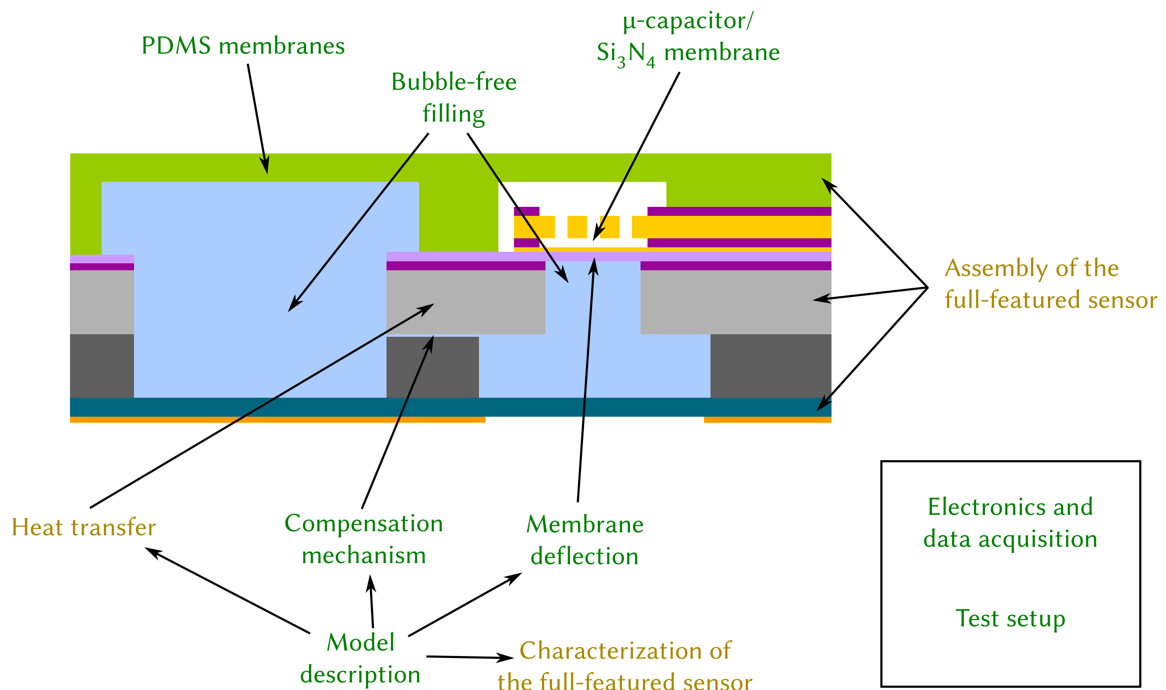

Figure 67: Components of the µ-biomimetic sensor. Green text denotes successfully implemented components. Yellow text denotes components that await experimental verification.

experimental determination of the sensitivity. The fact that the behavioural and electrophysiological experiments as well as the model yield compatible values is a strong hint that the obtained sensitivity is actually the true sensitivity of the beetle's receptor. A technical sensor based on the IR receptors – as presented in this work – will help to solve the decade-long discussion about the sensitivity and the anticipated detection mechanism.

The transfer of the beetle's receptor to a general concept for IR sensors was described in Chapter 3. Based on this, a theoretical model for such sensors was derived. For the first time ever, this model describes the thermal and fluidic behaviour and predicts the modulation frequency dependent membrane deflection. The model especially allows to calculate the filter properties of the compensation mechanism. A dedicated experimental verification of the fluidic filter mechanism was able to validate the model prediction as well as the simulation of the PDMS membranes. For this experiment, silicon chips were produced featuring a pressure and a compensation chamber connected by the compensation channel. An additional chamber was used to emulate the thermal expansion of the liquid inside the system. The experiment allowed to determine the spring constants of the membranes, coinciding with the simulated values. The model proved suitable to adapt the sensor concept to actual technical sensors.

To build a small sensor suitable for mass production, micro system technology is used. Chapter 4 presented the design of a sensor with an surface area of $4\,\mathrm{mm} \times 4\,\mathrm{mm}$ and a thickness of 1 mm made of silicon, glass, and PDMS. On the one hand, the design was optimized for feasibility, on the other hand, some parameters were optimized for high sensitivity using the model presented in the previous chapter. Instead of the dendrite, the biomimetic sensor uses a plate capacitor for the readout. One electrode of the capacitor is located on a silicon nitride membrane that is in contact to the liquid inside the pressure chamber. The other electrode is fixed. To achieve a high sensitivity, the ratio of the capacitor diameter to the electrode distance is 1000. Therefore, even the slightest deflection below 1 nm can be detected. The compensation chamber is sealed by a PDMS membrane, similar to the membranes used in the test of the fluidic filter. The behaviour of both the PDMS and the Si_3N_4 membrane is simulated. In addition to the micro technological process, the bubble-free filling with water and the final assembly were presented in this chapter. Especially bubble-free filling of micro cavities with water was a general problem in micro fluidics that was solved here.

The electrode distance is very small compared to the diameter; still the expected changes in capacitance are minute. In Chapter 5, a tailored electronic setup was presented that is able to measure changes below a femtofarad (1×10^{-15} F). Here, the electronic circuit was connected to a computer with a custom-build data recording and analysis software. The software controls the parameters of the CDC and is able to carry out frequency analysis. Finally a test setup for IR sensors was presented. Instead of a slow black-body radiator, semiconductor IR emitters that can be electronically modulated were used. The sensor was placed in an air-tight metal box with a transmissive window. The box is equipped with a precise heater to conduct measurements at different temperatures. The components developed in this chapter provide the necessary tools to characterize the IR sensors presented in the next chapters.

To facilitate the analysis of the influence of several parameters on the sensitivity and to validate the simulation of the Si_3N_4 membrane, a simplified sensor was presented in Chapter 6. This sensor is larger than the previously shown one and does not feature the compensation mechanism, yet it is based on the same detection mechanism. However, it is less prone to errors and can be built faster. Therefore, sensors with various membrane

diameters and thicknesses were analyzed. As these sensors were air-filled, the measurements could be used to verify the simulation of the Si_3N_4 membrane deflection and thus the spring constants. The knowledge about the membranes was used to predict the according behaviour of the membranes of the capacitor of the technical sensor – the μ-biomimetic sensor.

In the last chapter, Chapter 7, it is described how the μ-biomimetic sensor can be realized. This chapter focusses on the fabrication of the capacitor. Due to the large aspect ratio of 1000, the standard sacrificial layer process could not be employed. Instead, different other processes were evaluated and further developed. Finally it was possible to fabricate working μ-capacitors. It was shown that the sensor prototypes work exactly as predicted by employing a similar technique as for the simplified sensor.

In this work, the proof of the sensor concept as well as the proof of the feasibility of an according μ-biomimetic sensor were made. This work establishes the foundation for microtechnological sensors based on the IR receptors of *Melanophila acuminata*. Future works have to continue on the paved way to complete the μ-biomimetic sensor. The complete sensor will allow the validation of the predicted sensitivity. Furthermore, the thermal part of the model as well as the interaction of the thermal and fluidic parts can validated.

This work focused on the development of a sensor prototype. Therefore, the sensitivity of the implemented sensor design was a compromise between sensitivity and feasibility. However, it includes the fluidic compensation mechanism, enabling the sensor to withstand large temperature fluctuations without a loss of linearity. Based on the completed sensor, the developed processes, and the model, an improved design with increased sensitivity can be derived. A further miniaturization of the sensor will maximize the sensitivity and enable the fabrication of sensor arrays for image sensors.

Several novel processes and components were developed as part of the μ-biomimetic IR sensor. Moreover, these developments will have an impact beyond the sensor presented here. Bubble-free filling is a general problem in microfluidics that was solved here. Air-filled μ-capacitors with an aspect ration of 1000 can improve other sensors like pressure or temperature sensors. The compensation mechanism can be employed in all fluidic systems that suffer from large pressure fluctuations. Finally, the sensor and the model description will help to end the discussion about the detection mechanism and the sensitivity of the beetle.

A Flowcharts

This appendix contains the flowcharts used throughout this work. Only the most recent versions are shown, including all developments and improvements presented here.

μ-biomimetic sensor

This flowchart is divided into two parts. The first part is common to all methods for the fabrication of the μ-capacitor ("Basis"). The second part includes the remaining steps, adapted to the μ-capacitor. Here, only the successful modified support point process is shown ("Stützstellen V2"). For a detailed description, see Sections 4.3 and 7.1.

Flowchart ID-Nr.: **228-2014-05 IR-Sensor komplett - Basis**

FC- Betreuer: **Georg Siebke** Projekt: **Bionischer IR-Sensor**

Projektname: Bionischer IR-Sensor	**Projektgruppe/ Konto-Nr.: 50601**	**Flowchart- Betreuer: Georg Siebke**
Substrat-Art: Si-Wafer / DSP / 300μm	**Anzahl Substrate: 2×10**	

Nr.	**Prozess-Schritt:**	**Prozessseite**	**Prozess Parameter / Prozess Nummer**	**Ergebnisse / Bemerkung**	**Bearbeiter /Datum**
1	**Losgründung**		Wafername: Material: **Si / DSP / 4" / 300μm** Vorbehandlung: **keine**		
2	**Lithografie Schutzlack**	Wafer 2 Vorderseite	Prozessname: **AZ1518/~2,2μm** Maskenname: Justagemarke (Nr.): **keine** Substratoberfläche: **Si** Topologie: Bemerkung: **Schutzlack vor Lithographie Nr. 1 aufbringen um Oberfläche für Bonden zu schützen**	**Prozess ID:** Belacken: **HMDS 100°C/10s** **1,5ml AZ1518** **Prog.: AZ1518_M1** **SB: HP 100°C / 1min** Belichten: Entwickeln: Hartbake: Bemerkung:	
3	**Lithografie Nr. 1**	Wafer 2 Rückseite	Prozessname: **AZ1518/~2,2μm** Maskenname: **Maske 01 Justage-Marken V03** Justagemarke (Nr.): **1** Substratoberfläche: **Si** Topologie: **keine** Bemerkung: **Justagemarken Klemmchuck benutzen**	**Prozess ID:** Belacken: **HMDS 100°C/10s** **1,5ml AZ1518** **Prog.: AZ1518_M1** **SB: Umluft 100°C/30min** Belichten: **60mJ/cm2** **Vac. Cont.** **WEC: Spacer** Entwickeln: **AZ726/30s** Hartbake: **Umluftofen 120°C/30min** Bemerkung: **HMDS der Maske**	

caesar

Flowchart ID-Nr.: **228-2014-05 IR-Sensor komplett - Basis**

FC- Betreuer: **Georg Siebke** Projekt: **Bionischer IR-Sensor**

Nr.	Prozess-Schritt:	Prozessseite	Prozess Parameter / Prozess Nummer	Ergebnisse / Bemerkung	Bearbeiter /Datum
4	**Ätzen** Trockenätzen ICP	Wafer 2 Rückseite	Ätztiefe Silizium: **200nm** Ätzstopp: **keiner** Bemerkung: **Justagemarken**	**Prozess ID:** **Bemerkung:**	
5	**Ablacken** Nass (NMP, Aceton, IPA)	Wafer 2 Vorderseite Rückseite	Lack: **AZ1518** Lackdicke: **~2,2µm** Max. Ultraschall: **140%** Bemerkung: **frisches Aceton und IPA verwenden**	**Prozess ID:** **Bemerkung:**	
6	**Lithografie Nr. 2**	Wafer 2 Vorderseite	Prozessname: **AZ1518/~2,2µm** Maskenname: **Maske 02 Kapillare V03** Justagemarke (Nr.): **2 auf 1** Substratoberfläche: **Si** Topologie: **keine** Bemerkung: **Ausgleichskanal**	**Prozess ID:** Belacken: **HMDS 100°C/10s** **1,5ml AZ1518** **Prog.: AZ1518_M1** **SB: HP 100°C/1min** Belichten: **60mJ/cm2** **Vac. Cont.** **WEC: Spacer** Entwickeln: **AZ726/30s** Hartbake: **Umluftofen 120°C/30min** Bemerkung: **HMDS der Maske**	
7	**Ätzen** Trockenätzen ICP	Wafer 2 Vorderseite	Ätztiefe Silizium: **5 µm** Ätzstopp: **keiner** Bemerkung: **fein**	**Prozess ID:** **Bemerkung:**	
8	**Ablacken** Nass (NMP, Aceton, IPA)	Wafer 2 Vorderseite Rückseite	Lack: **AZ1518** Lackdicke: **~2,2µm** Max. Ultraschall: **140%** Bemerkung: **frisches Aceton und IPA verwenden**	**Prozess ID:** **Bemerkung:**	-

2 von 6

caesar

Flowchart ID-Nr.: **228-2014-05 IR-Sensor komplett - Basis**

FC- Betreuer: **Georg Siebke** Projekt: **Bionischer IR-Sensor**

Nr.	Prozess-Schritt:	Prozessseite	Prozess Parameter / Prozess Nummer	Ergebnisse / Bemerkung	Bearbeiter /Datum
9	**Kontrolle** Topologie Messung	Wafer 2 Vorderseite	**FRT - Weißlichtinterferometer**	**Prozess ID:** **Bemerkung:**	
10a	**Vorbehandlung Bonden** Aktivieren Nasschemisch	Wafer 1 Vorderseite Rückseite Wafer 2 Vorderseite Rückseite	Lösung: **H2SO4:H2O2=4:1; 10min; RT** **NH4OH:H2O2:H2O=1:1:5; 10min; 75°C** **NH4OH:H2O2:H2O=1:1:6; 10min; 75°C** Zeit: Bemerkung: **Separate Anleitung beachten! (Sören Becker)**	**Prozess ID:** **Bemerkung:**	
10b	**Bonden**	Wafer 1 Rückseite Wafer 2 Vorderseite	**Fusion Bonden** Justage: **grob** Druck: **10-4mbar** Temperatur: **450°C** Zeit: **1h** Bemerkung: **Separate Anleitung beachten!**	**Prozess ID:** **Bemerkung:**	

3 von 6

caesar

Flowchart ID-Nr.: **228-2014-05 IR-Sensor komplett - Basis**

FC- Betreuer: **Georg Siebke** Projekt: **Bionischer IR-Sensor**

Nr.	Prozess-Schritt:	Prozessseite	Prozess Parameter / Prozess Nummer	Ergebnisse / Bemerkung	Bearbeiter /Datum
11a	**Annealing** Oxidationsofen	Wafer1/2 Vorderseite Rückseite	**Rezept: bond1000.rcp** **Bei 1075°C 1:30 h unter Stickstoffatmosphäre tempern. Anschließend mit der Oxidation beginnen (nächster Schritt)** **Separate Anleitung beachten!**	**Prozess ID:** **Prozessparameter:** **Tube:** **Temperatur:** **Zeit:** **Bemerkung:**	
11b	**Beschichtung** Thermische Oxidation	Wafer1/2 Vorderseite Rückseite	Schicht: **SiO2 Feucht** Schichtdicke: **0,5µm** Bemerkung:	**Prozess ID:** **Prozessparameter:** **Tube:** **Temperatur:** **Zeit:** **Bemerkung:**	
12	**Beschichtung** LPCVD	Vorderseite Rückseite	Schicht: **Si_3N_4** Schichtdicke: **0,5µm** Bemerkung: **Schicht mit Zugspannung Membran** **+ Testwafer für Spannungsmessung**	**Prozess ID:** **Prozessparameter:** Tube: Temperatur: Zeit: Bemerkung:	
13	**Beschichtung** PECVD	Rückseite	Schicht: **SiO_2** Schichtdicke: **1 µm** Prozessparameter: Bemerkung: **Kratzschutz**	**Prozess ID:** **Prozessparameter:** Zeit: Leistung: Druck: Bemerkung:	

caesar

Flowchart ID-Nr.: **228-2014-05 IR-Sensor komplett - Basis**

FC- Betreuer: **Georg Siebke** Projekt: **Bionischer IR-Sensor**

Nr.	Prozess-Schritt:	Prozessseite	Prozess Parameter / Prozess Nummer	Ergebnisse / Bemerkung	Bearbeiter /Datum
14	**Beschichtung** Sputtern Unaxis	Vorderseite	Schicht: **Cr/Au/Cr** Schichtdicke: **10/200/10nm** Haftschicht/-dicke: **Cr/10nm** Sputteretch: **ja** Bemerkung:	**Prozess ID:** **Prozessparameter:** Zeit: Leistung: Druck / Gasfluss: Osz. / Rot.: Bemerkung:	
15	**Lithografie Nr. 3**	Vorderseite	Prozessname: **AZ1518/~2,2µm** Maskenname: **Maske 03 Untere Elektrode V03** Justagemarke (Nr.): **3 auf 1** Substratoberfläche: **Cr** Topologie: **keine** Bemerkung: **Elektrode**	**Prozess ID:** Belacken: **HMDS 100°C/10s 1,5ml AZ1518 Prog.: AZ1518_M1 SB: HP 100°C/1min** Belichten: **60mJ/cm2 Vac. Cont. WEC: Spacer** Entwickeln: **AZ726/30s** Hartbake: **Umluftofen 120°C/30min** Bemerkung: **HMDS der Maske**	
16	**Ätzen** Trockenätzen IBE	Vorderseite	Schichtpaket/ - dicke: **Cr/Au/Cr 10/200/10nm** Ätzstopp: **Si_3N_4** Bemerkung: **Achtung! Überätzen und anschließend Mikroskopkontrolle ob Füße weggeätzt sind.**	**Prozess ID:** Bemerkung:	
17	**Kontrolle**	Vorderseite	**Widerstandsprüfung auf Wafer**		

caesar

Flowchart ID-Nr.: **228-2014-05 IR-Sensor komplett - Basis**

FC- Betreuer: **Georg Siebke** Projekt: **Bionischer IR-Sensor**

Nr.	Prozess-Schritt:	Prozessseite	Prozess Parameter / Prozess Nummer	Ergebnisse / Bemerkung	Bearbeiter /Datum
18	**Ablacken** Lösungsmittel	Vorderseite Rückseite	Lack: **AZ1518** Lackdicke: **~2,2µm** Max. Ultraschall: **140%** Bemerkung: **NMP, Aceton, IPA**	**Prozess ID:** Bemerkung:	
19	**Kontrolle** Mikroskop	Vorderseite	**Prüfen, ob alle Lackreste entfernt wurden**		
___ **Wafer gehen über in FC 229 – IR-Sensor komplett – Stützstellen V2**					
___ **Wafer gehen über in FC – IR-Sensor komplett –**					

caesar

Flowchart ID-Nr.: **229-2014-05 IR-Sensor Prozessvariationen – Stützstellen V2**

FC- Betreuer: **Georg Siebke** Projekt: **Bionischer IR-Sensor**

Projektname: Bionischer IR-Sensor	**Projektgruppe/ Konto-Nr.: 50601**	**Flowchart- Betreuer: Georg Siebke**
Substrat-Art: Si-Wafer / DSP / 2 × 300µm gebondet	**Anzahl Substrate: 5**	

Nr.	Prozess-Schritt:	Prozessseite	Prozess Parameter / Prozess Nummer	Ergebnisse / Bemerkung	Bearbeiter /Datum
5 Wafer aus FC 228 übernommen					
1-19	**Siehe FC 228**				
20	**Beschichtung** PECVD	Vorderseite	Schicht: **SiO_2** Schichtdicke: **0,5 µm** Prozessparameter: Bemerkung: **Dielektrikum**	**Prozess ID:** **Prozessparameter:** Zeit: Leistung: Druck: Bemerkung:	
21	**Lithografie Nr. 4**	Vorderseite	Prozessname: **AZ1518/~2,2µm** Maskenname: **Maske 04 Dielektrikum V03** Justagemarke (Nr.): **4 auf 3** Substratoberfläche: **SiO_2** Topologie: Bemerkung: **Dielektrikum**	**Prozess ID:** Belacken: **HMDS 100°C/10s** **1,5ml AZ1518** **Prog.: AZ1518_M1** **SB: HP 100°C/1min** Belichten: **60mJ/cm^2** **Vac. Cont.** **WEC: Spacer** Entwickeln: **AZ726/30s** Hartbake: **Umluftofen 120°C/30min** Bemerkung: **HMDS der Maske**	

caesar

Flowchart ID-Nr.: **229-2014-05 IR-Sensor Prozessvariationen – Stützstellen V2**

FC- Betreuer: **Georg Siebke** Projekt: **Bionischer IR-Sensor**

Nr.	Prozess-Schritt:	Prozessseite	Prozess Parameter / Prozess Nummer	Ergebnisse / Bemerkung	Bearbeiter /Datum
22	**Ätzen** RIE	Vorderseite	Ätztiefe SiO_2: **0,5 µm** Ätzstopp: **Si_3N_4 / Cr** Bemerkung:	**Prozess ID:** Bemerkung:	
23	**Kontrolle**	Vorderseite	**Durchgangsprüfung an oberen Teststrukturen**		
24	**Ablacken** Nass (NMP, Aceton, IPA)	Vorderseite Rückseite	Lack: **AZ1518** Lackdicke: **~2,2µm** Max. Ultraschall: **100%** Bemerkung:	**Prozess ID:** Bemerkung:	
25	**Lithografie Nr. 5**	Vorderseite	Prozessname: **AZ15185µm** Maskenname: **Maske-05-Aus Gleichsmembran V03** Justagemarke (Nr.): **5 auf 4** Substratoberfläche: **SiO_2/Si_3N_4/Au** Topologie: Bemerkung: **Ausgleichsmembran**	**Prozess ID:** Belacken: **HMDS 100°C/1min** **3ml AZ1518** **Prog.: SK1000** **SB: HP 100°C/1min** Belichten: **165mJ/cm2** **Vac. Cont.** **WEC: Spacer** Entwickeln: **AZ726/60s** Hartbake: **Umluftofen 120°C/30min** Bemerkung:	
26	**Ätzen** Trockenätzen RIE	Vorderseite	Schichtpaket/ - dicke: **Si_3N_4 / SiO_2** **500 nm / 500nm** Ätzstopp: **Si** Bemerkung:	**Prozess ID:** Bemerkung:	

caesar

Flowchart ID-Nr.: **229-2014-05 IR-Sensor Prozessvariationen – Stützstellen V2**

FC- Betreuer: **Georg Siebke** Projekt: **Bionischer IR-Sensor**

Nr.	Prozess-Schritt:	Prozessseite	Prozess Parameter / Prozess Nummer	Ergebnisse / Bemerkung	Bearbeiter /Datum
27	**Ablacken** Nass (NMP, Aceton, IPA)	Vorderseite Rückseite	Lack: **AZ1518/~5µm** Lackdicke: **~5µm** Max. Ultraschall: **100%** Bemerkung:	**Prozess ID:** Bemerkung:	
28	**Beschichtung** Sputtern Unaxis	Vorderseite	Schicht: **Au** Schichtdicke: **80nm** Haftschicht/-dicke: **Cr/10nm** Sputteretch: **ja** Bemerkung: **Startschicht**	**Prozess ID:** **Prozessparameter:** Zeit: Leistung: Druck / Gasfluss: Osz. / Rot.: Bemerkung:	
29	**Lithografie Nr. 6**	Vorderseite	Prozessname: **AZ9260** Maskenname: **Maske 06 Obere Elektrode V03** Justagemarke (Nr.): **6 auf 3** Substratoberfläche: **Au** Topologie: Bemerkung: **zweite Elektrode**	**Prozess ID:** Belacken: **HMDS 100°C/10s** **3ml AZ9260** **Prog.: AZ9260_M1** **SB: Umluft 90°C / 1h** Belichten: **800 mJ/cm^2** **Vac. Cont.** **WEC: Spacer** Entwickeln: **AZ400K:H_2O = 1:4 6min** Hartbake: **Umluft: 110°C/30min** Bemerkung:	
30	**Galvanik**	Vorderseite	Metall: **Au** Fläche: **174mm^2** Schichtdicke: **4 µm** Bemerkung:	**Prozess ID:** Bemerkung:	

caesar

Flowchart ID-Nr.: **229-2014-05 IR-Sensor Prozessvariationen – Stützstellen V2**

FC- Betreuer: **Georg Siebke** Projekt: **Bionischer IR-Sensor**

Nr.	Prozess-Schritt:	Prozessseite	Prozess Parameter / Prozess Nummer	Ergebnisse / Bemerkung	Bearbeiter /Datum
31	**Beschichtung** Aufdampfen	Vorderseite	Schicht: **Cr** Schichtdicke: **250nm** Haftschicht/-dicke: Sputteretch: **ja** Bemerkung: **Haftschicht**	**Prozess ID:** **Prozessparameter:** Zeit: Leistung: Druck / Gasfluss: Osz. / Rot.: Bemerkung:	
32	**Lift-Off/Ablacken** Lösungsmittel	Vorderseite Rückseite	Lack: **AZ9260** Lackdicke: **~10µm** Max. Ultraschall: **100%** Bemerkung: **NMP, Aceton, IPA**	**Prozess ID:** Bemerkung:	
33	**Ätzen** Trockenätzen IBE	Vorderseite	Schichtpaket/ - dicke: **Au/Cr 80/10nm** Ätzstopp: **$SiO_2/Si_3N_4/Si$** Bemerkung:	**Prozess ID:** Bemerkung:	
34	**Kontrolle**	Vorderseite	**Widerstandsprüfung auf Wafer**		
35	**Beschichtung** PECVD	Vorderseite	Schicht: **SiO_2** Schichtdicke: **0,5µm** Prozessparameter: Bemerkung: **Passivierung**	**Prozess ID:** **Prozessparameter:** Zeit: Leistung: Druck: Bemerkung:	

4 von 10

caesar

Flowchart ID-Nr.: **229-2014-05 IR-Sensor Prozessvariationen – Stützstellen V2**

FC- Betreuer: **Georg Siebke** Projekt: **Bionischer IR-Sensor**

Nr.	Prozess-Schritt:	Prozessseite	Prozess Parameter / Prozess Nummer	Ergebnisse / Bemerkung	Bearbeiter /Datum
36	**Beschichtung** Aufdampfen	Rückseite	Schicht: **Al** Schichtdicke: **200nm** Haftschicht/-dicke: Sputteretch: **ja** Bemerkung: **Hartmaske**	**Prozess ID:** **Prozessparameter:** Zeit: Leistung: Druck / Gasfluss: Osz. / Rot.: Bemerkung:	
37	**Lithografie** Schutzlack	Vorderseite	Prozessname: **AZ1518/~5µm** Maskenname: Justagemarke (Nr.): keine Substratoberfläche: **$Au/Cr/SiO_2$** Topologie: Bemerkung: **Schutzlack**	**Prozess ID:** Belacken: **HMDS 100°C/10s** **3ml AZ1518** **Prog.: SK1000** **SB: HP 100°C / 1min** Belichten: Entwickeln: Hartbake: Bemerkung:	
38	**Lithografie Nr. 7**	Rückseite	Prozessname: **AZ1518/5µm** Maskenname: **Maske-08-Si3N4-RS V03** Justagemarke (Nr.): **8 auf 7** Substratoberfläche: **SiO2** Topologie: Bemerkung: **Hartmaske SiO_2/Si_3N_4**	**Prozess ID:** Belacken: **HMDS 100°C/1min** **3ml AZ1518** **Prog.: SK1000** **SB: HP 100°C/1min** Belichten: **165mJ/cm2** **Vac. Cont.** **WEC: Spacer** Entwickeln: **AZ726/60s** Hartbake: **Umluftofen 120°C/30 min** Bemerkung:	

5 von 10

caesar

Flowchart ID-Nr.: **229-2014-05 IR-Sensor Prozessvariationen – Stützstellen V2**

FC- Betreuer: **Georg Siebke** Projekt: **Bionischer IR-Sensor**

Nr.	Prozess-Schritt:	Prozessseite	Prozess Parameter / Prozess Nummer	Ergebnisse / Bemerkung	Bearbeiter /Datum
39	**Ätzen** Trockenätzen IBE	Rückseite	Schichtpaket/ - dicke: **Al 200nm** Ätzstopp: **SiO2** Bemerkung:	**Prozess ID:** **Bemerkung:**	
39	**Ätzen** Trockenätzen RIE	Rückseite	Schichtpaket/ - dicke: **SiO2 (therm.) / 1 µm** **Si3N4 / 0,5 µm** **SiO2 (PECVD) / 0,5 µm** Ätzstopp: **Si** Bemerkung:	**Prozess ID:** Bemerkung:	
40	**Ablacken** Nass (NMP, Aceton, IPA)	Vorderseite Rückseite	Lack: **AZ1518/~5µm** Lackdicke: **~5µm** Max. Ultraschall: **100%** Bemerkung:	**Prozess ID:** Bemerkung:	
41	**Lithografie** Schutzlack	Rückseite	Prozessname: **AZ1518/5µm** Maskenname: Justagemarke (Nr.): Substratoberfläche: **SiO_2/Si** Topologie: Bemerkung: **Schutzlack** **Klemm-Chuck verwenden!**	**Prozess ID:** Belacken: **HMDS 100°C/10s** **3ml AZ1518** **Prog.: SK1000** **SB: Umluft 100°C/30min** Belichten: Entwickeln: Hartbake: Bemerkung:	

caesar

Flowchart ID-Nr.: **229-2014-05 IR-Sensor Prozessvariationen – Stützstellen V2**

FC- Betreuer: **Georg Siebke** Projekt: **Bionischer IR-Sensor**

Nr.	Prozess-Schritt:	Prozessseite	Prozess Parameter / Prozess Nummer	Ergebnisse / Bemerkung	Bearbeiter /Datum
42	**Lithografie Nr. 8**	Vorderseite	Prozessname: **AZ1518/~5µm** Maskenname: **Maske-07-Opferschicht V03** Justagemarke (Nr.): **7 auf 3** Substratoberfläche: **SiO_2** Topologie: Bemerkung: **Klemm-Chuck verwenden!**	**Prozess ID:** Belacken: **HMDS 100°C/10s** **3ml AZ1518** **Prog.: SK1000** **SB: HP 100°C / 1min** Belichten: **165 mJ/cm^2** **Vac. Cont.** **WEC: Spacer** Entwickeln: **AZ726 60s** Hartbake: **Umluft: 120°C/30min** Bemerkung:	
43a	**Discum** TEPLA	Vorderseite Rückseite	Programm: **Prog 11** Bemerkung: **mit Käfig!** **Direkt vor dem Ätzen!**	**Prozess ID:** Bemerkung:	
43b	**Ätzen** Nassätzen BHF	Vorderseite Rückseite	Ätztiefe SiO_2: **1 µm senkrecht** **13 µm lateral** Ätzstopp: **Au/Si/Si_3N_4** Bemerkung: **Auflösen der Opfer-schicht, Überätzen (Lochabstand 22 µm)** **Nur nach Rücksprache mit Georg!**	**Prozess ID:** Bemerkung:	
44	**Reinigen** Carosche Säure	Vorderseite Rückseite	Prozess: **Carosche Säure** Bemerkung:	**Prozess ID:** Bemerkung:	

caesar

Flowchart ID-Nr.: **229-2014-05 IR-Sensor Prozessvariationen – Stützstellen V2**

FC- Betreuer: **Georg Siebke** Projekt: **Bionischer IR-Sensor**

Nr.	Prozess-Schritt:	Prozessseite	Prozess Parameter / Prozess Nummer	Ergebnisse / Bemerkung	Bearbeiter /Datum
45	**Beschichtung** PECVD	Vorderseite	Schicht: **Si** Schichtdicke: **1,5 µm** Prozessparameter: Bemerkung: **Stützen**	**Prozess ID:** **Prozessparameter:** Zeit: Leistung: Druck: Bemerkung:	
46	**Lithografie Nr. 9**	Rückseite	Prozessname: **AZ9260** Maskenname: **Maske-09-SiO2-RS V03** Justagemarke (Nr.): **9 auf 3** Substratoberfläche: **Al/Si** Topologie: Bemerkung: Klemm-Chuck verwenden!	**Prozess ID:** Belacken: **HMDS 100°C/10s** **3ml AZ9260** **Prog.: AZ9260_M1** **SB: Umluft 90°C / 1h** Belichten: **800 mJ/cm^2** **Vac. Cont.** **WEC: Spacer** Entwickeln: **AZ400K:H_2O = 1:4 6min** Hartbake: **Umluft: 110°C/30min** Bemerkung:	
47	**Ätzen** Trockenätzen ICP	Rückseite	Ätztiefe Silizium: **300µm** Ätzstopp: **keiner** Bemerkung:	**Prozess ID:** Bemerkung:	
48	**Ablacken** TEPLA	Vorderseite Rückseite	Lack: **AZ9260** Lackdicke: **10µm** Programm: **600W, bis Lack entfernt** Bemerkung: **mit Käfig!**	**Prozess ID:** Bemerkung:	

8 von 10

caesar

Flowchart ID-Nr.: **229-2014-05 IR-Sensor Prozessvariationen – Stützstellen V2**

FC- Betreuer: **Georg Siebke** Projekt: **Bionischer IR-Sensor**

Nr.	Prozess-Schritt:	Prozessseite	Prozess Parameter / Prozess Nummer	Ergebnisse / Bemerkung	Bearbeiter /Datum
49	**Ätzen** Trockenätzen ICP	Rückseite	Ätztiefe Silizium: **250µm** Ätzstopp: **keiner** Bemerkung: **exakte Tiefe unwichtig, restliches Si schützt Membran beim IBE-Ätzen**	**Prozess ID:** Bemerkung:	
50	**Ätzen** Trockenätzen IBE	Rückseite	Schichtpaket/ - dicke: **Al 200nm** Ätzstopp: **SiO2** Bemerkung: **Entfernung Hartmaske**	**Prozess ID:** **Bemerkung:**	
51	**Ätzen** Trockenätzen ICP	Rückseite	Ätztiefe Silizium: **~50µm** Ätzstopp: **SiO_2 Membran** Bemerkung: **vor dem Ätzen Tiefe bestimmen**	**Prozess ID:** Bemerkung:	
52	**Entweder RIE (52(1)) ODER BHF (52(2)) ODER überspringen (52(3))**				
52 (1)	**Ätzen** Trockenätzen RIE	Rückseite	Schichtpaket/ - dicke: **SiO_2 / 0,5µm** Ätzstopp: **Si_3N_4** Bemerkung:	**Prozess ID:** Bemerkung:	
52a (2)	**Discum** TEPLA	Vorderseite Rückseite	Programm: **Prog 11** Bemerkung: **mit Käfig! Direkt vor dem Ätzen!**	**Prozess ID:** Bemerkung:	
52b (2)	**Ätzen** Nassätzen BHF	Vorderseite Rückseite	Ätztiefe SiO_2: **0,5 µm** Ätzstopp: **Si_3N_4** Bemerkung: **leicht Überätzen!**	**Prozess ID:** Bemerkung:	
52 (3)	**Überspringen**		Oxidschicht unterhalb Membran stehen lassen		

9 von 10

caesar

Flowchart ID-Nr.: **229-2014-05 IR-Sensor Prozessvariationen – Stützstellen V2**

FC- Betreuer: **Georg Siebke** Projekt: **Bionischer IR-Sensor**

Nr.	Prozess-Schritt:	Prozessseite	Prozess Parameter / Prozess Nummer	Ergebnisse / Bemerkung	Bearbeiter /Datum
53	**Ätzen** Trockenätzen ICP	Vorderseite	Ätztiefe Silizium: **1,5 µm** Ätzstopp: **Stützen** Bemerkung:	**Prozess ID:** Bemerkung:	

Simplified sensor

Flowchart of the simplified sensor (see Chapter 6). To fabricate the chips with fixed electrode, the layer thicknesses in steps 5 and 6 have to adapted to 8 µm and 1 µm, respectively (see Section 6.2.2).

Flowchart ID-Nr.: **180-2012-11 IR-Sensor Testkapazität variable Elektroden (wie FC 159)**

FC- Betreuer: **Georg Siebke** Projekt: **Bionischer IR-Sensor**

Projektname: Bionischer IR-Sensor	**Projektgruppe/ Konto-Nr.: 50601**	**Flowchart- Betreuer: Georg Siebke**
Substrat-Art: Si-Wafer / DSP / 300 µm	**Anzahl Substrate: 14**	

Nr.	Prozess-Schritt:	Prozessseite	Prozess Parameter / Prozess Nummer	Ergebnisse / Bemerkung	Bearbeiter /Datum
1	**Losgründung**		Wafername: Material: **Si / DSP / 4" / 300µm** Vorbehandlung: **keine**		
2	**Lithografie Nr. 1**	Vorderseite	Prozessname: **AZ1518/~2,2µm** Maskenname: **Maske 01 V01 - Justagemarken + Vertiefung** Justagemarke (Nr.): **keine** Substratoberfläche: **Si** Topologie: **keine** Bemerkung:	**Prozess ID:** Belacken: **HMDS 100°C/10s** **1,5ml AZ1518** **Prog.: AZ1518_M1** **SB: HP 100°C/1min** Belichten: **55mJ/cm2** **Vac. Cont.** **WEC: Spacer** Entwickeln: **AZ726/30s** Hartbake: **Umluftofen 120°C/30min** Bemerkung: **HMDS der Maske**	
3	**Ätzen** Trockenätzen ICP	Vorderseite	Ätztiefe Silizium: **5 µm** Ätzstopp: **keiner** Bemerkung:	**Prozess ID:** Bemerkung:	
4	**Ablacken** Lösungsmittel	Vorderseite Rückseite	Lack: **AZ1518** Lackdicke: **~2,2µm** Max. Ultraschall: **100%** Bemerkung: **NMP, Aceton, IPA**	**Prozess ID:** Bemerkung:	

1 von 7

Flowchart ID-Nr.: **180-2012-11 IR-Sensor Testkapazität variable Elektroden (wie FC 159)**

FC- Betreuer: **Georg Siebke** Projekt: **Bionischer IR-Sensor**

Nr.	Prozess-Schritt:	Prozessseite	Prozess Parameter / Prozess Nummer	Ergebnisse / Bemerkung	Bearbeiter /Datum
5	**Beschichtung** Thermische Oxidation	Vorderseite Rückseite	Schicht: **SiO_2 Feucht** Schichtdicke: **0.5µm** Bemerkung:	**Prozess ID:** **Prozessparameter:** Tube: Temperatur: Zeit: Bemerkung:	
6	**Beschichtung** LPCVD	Vorderseite Rückseite	Schicht: **Si_3N_4** Schichtdicke: **siehe Beiblatt** Bemerkung: **Schicht mit Zugspan-nung Membran** **Messung der Schichtspannung**	**Prozess ID:** **Prozessparameter:** Tube: Temperatur: Zeit: Bemerkung:	
7	**Beschichtung** PECVD	Rückseite	Schicht: **SiO_2** Schichtdicke: **5 µm** Prozessparameter: Bemerkung:	**Prozess ID:** **Prozessparameter:** Zeit: Leistung: Druck: Bemerkung:	
8	**Beschichtung** Sputtern Unaxis	Vorderseite	Schicht: **Cr/Au/Cr** Schichtdicke: **10/200/10nm** Haftschicht/-dicke: **Cr/10nm** Sputteretch: **ja** Bemerkung:	**Prozess ID:** **Prozessparameter:** Zeit: Leistung: Druck / Gasfluss: Osz. / Rot.: Bemerkung:	

2 von 7

caesar

Flowchart ID-Nr.: **180-2012-11 IR-Sensor Testkapazität variable Elektroden (wie FC 159)**

FC- Betreuer: **Georg Siebke** Projekt: **Bionischer IR-Sensor**

Nr.	Prozess-Schritt:	Prozessseite	Prozess Parameter / Prozess Nummer	Ergebnisse / Bemerkung	Bearbeiter /Datum
9	**Lithografie Nr. 2**	Vorderseite	Prozessname: **AZ9260** Maskenname: **Maske 02 V01 – Elektrode** Justagemarke (Nr.): **2 auf 1** Substratoberfläche: **Au** Topologie: **5µm** Bemerkung: **Elektrode** **Maskendrehung siehe Beiblatt!!!**	**Prozess ID:** Belacken: **HMDS 100°C/10s** **3ml AZ9260** **Prog.: AZ9260_M1** **SB: Umluft 90°C / 1h** Belichten: **800 mJ/cm²** **Vac. Cont.** **WEC: Spacer** Entwickeln: **AZ400K:H_2O = 1:4 6min** Hartbake: **Umluft: 110°C/30min** Bemerkung:	
10	**Ätzen** Trockenätzen IBE	Vorderseite	Schichtpaket/ - dicke: **Cr/Au/Cr 10/200/10nm** Ätzstopp: **Si_3N_4** Bemerkung: **Kontrolle durch Widerstandsmessung**	**Prozess ID:** Bemerkung:	
11	**Ablacken** Lösungsmittel	Vorderseite Rückseite	Lack: **AZ9260** Lackdicke: **~10µm** Max. Ultraschall: **100%** Bemerkung: **NMP, Aceton, IPA**	**Prozess ID:** Bemerkung:	

caesar

Flowchart ID-Nr.: **180-2012-11 IR-Sensor Testkapazität variable Elektroden (wie FC 159)**

FC- Betreuer: **Georg Siebke** Projekt: **Bionischer IR-Sensor**

Nr.	Prozess-Schritt:	Prozessseite	Prozess Parameter / Prozess Nummer	Ergebnisse / Bemerkung	Bearbeiter /Datum
12	**Lithografie Nr. 3**	Rückseite	Prozessname: **AZ1518/~5µm** Maskenname: **Maske 03 V01 – Freistellen** Justagemarke (Nr.): **3 auf 1** Substratoberfläche: **Si_3N_4** Topologie: **keine** Bemerkung:	**Prozess ID:** Belacken: **HMDS 100°C/10s** **3ml AZ1518** **Prog.: SK1000** **SB: HP 100°C / 1min** Belichten: **165 mJ/cm²** **Vac. Cont.** **WEC: Spacer** Entwickeln: **AZ726 60s** Hartbake: **Umluft: 120°C/30min** Bemerkung:	
13	**Ätzen** RIE	Rückseite	Schichtpaket/ - dicke: **Si_3N_4 / 0,5 µm** **SiO_2 / 0,5µm** Ätzstopp: **Si** Bemerkung:	**Prozess ID:** Bemerkung:	
14	**Ablacken** Lösungsmittel	Vorderseite Rückseite	Lack: **AZ1518** Lackdicke: **~5µm** Max. Ultraschall: **kein** Bemerkung: **NMP, Aceton, IPA**	**Prozess ID:** Bemerkung:	

caesar

Flowchart ID-Nr.: **180-2012-11 IR-Sensor Testkapazität variable Elektroden (wie FC 159)**

FC- Betreuer: **Georg Siebke** Projekt: **Bionischer IR-Sensor**

Nr.	Prozess-Schritt:	Prozessseite	Prozess Parameter / Prozess Nummer	Ergebnisse / Bemerkung	Bearbeiter /Datum
15	**Lithografie** Schutzlack	Vorderseite	Prozessname: **AZ1518/~2,2µm** Maskenname: Justagemarke (Nr.): Substratoberfläche: **Si_3N_4, Cr** Topologie: Bemerkung: **Schutzlack**	**Prozess ID:** Belacken: **HMDS 100°C/10s** **1,5ml AZ1518** **Prog.: AZ1518_M1** **SB: HP 100°C/1min** Belichten: Entwickeln: Hartbake: Bemerkung: **ACHTUNG! Klemm-Chuck verwenden!**	
16	**Ätzen** Trockenätzen ICP	Rückseite	Ätztiefe Silizium: **120 µm** Ätzstopp: **SiO_2** Bemerkung:	**Prozess ID:** Bemerkung:	
17	**Wafersäge**	Vorderseite	Material: **Si** Abmaße: **15x15 mm^2** Sägemarken: Bemerkung: **Rückseite aufkleben!**	**Prozess ID:** Bemerkung:	
18	**Ätzen** Trockenätzen ICP	Rückseite	Ätztiefe Silizium: **180 µm** Ätzstopp: **SiO_2** Bemerkung:	**Prozess ID:** Bemerkung:	

caesar

Flowchart ID-Nr.: **180-2012-11 IR-Sensor Testkapazität variable Elektroden (wie FC 159)**

FC- Betreuer: **Georg Siebke** Projekt: **Bionischer IR-Sensor**

Nr.	Prozess-Schritt:	Prozessseite	Prozess Parameter / Prozess Nummer	Ergebnisse / Bemerkung	Bearbeiter /Datum
19	**Ablacken** TEPLA Lösungsmittel	Vorderseite Rückseite	Lack: **AZ1518** Lackdicke: **~2,2µm** Max. Ultraschall: **kein** Bemerkung: **TEPLA 30 min 800W** **mit Käfig** **NMP, Aceton, IPA** **u.U. wiederholen**	**Prozess ID:** Bemerkung:	
20	**Descum** TEPLA	Vorderseite Rückseite	Programm: **Prog 11** Bemerkung: **mit Käfig!** **Direkt vor dem Ätzen!**	**Prozess ID:** Bemerkung:	
21	**Ätzen** Nassätzen BHF	Vorderseite Rückseite	**Descum nicht vergessen!** Ätztiefe SiO_2: **0,5 µm** Ätzstopp: **Si_3N_4** Bemerkung: **leicht Überätzen!**	**Prozess ID:** Bemerkung:	

caesar

Flowchart ID-Nr.: **180-2012-11 IR-Sensor Testkapazität variable Elektroden (wie FC 159)**

FC- Betreuer: **Georg Siebke** Projekt: **Bionischer IR-Sensor**

Variationen

Wafer	Schichtdicke Si_3N_4 / Spannung	Drehung Maske
1-8 (130, 135, 137, 138, 139, 143, 144, 145)	500 nm	0
9-11 (062, 063, 064)	500 nm	180°
12-14 (160, 161, 163)	350 nm	0

Fluidic low-pass filter

Flowchart of the test system for the fluidic low-pass filter (see Section 3.4.1).

Flowchart ID-Nr.: **230-2014-06 IR-Sensor Fluidiktest – wie FC 202**

FC- Betreuer: **Georg Siebke** Projekt: **Bionischer IR-Sensor**

Projektname: Bionischer IR-Sensor	Projektgruppe/ Konto-Nr.: 50601	Flowchart- Betreuer: Georg Siebke
Substrat-Art: Si-Wafer / DSP / 525µm	Anzahl Substrate: 8	

Nr.	Prozess-Schritt:	Prozessseite	Prozess Parameter / Prozess Nummer	Ergebnisse / Bemerkung	Bearbeiter /Datum
1	**Losgründung**		Wafername: Material: **Si / DSP / 4" / 525µm** Vorbehandlung: **keine**		
2	**Lithografie Nr. 1**	Vorderseite	Prozessname: **AZ9260/~10µm** Maskenname: **Maske 01 V01 – Kanal und Marken** Justagemarke (Nr.): **keine** Substratoberfläche: **Si** Topologie: **keine** Bemerkung:	**Prozess ID:** Belacken: **HMDS 100°C/10s** **3ml AZ9260** **Prog.: AZ9260_M1** **SB: Umluft 90°C / 1h** Belichten: **800 mJ/cm²** **Vac. Cont.** **WEC: Spacer** Entwickeln: **AZ400K:H_2O = 1:4 6min** Hartbake: **Umluft: 110°C/30min** Bemerkung:	
3	**Ätzen** Trockenätzen ICP	Vorderseite	Ätztiefe Silizium: **4x 200µm, 4x 250µm** Ätzstopp: **keiner** Bemerkung:	**Prozess ID:** Bemerkung:	
4	**Ablacken** TEPLA	Vorderseite Rückseite	Programm: Lack: **AZ9260** Lackdicke: **~10µm** Schicht unter dem Lack: **Si** Bemerkung: **ohne Käfig**	**Prozess ID:** Bemerkung:	

1 von 3

Flowchart ID-Nr.: **230-2014-06 IR-Sensor Fluidiktest – wie FC 202**

FC- Betreuer: **Georg Siebke** Projekt: **Bionischer IR-Sensor**

Nr.	Prozess-Schritt:	Prozessseite	Prozess Parameter / Prozess Nummer	Ergebnisse / Bemerkung	Bearbeiter /Datum
5	**Messung**	Vorderseite	Bestimmung der Kanaltiefe für **jeden** Wafer		
6a	**Reinigen** Carosche Säure	Vorderseite Rückseite	**Prozessname**: Reinigung des Wafers **Zeit**: 10 min bis 15 min **Temperatur**: frisch ansetzen **Bemerkung: Direkt vor dem Bonden durchführen!**	**Bemerkung**:	
6b	**Anodisches Bonden**	Vorderseite	**Prozessname**: Anodic Vac 1 **Material**: Si-Wafer / Pyrex **Prozessparameter**: **Temperatur**: **Zeit**: **Bemerkung:**	**Bemerkung**:	
7	**Lithografie Nr. 2**	Rückseite	Prozessname: **AZ9260/~10µm** Maskenname: **Maske 02 V01 – Oeffnungen** Justagemarke (Nr.): **2 auf 1** Substratoberfläche: **SiO_2** Topologie: **keine** Bemerkung:	**Prozess ID:** Belacken: **HMDS 100°C/10s** **3ml AZ9260** **Prog.: AZ9260_M1** **SB: Umluft 90°C / 1h** Belichten: **800 mJ/cm²** **Vac. Cont.** **WEC: Spacer** Entwickeln: **AZ400K:H_2O = 1:4 6min** Hartbake: **Umluft: 110°C/30min** Bemerkung:	

2 von 3

caesar

Flowchart ID-Nr.: **230-2014-06 IR-Sensor Fluidiktest – wie FC 202**

FC- Betreuer: **Georg Siebke** Projekt: **Bionischer IR-Sensor**

Nr.	Prozess-Schritt:	Prozessseite	Prozess Parameter / Prozess Nummer	Ergebnisse / Bemerkung	Bearbeiter /Datum
8	**Ätzen** Trockenätzen ICP	Rückseite	Ätztiefe Silizium: **525µm** Ätzstopp: **Glas** Bemerkung:	**Prozess ID:** Bemerkung:	
9	**Ablacken** TEPLA	Vorderseite Rückseite	Programm: Lack: **AZ9260** Lackdicke: **~10µm** Schicht unter dem Lack: **Si** Bemerkung: **ohne Käfig**	**Prozess ID:** Bemerkung:	

B Masks

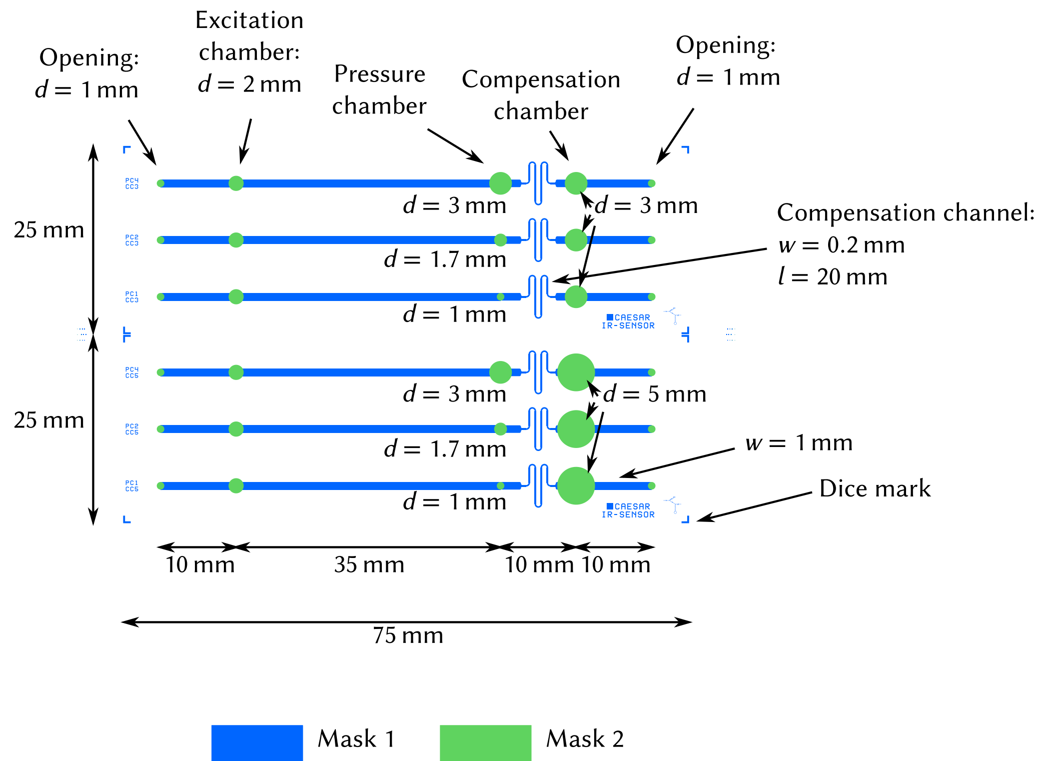

Figure 68: Masks of the Si-chip for the test of the fluidic low-pass filter. d: diameter, w: width, l: length.

C Electronics

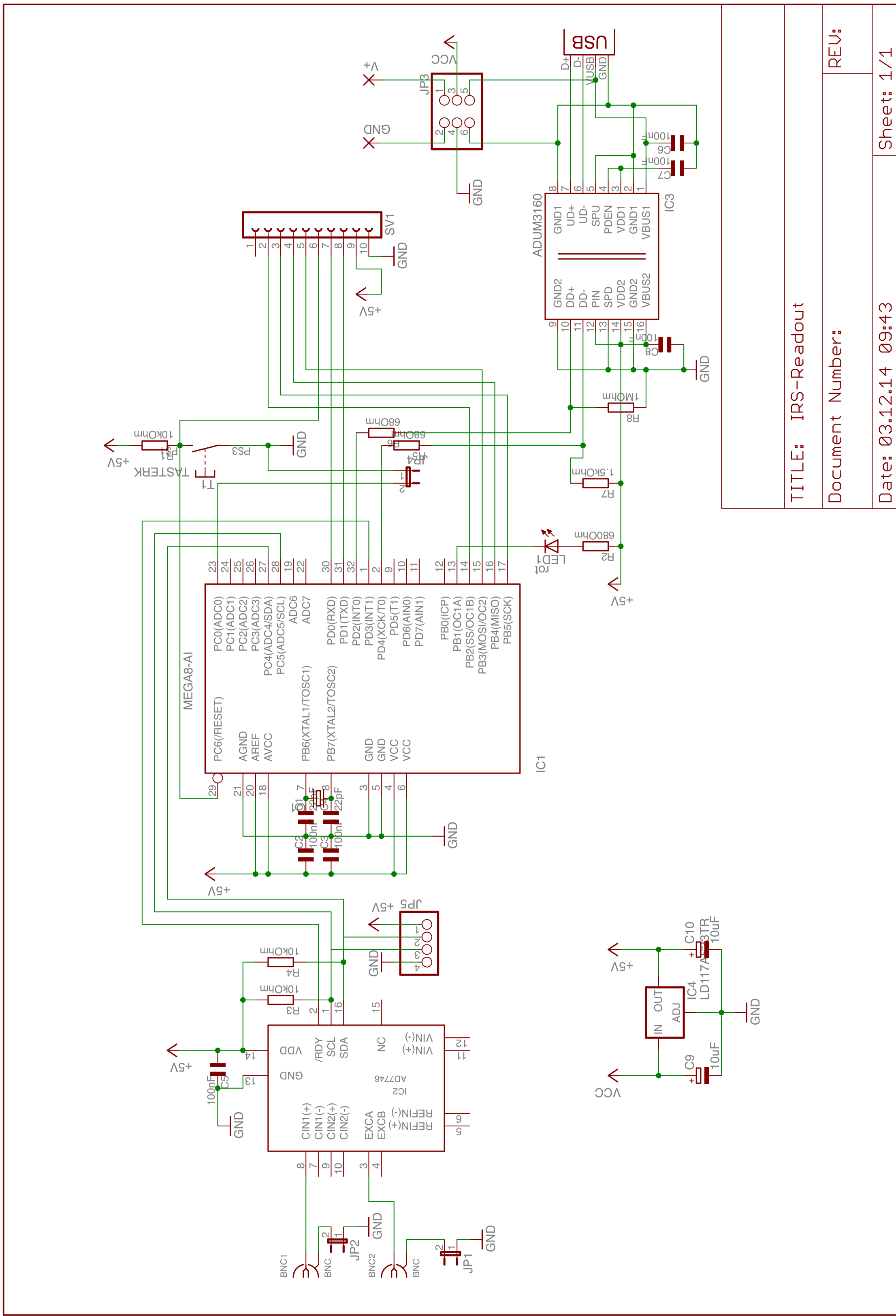

Figure 69: Schematic of the electronic circuit of the readout electronics (see Section 5.1).

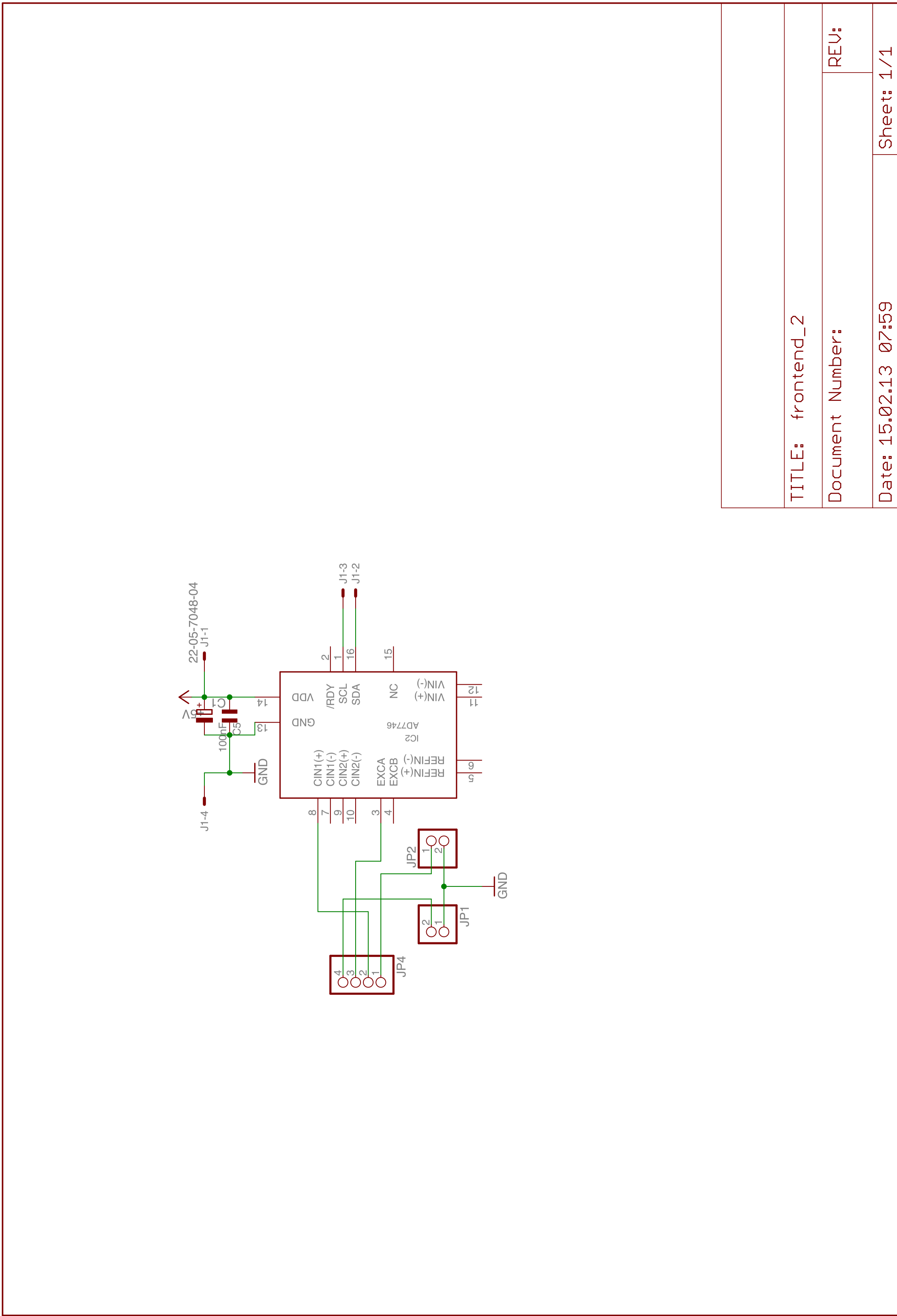

Figure 70: Schematic of the electronic circuit of the frontend electronics (see Sections 5.1 and 6.1).

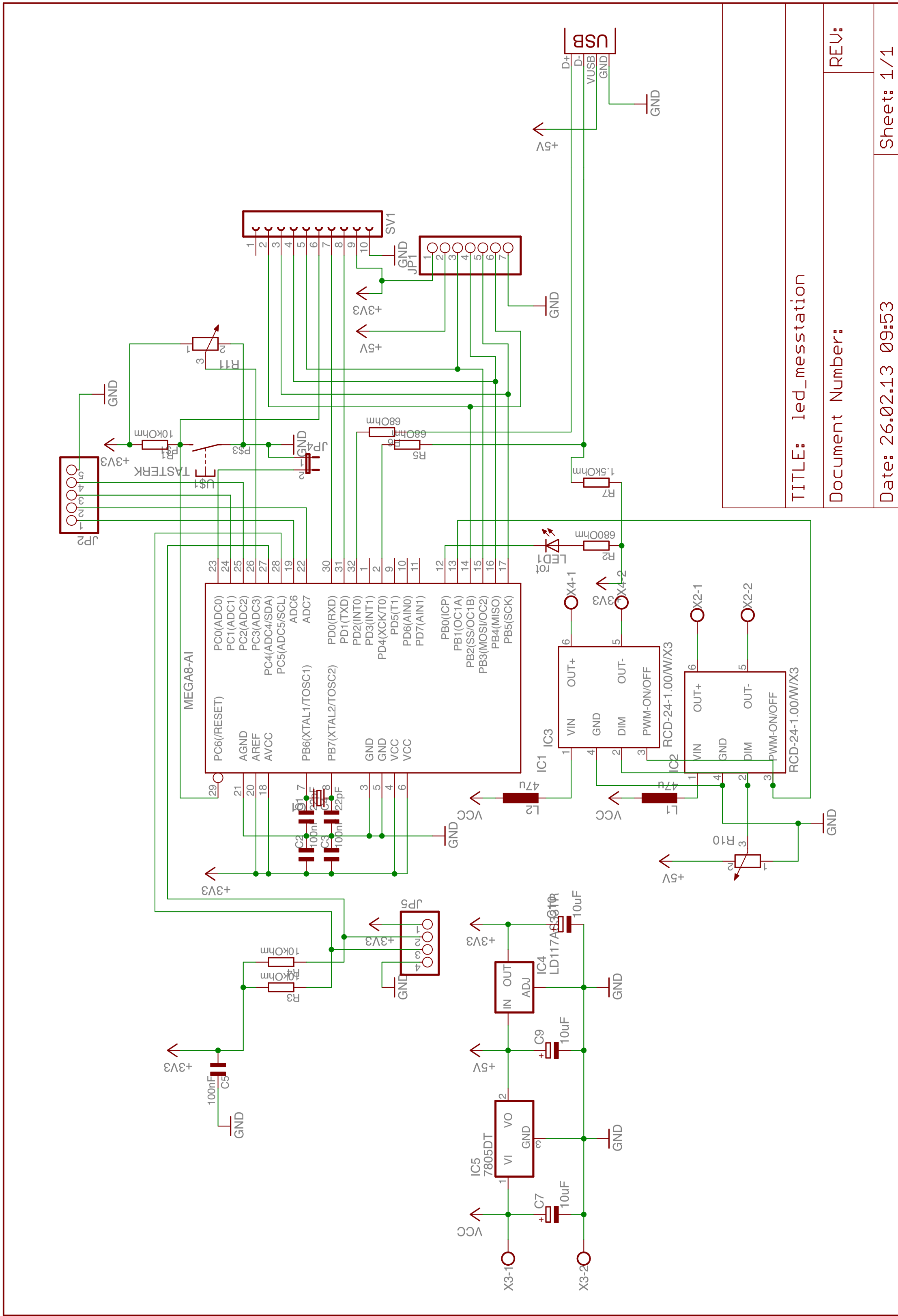

Figure 71: Schematic of the electronic circuit of the modulated IR radiation source (see Section 5.3).

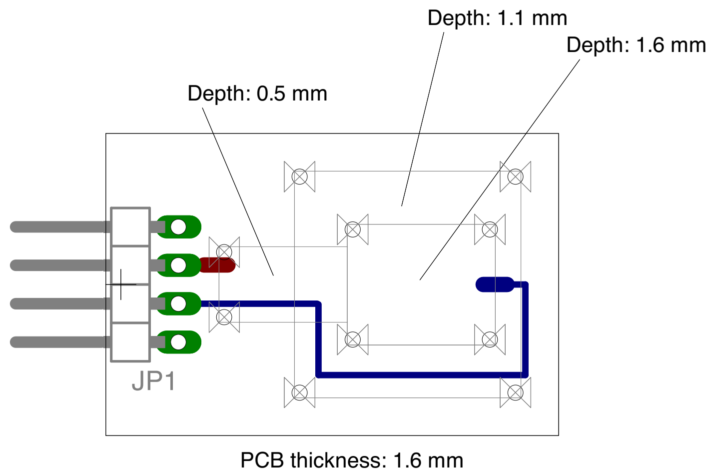

Figure 72: Design of the PCB holding the simplified sensor (see Section 6.1). Scale 2:1.

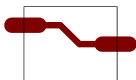

Figure 73: Design of the PCB contacting the simplified sensor (see Section 6.1). Scale 2:1.

List of Figures

1	The biological IR-sensor	3
2	Simplified cross section of one IR sensillum of the beetle	4
3	Detection chain of the IR sensillae of *Melanophila*	4
4	Shape of the spectral responsivity of thermal and photon detectors	9
5	Basic procedure to create three-dimensional structures within micro systems technology	11
6	Basic photlithography procedure using a positive resist	14
7	Concept of the biomimetic IR sensor	20
8	Overview of the theoretical model	20
9	Overview of the fluidic model	21
10	Equivalence of membrane and spring within the model description	22
11	Overview of the thermal model	24
12	Overview of the environmental model	26
13	Frequency spectrum of the membrane deflection for different parts of the model	29
14	Complete frequency spectrum of the sensor response	30
15	COMSOL Multiphysics simulation for the membrane deflection	33
16	Simulation of the deflection of a Si_3N_4 membrane	34
17	View of the sensor model for the simulation of heat transfer	34
18	Concept of the chip to validate the fluidic low-pass filter	35
19	Design of the chip to validate the fluidic low-pass filter	36
20	Simplified process flow of the chip to validate the fluidic low-pass filter	36
21	Test setup for the fluidic low-pass filter	37
22	Pretest of the fluidic low-pass filter	39
23	Experimental test of the fluidic low-pass filter	41
24	Comparison of measured and simulated spring constants	42
25	Simplified geometries for the estimation of the minimum required irradiance	43
26	Transfer of the biological sensor to the technological sensor	46
27	Influence of different parameters on the frequency spectrum	48
28	Steps I – III of the micro-technological process flow of the µ-biomimetic sensor	50
29	Steps IV – VI of the micro-technological process flow of the µ-biomimetic sensor	51
30	Steps VII – IX of the micro-technological process flow of the µ-biomimetic sensor	52
31	Steps X – XII of the micro-technological process flow of the µ-biomimetic sensor	53

32 Steps XIII – XV of the micro-technological process flow of the μ-biomimetic sensor . . . 54
33 Steps XVI – XVIII of the micro-technological process flow of the μ-biomimetic sensor . . . 55
34 Steps XIX – XXI of the micro-technological process flow of the μ-biomimetic sensor . . . 56
35 Procedure for bubble-free filling . . . 58
36 The micro-channel after the filling procedure . . . 58
37 Casting of the PDMS layer . . . 59
38 Assembly of the μ-biomimetic sensor . . . 60

39 Components required to characterize an IR sensor . . . 61
40 Components of the electronics used to read out the μ-biomimetic IR sensor 62
41 Electronics board for the read out the μ-biomimetic IR sensor . . . 63
42 Functions of the data acquisition software . . . 64
43 Window of the DAQ used to start and stop measurements and plots of the capacitance, temperature, and voltage . . . 64
44 Windows of the DAQ used to configure the capacitance measurements and for the real-time FFT . . . 65
45 Windows of the DAQ used to configure the voltage and temperature measurements and the storage of measured data . . . 65
46 Experimental setup for testing the sensors . . . 66

47 Schematics of the sensor . . . 70
48 Steps I – IV of the micro-technological process flow of the simplified sensor 71
49 Steps V – VIII of the micro-technological process flow of the simplified sensor 72
50 Assembled sensors . . . 73
51 Parasitic capacitances . . . 73
52 Equivalent circuit of the parasitic capacitances after the connection of the Si substrate to ground . . . 75
53 Sample measurement for different modulation frequencies with reduced time spans . . . 76
54 Amplitude $C_0(f)$ of the sensor response to a sinusoidal oscillation of the irradiance with an amplitude of $E_0 = 58\,\mathrm{W\,m^{-2}}$ at the frequency f . . . 79
55 Averaged amplitude $C_{0,\mathrm{avg}}$ and spread for identical sensors . . . 79
56 Temperature dependent deflection of the air-filled sensor . . . 80
57 Amplitudes for different modulation frequencies at different temperatures for one sensor . . . 82
58 Spring constants calculated from Figure 57 for each frequency and the simulated value . . . 82

59 Micro-technological process flow of μ-capacitor using the standard process 86
60 Micro-technological process flow of μ-capacitor using the sacrificial a-Si layer process . . . 88
61 Residuals of the sacrificial layer after ICP etching . . . 88
62 Micro-technological process flow of μ-capacitor using the support point process . . . 89
63 Residual resist preventing the BHF etching of the sacrificial layer . . . 90

64 Micro-technological process flow of μ-capacitor using the modified support point process . . . 92
65 μ-capacitors on a point probe station . . . 93
66 Measurement of the change in capacitance ΔC depending on the chip temperature T . . . 93

67 Components of the μ-biomimetic sensor . . . 95

68 Masks of the Si-chip for the test of the fluidic low-pass filter . . . 115

69 Schematic of the electronic circuit of the readout electronics . . . 118
70 Schematic of the electronic circuit of the frontend electronics . . . 119
71 Schematic of the electronic circuit of the modulated IR radiation source . . 120
72 Design of the PCB holding the simplified sensor . . . 121
73 Design of the PCB contacting the simplified sensor . . . 121

List of Tables

1 Radiometric terms used to describe IR radiation 7

2 Properties of the Si_3N_4 and PDMS (Sylgard 184) layers used to simulate the membrane 33
3 Resulting spring constants for Si_3N_4 membranes with different stress values 34
4 Geometry, experimental and simulated spring constants 38
5 Young's modulus of PDMS for different thicknesses 42
6 Physical properties of water and silicone oil and the minimum radiation intensity of the sensillum 44

7 Dimensions of the sensor used for the model calculations 47
8 Parameters used for the calculations of the frequency spectra 47

9 Properties of the capacitance-to-digital converter AD7745 62

10 Parasitic capacitances 74
11 Total base capacitance of the sensors, including parasitic capacitances . . . 78

12 Diameter, experimental and simulated values of the spring constant of the μ-capacitor 94

List of Symbols

A	area
b	depth
BW	bandwidth
c	specific heat capacity
c	speed of light
C	capacitance
C	heat capacity
d	diameter
d	distance
d'	rectangle side length
D	spring constant
D	detectivity
D^*	specific detectivity
E	energy
E_e	irradiance
E	Young's modulus
f	modulation frequency
F	force
$\mathscr{F}$	Fourier transform
h	Planck constant
I	current
I_e	radiant intensity
l	length
L_e	radiance
M_e	radiant exitance
n	count
NEP	noise equivalent power
p	pressure
p	pyroelectric coefficient
q	heat flux per area
Q	radiant energy
Q	heat
R	radius
$\mathscr{R}$	responsivity
SNR	signal-to-noise ratio
t	time
t	thickness
T	temperature
U	voltage
V	volume
W	work
x	deflection
α	coefficient of linear thermal expansion
α'	combined thermal expansion
α	temperature coefficient of resistance
γ	Hagen Poiseuille coefficient
δ	volume ratio
ε	emissivity
ε	relative permittivity
ε_0	vacuum permittivity
η	dynamic viscosity
θ	Seebeck coefficient
λ	thermal conduction
λ'	combined thermal conduction
λ	wavelength
ν	optical frequency
ν	Poisson's ratio
ρ	density
σ	residual stress
σ	Stefan Boltzmann constant
σ'	combined Stefan Boltzmann constant
σ	tension
$\boldsymbol{\Phi}$	heat flux
$\boldsymbol{\Phi}_e$	radiant flux
ω	angular frequency

List of Abbreviations

AC	alternating current
AFM	atomic force microscope
BHF	buffered hydrofluoric acid
BST	barium strontium titanate
BW	bandwidth
CAD	computer aided design
CDC	capacitance-to-digital converter
CVD	chemical vapour deposition
DAQ	data acquisition
DCS	dichlorosilane
DFT	discrete Fourier transformation
DNQ	Diazonaphtoquinone-sulphonate
DRIE	deep reactive ion etching
FFT	fast Fourier transformation
FPA	focal plane array
GUI	graphical user interface
HF	hydrofluoric acid
IBE	ion beam etching
IC	integrated circuit
ICP	inductively coupled plasma
IR	infrared
LED	light-emitting diode
LPCVD	low pressure chemical vapour deposition
MEMS	micro-electro-mechanical systems
MOEMS	micro-opto-electro-mechanical systems
NEP	noise equivalent power
PCB	printed circuit board
PDMS	polydimethylsiloxane
PECVD	plasma enhanced chemical vapour deposition
PMMA	poly(methyl methacrylate)
PVD	physical vapour deposition
PWM	pulse width modulation
RCA	Radio Corporation of America
RIE	reactive ion etching
SEM	scanning electron microscope
SNR	signal-to-noise ratio
USB	universal serial bus

Bibliography

[1] W. G. Evans, “Infra-red receptors in *Melanophila acuminata* DeGeer”, Nature **202**, 211 (1964).

[2] W. G. Evans, “Perception of infrared radiation from forest fires by *Melanophila acuminata* DeGeer (Buprestidae Coleoptera)”, Ecology **47**, 1061–1065 (1966).

[3] H. Schmitz and H. Bleckmann, “Fine structure and physiology of the infrared receptor of beetles of the genus *Melanophila* (Coleoptera: Buprestidae)”, Int. J. Insect Morphol. Embryol. **26**, 1441–50 (1997).

[4] T. Vondran, K. H. Apel, and H. Schmitz, “The infrared receptor of *Melanophila acuminata* De Geer (Coleoptera: Buprestidae): ultrastructural study of a unique insect thermoreceptor and its possible descent from a hair mechanoreceptor”, Tissue Cell **27**, 645–58 (1995).

[5] A. Schmitz, A. Sehrbrock, and H. Schmitz, “The analysis of the mechanosensory origin of the infrared sensilla in *Melanophila acuminata* (Coeloptera; Buprestidae) adduces new insight into the transduction mechanism”, Arthropod Struct. Dev. **36**, 291–303 (2007).

[6] H. Schmitz, H. Bleckmann, and M. Murtz, “Infrared detection in a beetle”, Nature **386**, 773 (1997).

[7] W. Gronenberg and H. Schmitz, “Afferent projections of infrared-sensitive sensilla in the beetle *Melanophila acuminata* (Coleoptera: Buprestidae)”, Cell Tissue Res. **297**, 311–8 (1999).

[8] D. X. Hammer, H. Schmitz, A. Schmitz, H. G. Rylander, and A. J. Welch, “Sensitivity threshold and response characteristics of infrared detection in the beetle *Melanophila acuminata* (Coleoptera: Buprestidae)”, Comp. Biochem. Physiol., Part A: Mol. Integr. Physiol. **128**, 805–19 (2001).

[9] D. X. Hammer, J. Seigert, M. O. Stone, H. G. Rylander, and A. J. Welch, “Infrared spectral sensitivity of *Melanophila acuminata*”, J. Insect Physiol. **47**, 1441–50 (2001).

[10] W. G. Evans, “Infrared radiation sensors of *Melanophila acuminata* (Coleoptera: Buprestidae): a thermopneumatic model”, Ann. Entomol. Soc. Am. **98** (2005).

[11] G. Siebke, P. Holik, S. Schmitz, M. Lacher, and S. Steltenkamp, “A μ-biomimetic uncooled infrared-sensor”, in Bioinspiration, biomimetics, and bioreplication 2013, Vol. 8686, edited by R. J. Martín-Palma and A. Lakhtakia, Proc. SPIE (2013).

[12] D. Klocke, A. Schmitz, H. Soltner, H. Bousack, and H. Schmitz, “Infrared receptors in pyrophilous (“fire loving”) insects as model for new un-cooled infrared sensors”, Beilstein J. Nanotechnol. **2**, 186–97 (2011).

[13] M. Müller, M. Olek, M. Giersig, and H. Schmitz, "Micromechanical properties of consecutive layers in specialized insect cuticle: the gula of *Pachnoda marginata* (Coleoptera, Scarabaeidae) and the infrared sensilla of *Melanophila acuminata* (Coleoptera, Buprestidae)", J. Exp. Biol. **211**, 2576–83 (2008).

[14] H. Schmitz and H. Bleckmann, "The photomechanic infrared receptor for the detection of forest fires in the beetle *Melanophila acuminata* (Coleoptera: Buprestidae)", J. Comp. Physiol. A: Neuroethol. Sens. Neural. Behav. Physiol. **182**, 647–57 (1998).

[15] H. Schmitz and H. Bousack, "Modelling a historic oil-tank fire allows an estimation of the sensitivity of the infrared receptors in pyrophilous melanophila beetles", PLoS ONE **7**, e37627 (2012).

[16] Excelitas Technologies, *Infrared sensing catalogue* (2011).

[17] H. Schmitz, M. Murtz, and H. Bleckmann, "Responses of the infrared sensilla of *Melanophila acuminata* (Coleoptera: Buprestidae) to monochromatic infrared stimulation", J. Comp. Physiol. A: Neuroethol. Sens. Neural. Behav. Physiol. **186**, 543–9 (2000).

[18] D. X. Hammer, D. Dave, T. E. Milner, B. Choi, H. G. Rylander, and A. J. Welch, "Investigation of the transduction mechanism of infrared detection in *Melanophila acuminata*: photo-thermal-mechanical hypothesis", Comp. Biochem. Physiol., Part A: Mol. Integr. Physiol. **132**, 381–92 (2002).

[19] H. Schmitz and S. Trenner, "Electrophysiological characterization of the multipolar thermoreceptors in the "fire-beetle" *Merimna atrata* and comparison with the infrared sensilla of melanophila acuminata (both coleoptera, buprestidae)", J. Comp. Physiol. A: Neuroethol. Sens. Neural. Behav. Physiol. **189**, 715–22 (2003).

[20] E. Van Dyke, "Buprestid swarming", Pan-Pac. Entomol. **3**, 41 (1926).

[21] G. Uhmann, "Melanophila acuminata Deg. in der Oberpfalz (Coleopt., Buprestidae)", Nachrichtenblatt der Bayerischen Entomologen **19** (1970).

[22] W. G. Evans, "Reproductive role of infrared radiation sensors of *Melanophila acuminata* (Coleoptera: Buprestidae) at forest fires", Ann. Entomol. Soc. Am. **103**, 823–6 (2010).

[23] M. Israelowitz, J.-A. Kwon, S. W. H. Rizvi, C. Gille, and H. P. von Schroeder, "Mechanism of infrared detection and transduction by beetle *Melanophila Acuminata*", J. Bionic. Eng. **8**, 129–139 (2011).

[24] A. L. Campbell, R. R. Naik, L. Sowards, and M. O. Stone, "Biological infrared imaging and sensing", Micron **33**, 211–25 (2002).

[25] A. Schmitz, M. Gebhardt, and H. Schmitz, "Microfluidic photomechanic infrared receptors in a pyrophilous flat bug", Naturwissenschaften **95**, 455–60 (2008).

[26] A. Schmitz, H. Schaetzel, and H. Schmitz, "Distribution and functional morphology of photomechanic infrared sensilla in flat bugs of the genus *Aradus* (Heteroptera, Aradidae)", Arthropod Struct. Dev. **39**, 17–25 (2010).

[27] E. S. Schneider and H. Schmitz, "Bimodal innervation of the infrared organ of *Merimna atrata* (Coleoptera, Buprestidae) by thermo- and mechanosensory units", Arthropod Struct. Dev. **42**, 135–142 (2013).

[28] H. Schmitz, A. Schmitz, S. Trenner, and H. Bleckmann, "A new type of insect infrared organ of low thermal mass", Naturwissenschaften **89** (2002).

[29] E. Kreiss, H. Schmitz, and M. Gebhardt, “Electrophysiological characterisation of the infrared organ of the Australian ”little ash beetle” Acanthocnemus nigricans (Coleoptera, Acanthocnemidae)”, J. Comp. Physiol. A: Neuroethol. Sens. Neural. Behav. Physiol. **193**, 729–739 (2007).

[30] G. J. Molenaar, “Anatomy and physiology of infrared sensitivity of snakes”, in *Biology of the reptilia*, edited by C. Gans and P. S. Ulinski, Neurology C, Vol. 17 (The University of Chicago Press, Chicago, 1992), pp. 367–453.

[31] T. de Cock Buning, “Thermal sensitivity as a specialization for prey capture and feeding in snakes”, Am. Zool. **23**, 363–75 (1983).

[32] A. Rogalski, *Infrared detectors*, 2nd ed. (CDC Press, Boca Raton, FL, 2011).

[33] A. Daniels, *Field guide to infrared systems, detectors, and FPAs*, 2. (SPIE Press, Bellingham, Washington, 2010).

[34] J. L. Corbeil, N. V. Lavrik, S. Rajic, and P. G. Datskos, “”Self-leveling”uncooled microcantilever thermal detector”, Appl. Phys. Lett. **81**, 1306–1308 (2002).

[35] P. G. Datskos, N. V. Lavrik, S. R. Hunter, S. Rajic, and D. Grbovic, “Infrared imaging using arrays of SiO_2 micromechanical detectors”, Opt. Lett. **37**, 3966–3968 (2012).

[36] X. C. Zhang, E. B. Myers, J. E. Sader, and M. L. Roukes, “Nanomechanical torsional resonators for frequency-shift infrared thermal sensing”, Nano Lett. **13**, 1528–1534 (2013).

[37] M. J. E. Golay, “A pneumatic infra-red detector”, Rev. Sci. Instrum. **18**, 357–62 (1947).

[38] M. J. E. Golay, “Theoretical consideration in heat and infra-red detection, with particular reference to the pneumatic detector”, Rev. Sci. Instrum. **18**, 347–356 (1947).

[39] M. J. E. Golay, “The theoretical and practical sensitivity of the pneumatic infra-red detector”, Rev. Sci. Instrum. **20**, 816–820 (1949).

[40] J.-B. Chévrier, K. Baert, T. Slater, and A. Verbist, “Micromachined infrared pneumatic detector for gas sensor”, Microsyst. Technol. **1**, 71–74 (1995).

[41] T. Kenny, J. Reynolds, J. Podosek, E. Vote, L. Miller, H. Rockstad, and W. Kaiser, “Micromachined infrared sensors using tunneling displacement transducers”, Rev. Sci. Instrum. **67**, 112–128 (1996).

[42] M. E. McConney, K. D. Anderson, L. L. Brott, R. R. Naik, and V. V. Tsukruk, “Bioinspired material approaches to sensing”, Adv. Funct. Mater. **19**, 2527–44 (2009).

[43] A. D. Pris, Y. Utturkar, C. Surman, W. G. Morris, A. Vert, S. Zalyubovskiy, T. Deng, H. T. Ghiradella, and R. A. Potyrailo, “Towards high-speed imaging of infrared photons with bio-inspired nanoarchitectures”, Nature Photon. **6**, 195–200 (2012).

[44] R. Ciupa and A. Rogalski, “Performance limitations of photon and thermal infrared detectors”, Opto-Electron. Rev., 257–266 (1997).

[45] W. Menz and J. Mohr, *Mikrosystemtechnologie für Ingenieure*, 2nd ed. (VCH, Weinheim, 1997).

[46] T. M. Adams and R. A. Layton, *Introductory MEMS* (Springer, New York, 2010).

[47] P. French, P. Sarro, R. Mallée, E. Fakkeldij, and R. Wolffenbuttel, “Optimization of a low-stress silicon nitride process for surface-micromachining applications”, Sens. Actuators, A **58**, 149–157 (1997).

[48] J. M. Olson, "Analysis of LPCVD process conditions for the deposition of low stress silicon nitride. Part I: preliminary LPCVD experiments", Mater. Sci. Semicond. Process. **5**, 51–60 (2002).

[49] S. C. Witczak, M. Gaitan, J. S. Suehle, M. C. Peckerar, and D. I. Ma, "The interaction of stoichiometry, mechanical stress, and interface trap density in LPCVD Si-rich SiN_x-Si structures", Solid State Electron. **37**, 1695–1704 (1994).

[50] P. Pan and W. Berry, "The composition and physical properties of LPCVD silicon nitride deposited with different NH_3/SiH_2Cl_2 gas ratios", J. Electrochem. Soc. **132**, 3001–3005 (1985).

[51] S. Habermehl, "Stress relaxation in Si-rich silicon nitride thin films", J. Appl. Phys. **83**, 4672–4677 (1998).

[52] M. Elwenspoek and H. V. Jansen, *Silicon micromachining* (Cambridge Univ Press, Cambridge, 1998).

[53] D. L. Flamm, "Introduction to plasma chemistry", in *Plasma etching*, edited by D. M. Manos and D. L. Flamm (Academic Press, San Diego, 1989).

[54] F. Laermer and A. Schilp, "Verfahren zum anisotropen Ätzen von Silicium", DE Patent 4241045 (1994).

[55] G. Siebke, P. Holik, S. Schmitz, H. Schmitz, M. Lacher, and S. Steltenkamp, "A model for μ-biomimetic thermal infrared sensors based on the infrared receptors of *Melanophila acuminata*", Bioinspir. Biomim. **9**, 036012 (2014).

[56] J. H. Spurk and N. Aksel, *Strömungslehre* (Springer, Heidelberg, 2010).

[57] O. Tabata, K. Kawahata, S. Sugiyama, and I. Igarashi, "Mechanical property measurements of thin films using load-deflection of composite rectangular membranes", Sens. Actuators. **20**, 135–141 (1989).

[58] J. F. Shackelford and W. Alexander, "Mechanical properties of materials", in *CRC materials science and engineering handbook*, 3rd ed. (CRC Press, 2000).

[59] K. Petersen, "Dynamic micromechanics on silicon: techniques and devices", IEEE Transactions on Electron Devices **25**, 1241–1250 (1978).

[60] *Sylgard® 184 silicone elastomer*, Dow Corning (Midland, Michigan, USA, 2014).

[61] G. Siebke, P. Holik, S. Schmitz, S. Tätzner, J. Thiesler, and S. Steltenkamp, "The development of a μ-biomimetic uncooled ir-sensor inspired by the infrared receptors of *Melanophila acuminata*", Bioinspir. Biomim. (in press).

[62] K. C. Tang, E. Liao, W. L. Ong, J. D. S. Wong, A. Agarwal, R. Nagarajan, and L. Yobas, "Evaluation of bonding between oxygen plasma treated polydimethyl siloxane and passivated silicon", Journal of Physics: Conference Series **34**, 155 (2006).

[63] M. Quaglio, G. Canavese, E. Giuri, S. L. Marasso, D. Perrone, M. Cocuzza, and C. F. Pirri, "Evaluation of different pdms interconnection solutions for silicon, Pyrex and COC microfluidic chips", J. Micromech. Microeng. **18**, 055012 (2008).

[64] Elliptec Resonant Actuator AG, *A10E* (2008).

[65] I. D. Johnston, D. K. McCluskey, C. K. L. Tan, and M. C. Tracey, "Mechanical characterization of bulk Sylgard 184 for microfluidics and microengineering", J. Micromech. Microeng. **24** (2014).

[66] D. Armani, C. Liu, and N. Aluru, "Re-configurable fluid circuits by PDMS elastomer micromachining", in Twelfth IEEE international conference on micro electro mechanical systems (1999), pp. 222–227.

[67] M. Liu, J. R. Sun, Y. Sun, C. Bock, and Q. F. Chen, "Thickness-dependent mechanical properties of polydimethylsiloxane membranes", J. Micromech. Microeng. **19**, 035028 (2009).

[68] B. Lorenz, I. Mey, S. Steltenkamp, T. Fine, C. Rommel, M. M. Müller, A. Maiwald, J. Wegener, C. Steinem, and A. Janshoff, "Elasticity mapping of pore-suspending native cell membranes", small **5**, 832–838 (2009).

[69] T. Shimozawa, J. Murakami, and T. Kumagai, "Cricket wind receptors: thermal noise for the highest sensitivity known", in *Sensors and sensing in biology and engineering*, edited by F. G. Barth, J. A. C. Humphrey, and T. W. Secomb (Springer, Wien, 2003).

[70] S. Steltenkamp, C. Rommel, J. Wegener, and A. Janshoff, "Membrane stiffness of animal cells challenged by osmotic stress", small **2**, 1016–1020 (2006).

[71] T. Kahl, H. Bousack, E. S. Schneider, and H. Schmitz, "Infrared receptors of pyrophilous jewel beetles as model for new infrared sensors", Sens. Rev. **34**, 123–134 (2014).

[72] U. Leute, *Physik und ihre Anwendungen in Technik und Umwelt*, 2nd ed. (Hanser, München, 2004).

[73] Wacker-Chemie GmbH, *Wacker Siliconöle AK* (2001).

[74] J. Thiesler, "μ-biomimetic infrared sensor – capacitive radiation sensing and bubble-free filling", BA thesis (Westfälische Hochschule Gelsenkirchen Bocholt Recklinghausen, 2014).

[75] M. Lacher, P. Holik, M. Koch, and S. Schmitz, "Verfahren zum blasenfreien Füllen einer Mikrokavität", DE Patent 102009052828 (2009).

[76] G. Kissinger and W. Kissinger, "Hydrophilicity of silicon wafers for direct bonding", physica status solidi (a) **123**, 185–192 (1991).

[77] Analog Devices, Inc., *24-Bit capacitance-to-digital converter with temperature sensor – AD7745/AD7746* (2005).

[78] L. I. Berger, "Dielectric strength of insulating materials", in *CRC materials science and engineering handbook*, 3rd ed. (CRC Press, 2000).

[79] Objective Development Software GmbH, *Virtual USB port for AVR microcontrollers*, `http://www.obdev.at/products/vusb` (visited on 12/10/2014).

[80] Atmel Corporation, *8-bit Atmel with 8KBytes in-system programmable flash – ATmega8, ATmega8L* (2013).

[81] Analog Devices, Inc., *Full/low speed 2.5 kV USB digital isolator – ADuM3160* (2010).

[82] OSRAM Opto Semiconductors GmbH, *OSLON black series (940 nm) – FH4725S* (2014).

[83] OSRAM Opto Semiconductors GmbH, *OSLON SSL 80 – LHCP7P* (2013).

[84] G. Siebke, K. Gerngroß, P. Holik, S. Schmitz, M. Rohloff, S. Tätzner, and S. Steltenkamp, “An uncooled capacitive sensor for IR detection”, in Infrared technology and applications XL 2014, Vol. 9070, edited by B. F. Andresen, G. F. Fulop, C. M. Hansona, and P. R. Norton, Proc. SPIE (2014).

[85] R. Muller, T. Kamins, and M. Chan, *Device electronics for integrated circuits* (John Wiley & Sons, 2003).

[86] H. O. Pierson, “The CVD of ceramic materials: nitrides”, in *Handbook of chemical vapor deposition (CVD)*, edited by H. O. Pierson, 2nd ed. (William Andrew Publishing, Norwich, NY, 1999) Chap. 10, pp. 265–294.

[87] S. Smith, *The scientist and engineer’s guide to digital signal processing* (California Technical Pub., San Diego, 1997).

Danksagung

An dieser Stelle möchte ich mich bei allen bedanken, die mich bei der Anfertigung dieser Dissertation unterstützt haben.

Ich danke Herrn Prof. Dr. Schmieden vom Physikalischen Institut der Universität Bonn für die Betreuung meiner Arbeit und die Unterstützung beim Verfassen der Dissertation. Herrn Prof. Dr. U. B. Kaupp vom Forschungszentrum caesar danke ich für Zweitbetreuung und die Möglichkeit, laufende Forschungsergebnisse im Rahmen eines Seminars zu präsentieren.

Besonderer Dank gebührt Herrn Dr. Steltenkamp, der mir während der gesamten Zeit am Forschungszentrum caesar mit Rat und Tat zur Seite stand sowie Herrn Lacher für die anregenden Diskussionen über technologische Fragestellungen.

Ich danke dem gesamten Team der Mikrosystemtechnologie vom Forschungszentrum caesar für die angenehme Arbeitsatmosphäre, die Diskussionen und die Unterstützung bei der Umsetzung meiner Ideen.

Weiterhin möchte ich Herrn Prof. Dr. Bleckmann und Herrn Prof. Dr. Wermes für die Bereitschaft danken, Teil der Promotionskommission zu sein.

Außerdem möchte ich mich bei Herrn Prof. Janshoff und Herrn Dr. Mey von der Universität Göttingen für die Möglichkeit, AFM Messungen an ihrem Institut durchzuführen, bedanken.

Schließlich möchte ich mich bei meinen Eltern und meiner Frau Gesine bedanken, ohne deren Rückhalt diese Arbeit nie zustande gekommen wäre.